Improving fMRI Analysis and MR Reconstruction with the Incorporation of MR Relaxivities and Correlation Effect Examination

Meryem Muge Karaman
Marquette University

IMPROVING FMRI ANALYSIS AND MR RECONSTRUCTION WITH THE INCORPORATION OF MR RELAXIVITIES AND CORRELATION EFFECT EXAMINATION

by

M. Muge Karaman

A Dissertation submitted to the Faculty of the Graduate School,
Marquette University,
in Partial Fulfillment of the Requirements for
the Degree of Doctor of Philosophy

Milwaukee, Wisconsin

August 2014

ABSTRACT
IMPROVING FMRI ANALYSIS AND MR RECONSTRUCTION WITH THE
INCORPORATION OF MR RELAXIVITIES AND
CORRELATION EFFECT EXAMINATION

M. Muge Karaman

Marquette University

Functional magnetic resonance imaging (fMRI) and functional connectivity MRI (fcMRI) use the physical principles of nuclear MR to provide high resolution representations of brain activity and connectivity. As the fMRI and fcMRI signals are detected from the excited hydrogen atoms in a magnetic field, the acquired data is determined by the underlying physical processes, such as the MR relaxivities. In fMRI and fcMRI, the Fourier encoded frequency space measurements are reconstructed into brain images, then spatiotemporal processing operations are applied before computing the brain activation and connectivity statistics. This dissertation seeks to utilize the magnetic resonance (MR) relaxivities at different stages of the fMRI pipeline, and aims to observe the statistical implications of the spatiotemporal processing operators on the fMRI and fcMRI data. We first develop a new statistical complex-valued nonlinear fMRI activation model that incorporates the MR relaxivities of gray matter into the brain activation statistics by utilizing the physical MR magnetization equation and the first scans of the fMRI data. We provide both theoretical and experimental comparison between the proposed model with the conventional linear magnitude-only and complex-valued fMRI activation models. Our statistical analysis results show that the new model provides better accuracy in computing brain activation statistics while theoretically eliminating false positives in non-gray matter areas. We then develop a linear Fourier reconstruction operator that incorporates the MR relaxivities into the image reconstruction process to account for their effects. The utilization of a linear system makes it achievable to theoretically compute the statistical implications of the use of the proposed operator. By focusing on longitudinal relaxation time, T_1, to include into the image reconstruction, we show that the application of the proposed Fourier reconstruction operator provides better image contrast in the reconstructed images by recovering the information of the tissue characteristics that exist prior to T_1 equilibrium. We finally examine the effects of time series preprocessing on computed functional correlations through the use of linear operators and provide ways of accounting for such effects in computing functional activity and connectivity statistics. Using both theoretical and experimentally acquired functional connectivity data, we examine the correlations induced by commonly used spatial and temporal processing operations. Furthermore, we provide the expansion of the statistical fcMRI and fMRI models to incorporate the quantified processing induced correlations in computing brain activity and connectivity statistics.

ACKNOWLEDGEMENTS

M. Muge Karaman

TABLE OF CONTENTS

LIST OF TABLES

LIST OF FIGURES

Chapter 1:   Introduction

1.1   Motivation

Over the past two decades, functional magnetic resonance imaging (fMRI) and functional connectivity magnetic resonance imaging (fcMRI) have become two of the most dominant noninvasive means for neuroscientists and biomedical engineers to study brain activity and connectivity. Both fMRI and fcMRI use the blood's magnetic properties to identify the regions of the brain that are active in response to a specific task, and to determine the connectivity between brain regions that are linked across time. FMRI and fcMRI has been used to assess brain damage from head injury or degenerative disorders, identify and monitor neurological disorders; therefore provide important clinical information for treatment of such diseases and neurosurgical planning.

The scope of fMRI and fcMRI research covers data acquisition, image reconstruction, data processing, and data analysis. MRI data is acquired in the spatial frequency domain (k-space) and reconstructed into brain images using image reconstruction techniques. The measured magnetic resonance (MR) signal is affected by noise from various sources, such as physiological, thermal, system noise, and noise from random neuronal activity during the task performance. Therefore, it has been a common practice to use spatial and temporal data processing operations to attenuate noise in reconstructed images. After processing, statistical models are used for the fMRI and fcMRI data to determine cognitive brain activity and functional connectivity statistics. Despite promising research efforts, there is still a big gap between the real dynamics of the brain, and what the current analysis methods can provide from the images. An effort

to develop unified models that link the different stages of the fMRI and fcMRI pipeline, starting from the frequency space with the acquisition of the data and ending at the image space with the final activity and connectivity analyses, can lead to efficient and effective solutions to the significant questions in basic and clinical neuroscience. Additionally, an exact quantification of the statistical impact of data processing through a theoretical approach can effectively prevent possible incorrect conclusions drawn from the fMRI and fcMRI data. Development of quantitative models from these perspectives can have significant impact on investigating intractable and inexplicable problems in neuroimaging. Therefore, the overall goal of this research is directed towards developing statistical models to improve the accuracy of MR reconstruction and cognitive brain activation through the utilization of the fundamental physics of the nuclear MR signal, and improve the accuracy of the fMRI and fcMRI analyses by quantifying and accounting for the implications of spatiotemporal data processing.

This dissertation is organized in six chapters. This opening chapter provides a description of the theory and the background on which this dissertation is based. Chapter 2 develops a new statistical fMRI activation model that incorporates gray matter relaxation parameters into brain activation statistics by modeling the fMRI data from the correct MR magnetization, and utilizing the first scans for estimation of the MR relaxivities. The third chapter provides a mathematical model to incorporate the MR relaxivities into the image reconstruction process in a single step with an effort to improve the reconstructed images that are used as inputs in the fMRI and fcMRI models. In Chapter 4, this model is extended to a linear framework that precisely quantifies the statistical effects of spatiotemporal processing operations applied to the fMRI and fcMRI

data in such a way that the true statistical properties of the processed data can be utilized in the final brain activation and connectivity analysis. Chapter 5 provides future application methods to account for the quantified exact noise properties of the fMRI and fcMRI data in computing functional activity and functional connectivity statistics. Finally, Chapter 6 summarizes the contributions of the work presented in this dissertation and gives ideas for areas of future work.

1.2   Functional MRI and Functional Connectivity MRI

Functional MRI and fcMRI are specialized magnetic resonance imaging (MRI) procedures that measure activity and connectivity in the human brain. Blood oxygen level-dependent (BOLD) contrast-based fMRI/fcMRI visualizes brain functions by measuring the changes in the inhomogeneity of the magnetic field that results from changes in blood oxygenation (Ogawa et al., 1993, Biswal et al., 1995). While there are other methods to observe the changes in the metabolic activity that follow mental work, such as arterial spin labeling, BOLD contrast has become the most widely used image contrast in fMRI and fcMRI. The field inhomogeneities that are induced by blood vessels containing deoxyhemoglobin provides the main source of BOLD contrast. When there is neural activity in nerve cells, a steady supply of oxygen is required to metabolize glucose that is provided from the hemoglobin component of the blood cells that are bound to oxygen. Therefore, the neural activity results in an increased flow of oxygenated blood with a relative decrease in deoxyhemoglobin and an increase in oxyhemoglobin. The magnetic field inhomogeneities that are caused by the paramagnetic deoxygenated hemoglobin and the diamagnetic oxygenated hemoglobin during neural activity can be detected by an MRI scanner (Huettel and Song, 2008). The positive peak in the BOLD

signal reflects a regional decrease in the concentration of deoxyhemoglobin, and thereby an indicator of an increase in neural activity. By using the BOLD contrast mechanism, fMRI and fcMRI have become highly useful techniques that provide remarkable clinical advantages that further our understanding of brain function in health and disease without the need for surgery.

In fMRI experiments, the subject generally alternates between performing a task and resting while a time series of brain images are rapidly acquired. The increase in MR signal reflects the positive BOLD effect and is directly related to the underlying neural activity. When the stimulus is maintained for a sufficient time, the signal reaches a plateau (Buxton et al., 2004), eventually returns to the baseline after the stimulus is removed. The basic concept of fMRI is that the BOLD time series images can be used to indirectly detect a change in the neural activity associated with a subject performing a task. By using statistical models, the MR signal time course of each voxel in an image is compared to the task paradigm, and statistically tested for significance. The cortical and sub-cortical regions that have a signal correlated with the task are then identified and considered as functionally activated.

Functional connectivity MRI provides a means of noninvasively measuring the interdependency of brain regions with the use of cross correlation methodology even when there is no task, referred to as the resting state condition. In fcMRI, the correlations in the spontaneous fluctuations in the voxels' BOLD time courses are examined. The synchronized low-frequency blood flow fluctuations in distinct brain regions are detected and the regions that show statistically significant correlation are identified as functionally connected.

1.3 MR Physics and Modeling fMRI Data

The MR machine creates a strong magnetic field around the body parts to be scanned, and this magnetic field aligns most of the hydrogen protons in molecules along the axis of the MR scanner. When additional energy, a brief radio frequency (RF) wave, is applied into the magnetic field, the hydrogen atoms absorb energy (excitation), and their equilibrium state is perturbed. These hydrogen atoms emit energy which is called the relaxation process, and then they return from the tipped state to their original lower energy state of being aligned in the direction of the magnetic field. The characteristic times involved in the relaxation of the nuclear spin magnetization vector, M, are known as relaxation times. Longitudinal, or spin-lattice, relaxation time, T_1, is the decay constant for the recovery of the z component of the magnetization, M_z, towards its thermal equilibrium value, $M_{z,eq}$. The transverse, or spin-spin, relaxation time, T_2, is the decay constant for the component of M perpendicular to external magnetic field, B_0, designated M_{xy}. While all hydrogen nuclei in a magnetic field precess with the same frequency in an ideal system, there is an additional dephasing of the magnetization introduced by external field inhomogeneities. This reduction in the initial value of M_{xy} can be characterized by a separate decay time, T_2^*, which is the decay parameter for the magnetization including both T_2 from completely random interaction between spins and magnetic field inhomogeneities (Haacke et al., 1999). The relationship between T_2 and T_2^* can be expressed by $1/T_2^* = 1/T_2 + 1/T_2'$, where $T_2' = \gamma \Delta B$, γ is the gyromagnetic ratio of the nuclei being imaged, and ΔB is the magnetic field inhomogeneity across a voxel. For fMRI and fcMRI protons (hydrogen nuclei) are imaged, therefore $\gamma = 42.576$ MHz/T. The changes in blood oxygenation cause changes in magnetic field inhomogeneity and

thus in decay parameter T_2^*, as the T_2^* signal is relatively sensitive to the inhomogeneities in the magnetic field. This leads to changes in image intensity in T_2^*-weighted images, which are thus used to study brain activity in brain functional imaging studies (Ogawa et al., 1992).

The measured signal intensity in an MR image is the combination of the principal relaxation processes, T_1 and T_2^*, along with the proton spin density, M_0, and blood flow. Proton spin density is the concentration of the protons in water and other macromolecules in tissues. As the MR relaxation times, T_1 and T_2^*, define the rate that the protons in molecules relapse back to their equilibrium state after the first RF pulse, nuclear spin magnetization in fMRI follows an exponential decay. This physical mechanism in MRI leads to tissue-dependent signal intensity as the contrast of different tissues is determined by tissue-specific relaxation times.

One of the main challenges in detecting brain activation, as in many other fields in which the main aim is to draw medical conclusions from the data, is correctly and realistically modeling the acquired data. The process of fMRI data modeling can be considered to consist of two main components: realistically modeling MR magnetization, which is the main source of the acquired measurements, and effectively representing the activation information in the models that are used for fMRI activation analysis. Despite the known physical mechanisms behind MRI, and biological knowledge about brain functionality, a linear model has been used to describe fMRI data and the differential signal change resulting from activation (Bandettini et al., 1993; Rowe and Logan, 2004; Rowe and Logan 2005a,b). While such models have provided powerful tools for cognitive neuroscience researchers for years, a better representation of the acquired signal

that utilizes both physical and biological information can provide additional measurable benefits. The practical use of such models in the final analysis may ultimately contribute to advancing the clinical application of fMRI. As such, there is an apparent need for more physically and biologically driven models for fMRI analysis that aim to further improve the current models with the incorporation of physics that generates data.

1.4   Reconstructing MRI Data

In MRI, the spatial information of the real-valued object is Fourier encoded by magnetic field gradients and represented as complex-valued spatial frequencies. Therefore, the acquired complex-valued k-space measurements are generally expected to be the Fourier transformation of the physical image. These measurements are then transformed into the image measurements by performing image reconstruction via inverse Fourier transformation. Using (k_x, k_y) and (x, y) as the two dimensional k-space and image space variables respectively, the frequency space signal, $s(k_x, k_y)$, is given by

$$s(k_x, k_y) = \int_{-\infty}^{\infty} \int_{-\infty}^{\infty} M_0(x, y) e^{-i2\pi(k_x x + k_y y)} dx dy, \qquad [1.1]$$

which represents the Fourier image encoding process. In the above equation, $M_0(x, y)$ represents the proton (spin) density. The Fourier transform relationship in Eq. [1.1] can be inverted in order to obtain the Fourier image reconstruction process as

$$\hat{M}_0(x, y) = \int_{-\infty}^{\infty} \int_{-\infty}^{\infty} s(k_x, k_y) e^{i2\pi(k_x x + k_y y)} dk_x dk_y, \qquad [1.2]$$

where $\hat{M}_0(x, y)$ is the estimate of the proton spin density.

Although the original object's, proton spin density, M_0, is real-valued, a complex-valued image, $\hat{M}_0$, is obtained by Fourier reconstruction due to the magnetic field inhomogeneities resulting from motion and respiratory effects, and chemical shifts (Hahn et al., 2009; Hahn and Rowe, 2012; Hahn et al., 2012; Jezzard and Balaban, 1995). Furthermore, the physical mechanisms presented in section 1.3, specifically the MR relaxivities, along with the phenomena of non-instantaneous sampling of k-space lines alter the expected Hermitian symmetry and the signal strength of the frequency observations during Fourier encoding process. Such alteration results in image artifacts such as image warping, image blurring, and loss in image intensity in the reconstructed images.

Despite the known mechanisms that affect the measured MR signal during the Fourier encoding process, the commonly used Fourier reconstruction algorithms generally do not directly account for their effects when obtaining images from k-space measurements. While there has been a field of study to investigate and remove the effects of T_2^* and ΔB, these methods have been developed as a correction step rather than being incorporated into the Fourier image reconstruction process. Although the longitudinal relaxation time, T_1, provides a quantitative parameter to identify tissue characteristics, no effort has been made to maintain the contrast information that it offers in the reconstructed images. In fMRI and fcMRI models, the time series of the reconstructed images are used as inputs, and therefore the reliability of the final analyses significantly depends on the correctness of the reconstructed image measurements. Moreover, the accuracy of the fMRI and fcMRI models directly affects the precision of the corrections performed after image reconstruction such as motion correction and image registration.

As such, utilizing direct methods that account for the effects of the MR relaxivities that the fMRI signal is subject to could provide better accuracy in the further analysis of the data in a more efficient way.

1.5   Processing of fMRI and fcMRI Data

In fMRI and fcMRI, time series data can be considered as a combination of signal and "noise." Signal corresponds to hemodynamic changes that can be modeled as the convolution of the underlying neuronal process responding to experimental changes. Noise in fMRI and fcMRI has many components that give rise to the data having a complicated spatiotemporal correlation structure. Noise in the data consists of neuronal sources such as unmodeled neuronal effects in the frequency spectrum of hemodynamic signal, and non-neuronal sources that have physiological or non-physiological origin such as subject movement, respiration, cardiac, scanner artifacts, and uncontrollable system effects. Such noise corrupts the measured BOLD signal, decreases the signal-to-noise ratio (SNR), and reduces the accuracy of the experimental design and analysis. As such, it has been a common practice in fMRI and fcMRI studies to perform spatial and temporal processing operations, such as slice timing correction, motion correction, registration, normalization, spatial smoothing, global signal regression, and temporal filtering, before statistically analyzing the data. The processing of the data increases the ratio of BOLD contrast and noise, helps to meet the assumptions that are made in the given statistical models, and therefore plays a vital role in obtaining relevant results that can be interpreted by neuroscientists.

The statistical models that are used to analyze the fMRI and fcMRI data require numerous steps starting with raw data and ending with an activation image of statistics

values for evaluating hypotheses. Due to the complexity of this pipeline, the analysis of the fMRI and fcMRI data has commonly been performed through the use of various software packages, such as SPM, AFNI, FSL, FreeSurfer, and BrainVoyager, which are available to neuroscientists and biomedical engineers. While these sources allow users to input their data, apply numerous pre- and post-processing operations, and choose certain modeling options to conduct data analyses, the pitfall of such analysis is a "black box" that users are often not aware the reason and consequences of the use of certain processing and modeling options. One of the obstacles of using a black box system of this kind is the alteration of the signal and noise properties of the acquired data, specifically inducing correlations of no biological origin, which could be misinterpreted in the final connectivity and activity analyses. The considerations that need to be taken into account are to quantify the statistical implications of such processing of the time series, and accounting for the possible effects in the final analyses of the data.

Despite current efforts for investigating effects of the processing operations, such as temporal smoothing (Friston et al., 1999) and global signal regression (Chai et al., 2012; Saad et al., 2012; Murphy et al., 2009), on the analysis of fMRI and resting state fMRI data, the methodologies to account for such effects have not been well-integrated into the statistical models that produce the final results. Moreover, the traditional fMRI and fcMRI models generally assume independence between voxels and therefore do not account for the spatial correlation between voxels or temporal correlation within each voxel's time series. As such, a means by which the statistical implications of processing can be quantified and accounted for is necessary for neuroscientists to reap the benefits of processing operations without suffering from the statistical implications that they incur.

Chapter 2:   Incorporating MR Relaxivities for More Accurate fMRI Activation

In MRI and fMRI, two of the main areas of study are the estimation of the relaxation parameters and the detection of brain activations through changes in blood oxygenation. The quantification of the longitudinal and transverse relaxation times has become a common means of characterizing the tissue properties. In brain activation detection studies, the aim is to determine voxels in which there is a signal increase associated with specific neural activity when the subject performs a task. Traditionally, relaxation parameter estimation and brain activation detection are performed as separate studies, the results of which are not generally used together. It is the incentive of this chapter to introduce a new statistical fMRI model that can both estimate the relaxation parameters and determine brain activation by incorporating the simultaneously estimated MR relaxivities of gray matter, and modeling fMRI data from the correct MR magnetization equation rather than using a conventionally used linear model. The developed model serves to quantify the activation statistics in a more accurate and informed way while estimating the relaxation parameters at the same time.

2.1   Introduction

The spin density, M_0, longitudinal relaxation time, T_1, and transverse relaxation time, T_2^*, provide the three most intrinsic and basic contrast mechanisms in MRI/fMRI. It is thus of interest to measure and exploit differences in these parameters in order to develop image contrast between different brain tissue since the resulting measured values could be used for tissue characterization and provide useful information on local

environment interaction. The quantization of the relaxation parameters makes it possible to better understand the contrast mechanism and the tissue characterization.

The Bloch equations describe the behavior of a magnetization vector in the presence of an externally applied magnetic field subject to the relaxation process (Haacke et al., 1999). According to the solution of the Bloch equations, magnetization can be characterized by the tissue parameters (T_1, T_2 or T_2^*, M_0) and imaging parameters (TR, TE, ϕ) where TR is the repetition time, TE is the echo time, and ϕ is the RF flip angle. Thus, the signal change can be induced by a change in spin density, T_1, and/or T_2^*. In a T_2^*-weighted gradient echo fMRI experiment, for a given voxel, the magnetization after the tth RF excitation, M_t, for a series of excitations is given by:

$$M_t = \left[M_{t-1} e^{-\frac{TR}{T_1}} \cos(\phi) + M_0 \left(1 - e^{-\frac{TR}{T_1}} \right) \right] \sin(\phi) e^{-\frac{TE_t}{T_2^*}}. \qquad [2.1]$$

Accurate relaxation parameter estimation is essential in quantitative MR applications as being a fundamental way of determining image segmentation and tissue characterization as well as quantifying absolute metabolites in nuclear MR spectroscopy. It has been found that a significant variation is observed in the relaxation time parameters with many pathologies, such as cancer (Roebuck et al., 2009; Mariappan et al., 1988;) Alzheimer's disease (Haley et al., 2004), and Parkinson's disease (Antonini et al., 1993).

In addition to serving as a useful tool for improving clinical diagnosis, tissue characterization may serve as a very important source of information in detecting brain activation since it is generally believed that gray matter tissue includes the neurons that are to be active during the performance of a task. Considering the fact that fMRI is based on the hemodynamic changes related to neuronal activity, and not neuronal electrical

activity itself, the accuracy of the brain activation statistics calculated from the considered statistical fMRI activation model plays a major role for the medical statements that could be drawn. The incorporation of the information of the tissue characteristics into the brain activation detection process can restrict the search volume for activation detection within the gray matter and thereby theoretically eliminate the false positives in non-gray matter areas. A model of this kind can provide more accurate activation statistics by decreasing the number of the voxels that are mistakenly detected as active.

In traditional fMRI studies, the first few scans are generally discarded from the data set before brain activation is computed in an effort to avoid the effects of magnetic saturation. These first images, however, obtain important information on the relaxation decay parameters for the type of tissue contained in each voxel, which can ultimately be utilized to estimate the MR relaxivities and therefore quantify contrast mechanisms.

The estimation of MR relaxivities has been an interest of study as it is widely known that the knowledge of relaxation times can provide important information on the tissues. Although voxel time courses in fMRI are complex-valued (Bonny et al., 1996; Haldar et al., 2007; Liu et al., 1998; Mazaheri et al., 2006; Sijbers et al., 1999), using only the magnitude of complex-valued magnetic resonance images has become the gold standard for the estimation of the relaxation parameters. However, Baselice et al. (2012) presented a statistical technique to estimate relaxation times exploiting complex-valued MR images. Wheaton et al. (2003) reconstructed $T_1\rho$ maps from partial k-space image data using linear regression, and error was measured in relation to $T_1\rho$ maps created from the full k-space images. Haldar et al. (2007) used the variable projection algorithm for maximum likelihood estimation of T_1 relaxation parameters by reducing the four-

dimensional minimization problem to a two dimensional maximization problem, rather than iteratively solving the four-parameter curve fitting problem.

In fMRI, voxel time courses are complex-valued after Fourier, or non-Fourier image reconstruction due to the phase imperfections as a result of magnetic field inhomogeneities. Although biological information regarding the brain vasculature can be extracted from the phase (Lai and Glover, 1997; Nan and Nowak, 1999; Reichenbach, 2012; Rowe and Logan, 2004; Rowe and Logan 2005a,b; Menon 2002; Nencka et al., 2007), it has been a common practice in fMRI to determine functional brain activation from the magnitude-only data model which discards the phase information (Bandettini et al., 1993; Cox et al., 1995). The phase portion of the complex-valued MR images provides information about the magnetic field changes, which may be caused by tumor, velocity of blood flow in MR angiography, or the motion of cerebrospinal fluid through the central nervous system (Poncelet et al., 1992). Another application area of phase in MRI is BOLD MR venography, which uses phase images to achieve the optimal contrast between the veins and the surrounding tissue, and offers valuable knowledge about the hemodynamic processes involved in BOLD fMRI (Rauscher et al., 2003; Hall et al., 2002). A complex-valued fMRI activation model was presented by Rowe and Logan (2004) to determine functional brain activation and it was shown that the use of complex-valued data provides an improved power of detection at low SNRs and low CNRs. The statistical fMRI model for detecting activation introduced in this chapter is based upon the complex-valued activation model of Rowe and Logan.

In this chapter, we develop a statistical fMRI model for Differential T_2^* ConTrast Incorporating T_1 and T_2^* of Gray Matter (GM), so-called DeTeCT-ING Model, to

determine brain activation by incorporating T_1 and T_2^* of GM (Karaman et al., 2013a; Karaman et al., 2014a). The model considers the physical nonlinear signal equation to model the MR magnetization rather than using a linear model; utilizes the first scans of the complex-valued fMRI data to estimate each voxel's T_1 and T_2^*; and incorporates GM T_1 and T_2^* values into the activation statistics. A single pulse sequence is used with three parts, where in the first two parts the subject does not perform the task while in the third part the subject performs the task as in a standard fMRI experiment. In the first part, several images are acquired at a constant TE; in the second part, TE is varied; and in the third part TE is constant. This pulse sequence allows one to have the three parts for: a) T_1 estimation, b) T_2^* estimation and c) detecting activation, while all of the model parameters are estimated simultaneously using data from the entire scan. The parameter setting in the first part allows the utilization of signal change between data acquired during the transient state prior to T_1 equilibrium and the steady state images since the volumes at the beginning of fMRI block contains a transition signal and the signal of the first volume is $M_1 = M_0 e^{-TE_t/T_2^*}$. The second and third parts of the pulse sequence differentiates the signal with TE and differential task changes respectively since T_2^* is influenced by TE, and activation is modeled by differential signal change. Furthermore, a slightly modified version of the DeTeCT-ING Model, the DeTeCT Model, is developed by modeling the complex-valued observations according to the physical magnetization equation, utilizing the first scans to estimate the MR relaxivities, but not incorporating GM T_2^* and T_1 values into the activation statistics in order to observe the benefits of the GM MR relaxivities incorporation on the computed activation statistics. The Cramer-Rao Lower Bounds (CRLBs), which provide a lower bound for the variance of unbiased

parameter estimators, are also numerically calculated for the DeTeCT-ING and DeTeCT Models.

In order to observe the performance of the DeTeCT-ING model, theoretical illustrations are implemented on 96×96 phantom data through simulation, and the model is compared with the conventionally used magnitude-only (MO) and newer complex-valued (CV) fMRI activation models by comparing the means and variances of the model parameters and activation statistics with the true parameter values and CRLBs of the models. The DeTeCT-ING model is then evaluated by deploying all four models, DeTeCT-ING, DeTeCT, MO, and CV, in the acquired bilateral finger tapping fMRI data.

2.2 Theory

2.2.1 Complex-valued and Magnitude-only fMRI Activation Models

After the inverse Fourier transformation, images or voxel measurements are complex-valued and still corrupted by noise in both real and imaginary parts (Rowe and Logan, 2004). The complex-valued image measured over time in a given voxel is described as:

$$y_{CV_t} = \left(M_{CV_t} \cos\theta + \eta_{R_t} \right) + i \left(M_{CV_t} \sin\theta + \eta_{I_t} \right), \qquad [2.2]$$

where $t = 1,\ldots,n$. The noise vector is generally assumed to be $\left(\eta_{R_t}, \eta_{I_t} \right)' \sim N\left(0, \sigma^2 I_2 \right)$.

The data gathered during the course of an fMRI experiment is comprised of a sequence of individual MR images that are acquired while the subject performs a set of tasks. Throughout the experiment, the subject generally alternates between performing no task and performing a task allowing the task-related activations to be detected by

qualifying the relative changes in the measured signal between individual images. Using periods of non-task scans is a common means of establishing a baseline on which the assumption is made that the brain activity scales in a linear fashion. The linear model that is generally used to describe the temporally varying magnitude, M_{CV_t}, is

$$M_{CV_t} = x_t'\beta = \beta_0 + \beta_1 x_{1_t} + \cdots + \beta_q x_{qt},$$ [2.3]

where q is the number of non-baseline regressors, x_t is the tth row of an $n\times(q+1)$ design matrix X, β is a $(q+1)\times1$ vector of magnitude regression coefficients, and the operator "$\prime$" denotes the transpose of a vector or matrix. Thus, the observed complex-valued data at time t can be represented by a 2×1 real-valued vector,

$$\begin{pmatrix} y_{R_t} \\ y_{I_t} \end{pmatrix} = \begin{pmatrix} x_t'\beta\cos\theta \\ x_t'\beta\sin\theta \end{pmatrix} + \begin{pmatrix} \eta_{R_t} \\ \eta_{I_t} \end{pmatrix},$$ [2.4]

where y_{Rt} is the real part, and y_{It} is the imaginary part of the observed image-space data at time point, t. This model can also be written more generally as

$$\begin{matrix} y_{CV} & = & \begin{pmatrix} X & 0 \\ 0 & X \end{pmatrix} & \begin{pmatrix} \beta\cos\theta \\ \beta\sin\theta \end{pmatrix} & + & \eta \\ 2n\times1 & & 2n\times2(q+1) & 2(q+1)\times1 & & 2n\times1 \end{matrix},$$ [2.5]

where the observed vector of data $y_{CV} = (y_R', y_I')'$ is the vector of n observed real values stacked on the observed n imaginary values, and the vector of errors $\eta = (\eta_R', \eta_I')'$ is represented with the same order. The noise vector is assumed to be $\eta \sim N(0, \Sigma_v)$ where the temporal covariance matrix of the considered voxel, Σ_v, is generally assumed to be

$$\Sigma_v = \sigma^2 I_2 \otimes I_n.$$

Functional brain activation is detected by testing the significance of the task-related parameters on a voxel by voxel basis. In order to determine whether a voxel is active or not, the null hypothesis, H_0:$C\beta$=0 (there is no activation), is tested against the alternative hypothesis, H_1:$C\beta{\neq}0$ (there is activation). In this hypothesis testing set up, the full row rank contrast matrix C is set to (0,0,1) in order to test whether coefficient for the reference function is 0.

Unrestricted maximum likelihood estimates (MLEs) of the parameters, phase, $\hat{\theta}$, regression coefficients, $\hat{\beta}$, and variance, $\hat{\sigma}^2$, under the alternative hypothesis, H_1:$C\beta{\neq}0$, can be derived by maximizing the logarithm of the likelihood function, and yields

$$\tan\left(2\hat{\theta}\right)=\left[\frac{2\hat{\beta}'_R\left(X'X\right)\hat{\beta}_I}{\hat{\beta}'_R\left(X'X\right)\hat{\beta}_R-\hat{\beta}'_I\left(X'X\right)\hat{\beta}_I}\right]$$

$$\hat{\beta}=\hat{\beta}_R\cos\hat{\theta}+\hat{\beta}_I\sin\hat{\theta} \qquad\qquad [2.6]$$

$$\hat{\sigma}^2=\frac{1}{2n}\left[\begin{pmatrix}y_R\\y_I\end{pmatrix}-\begin{pmatrix}X\hat{\beta}\cos\hat{\theta}\\X\hat{\beta}\sin\hat{\theta}\end{pmatrix}\right]'\left[\begin{pmatrix}y_R\\y_I\end{pmatrix}-\begin{pmatrix}X\hat{\beta}\cos\hat{\theta}\\X\hat{\beta}\sin\hat{\theta}\end{pmatrix}\right],$$

under the alternative hypothesis. The estimates of the regression coefficients are

$\hat{\beta}_R=\left(X'X\right)^{-1}X'y_R$ from the real part of the time series, and $\hat{\beta}_I=\left(X'X\right)^{-1}X'y_I$ from the imaginary part of the time series. (Rowe and Logan, 2004; Rowe and Logan, 2005a,b).

The MLEs of the parameters, phase, $\tilde{\theta}$, regression coefficients, $\tilde{\beta}$, and variance, $\tilde{\sigma}^2$, under the constrained null hypothesis, H_0:$C\beta$=0, can also be derived by maximizing the logarithm of the likelihood function with the Lagrange multiplier term $\Psi'(C\beta-0)$ and yields

$$\tan\left(2\tilde{\theta}\right) = \left[\frac{2\hat{\beta}_R'\Psi\left(X'X\right)\hat{\beta}_I}{\hat{\beta}_R'\Psi\left(X'X\right)\hat{\beta}_R - \hat{\beta}_I'\Psi\left(X'X\right)\hat{\beta}_I}\right]$$

$$\tilde{\beta} = \Psi\left[\hat{\beta}_R\cos\tilde{\theta} + \hat{\beta}_I\sin\tilde{\theta}\right] \qquad [2.7]$$

$$\tilde{\sigma}^2 = \frac{1}{2n}\left[\begin{pmatrix}y_R\\y_I\end{pmatrix} - \begin{pmatrix}X\tilde{\beta}\cos\tilde{\theta}\\X\tilde{\beta}\sin\tilde{\theta}\end{pmatrix}\right]'\left[\begin{pmatrix}y_R\\y_I\end{pmatrix} - \begin{pmatrix}X\tilde{\beta}\cos\tilde{\theta}\\X\tilde{\beta}\sin\tilde{\theta}\end{pmatrix}\right],$$

where Ψ is

$$\Psi = I_{q+1} - (X'X)^{-1}C'[C(X'X)^{-1}C']^{-1}C. \qquad [2.8]$$

Denoting the maximum likelihood estimators under the alternative hypothesis using hats, and those under the null hypothesis using tildes, the generalized likelihood ratio statistics for the CV Model, -2logλ_C, can be derived as,

$$-2\log\lambda_C = 2n\log\left(\frac{\tilde{\sigma}^2}{\hat{\sigma}^2}\right). \qquad [2.9]$$

This statistic has an asymptotic χ_r^2 distribution for large samples, where r is the difference in the number of constraints between the alternative and the null hypotheses or the full row rank of C. Note that, when $r = 1$, two-sided testing can be performed using the signed likelihood ratio test that is given by

$$Z_C = sign\left(C\hat{\beta}\right)\sqrt{-2\log\lambda_C}, \qquad [2.10]$$

which has an approximate standard normal distribution under the null hypothesis (Rowe and Logan, 2004; Severini, 2001). With the given distributional specifications, the

CRLBs of the CV Model can be computed from the likelihood of the complex-valued data (Rowe, 2005a).

In fMRI, complex-valued time courses are almost exclusively converted to magnitude and phase time courses, then the magnitude-only activation is determined while phase voxel time courses are discarded (Bandettini et al., 1993; Cox et al., 1995). This typical method to compute the activation using only the magnitude at time t is denoted by y_{MO_t}, and is written as

$$y_{MO_t} = \left[\left(M_{MO_t} \cos\theta + \eta_{R_t} \right)^2 + \left(M_{MO_t} \sin\theta + \eta_{I_t} \right)^2 \right]^{\frac{1}{2}},$$ [2.11]

where the population magnitude, M_{MO_t}, is the same as M_{CV_t}, that is given by Eq. [2.3]. The magnitude of a complex-valued observation at time t is not normally distributed but is Ricean distributed (Gudbjartsson and Patz, 2005; Rice, 1944; Rowe and Logan, 2004; Adrian et al., 2013). The Ricean distribution of the magnitude, y_{MO_t}, at time t becomes normal with mean a mean of $x_t'\beta$ and a variance of σ^2 at high SNRs. This model can also be written as

$$\begin{array}{ccccc} y_{MO} & = & X & \beta & + & \varepsilon \\ n\times 1 & & n\times(q+1) & (q+1)\times 1 & & n\times 1 \end{array}$$ [2.12]

where $\varepsilon \sim N\left(0, \sigma^2 I_n\right)$ after suitable preprocessing of the data.

Assuming a normal distribution for the errors in Eq. [2.12], the unconstrained maximum likelihood estimates of the parameters (β, σ^2) can be derived as

$$\hat{\beta} = \left(X'X \right)^{-1} X'y_{MO}$$

$$\hat{\sigma}^2 = \left(y_{MO} - X\beta\right)'\left(y_{MO} - X\beta\right)/n. \tag{2.13}$$

In order to construct a generalized likelihood ratio test of the hypothesis H_0:$C\beta$=0 versus H_1:$C\beta$≠0, where C is a full row rank matrix, the likelihood under the constrained hypothesis is maximized. The constrained MLEs can be derived as

$$\tilde{\beta} = \Psi\hat{\beta}$$

$$\tilde{\sigma}^2 = \left(y_{MO} - X\beta\right)'\left(y_{MO} - X\beta\right)/n, \tag{2.14}$$

where Ψ is defined as in Eq. [2.8]. Similarly with the CV Model, the likelihood ratio statistics for the MO Model is given by,

$$-2\log\lambda_M = n\log\left(\frac{\tilde{\sigma}^2}{\hat{\sigma}^2}\right). \tag{2.15}$$

The likelihood ratio test has an asymptotic χ_1^2 distribution and is asymptotically equivalent to the usual t tests for activation given by

$$t = \frac{\hat{\beta}_2}{SE\left(\hat{\beta}_2\right)}. \tag{2.16}$$

In the above equation, $SE(\hat{\beta}_2)$ denotes the standard error of $\hat{\beta}_2$, and it is computed by $SE(\hat{\beta}_2) = \hat{\sigma}^2 W_{22}$, where W_{22} is the $(2,2)^{\text{th}}$ element of $W = \left(X'X\right)^{-1}$. With the given distributional specifications, the CRLBs can also be computed from the likelihood of the MO data (Rowe, 2005a).

The constant-phase CV Model, given by Eqs. [2.4] or [2.5], can be extended into a more general model that considers temporally varying phase (Rowe, 2005b). It was

shown that (Rowe, 2004; Rowe, 2005a,b; Logan and Rowe, 2004) for a bilateral finger tapping fMRI experiment, the CV Model has a greater statistical power than the MO Model, as it can detect activations in voxels where changes in the BOLD signal are noted in the magnitude and/or phase.

It is of note here that the modeling of the magnetization of the fMRI data relies on the assumption of linearity in both CV and MO Models as defined in Eq. [2.3] although the MR magnetization follows an exponential decay depending on the MR relaxivities. Additionally, the hypothesis testing settings of both models do not include any tissue characteristics information to be used for decreasing the number of voxels that are not in GM, which can be mistakenly declared active. Furthermore, the first images which could provide important biological information regarding the tissue type of each voxel have been discarded in both CV and MO Models before computing activation statistics given by Eqs. [2.10] and [2.16]. The new fMRI activation model presented section 2.2.2 utilizes such information that has been neglected in conventional studies in an effort to produce more accurate fMRI activation statistics.

2.2.2   A New Statistical fMRI Model for Differential T_2^* Contrast Incorporating T_1 and T_2^* of Gray Matter

The temporally varying magnitude of the signal can be represented by incorporating the effect of the task execution to the magnetization. In the DeTeCT-ING and DeTeCT Models, the temporally varying magnitude, M_t, for an individual voxel, is defined as

$$M_t = \left[M_{t-1} e^{-\frac{TR}{T_1}} \cos(\phi) + M_0 \left(1 - e^{-\frac{TR}{T_1}} \right) \right] \sin(\phi) e^{-\frac{TE_t}{T_2^* + \delta z_t}} + x_t' \beta_1, \qquad [2.17]$$

where $x_t' \beta_1 = \beta_1 x_t$.

In this model, z_t is a column vector containing the reference function related a block experimental design, δ is a coefficient for a reference function, z_t, and represents the task related differential signal change. As noted before, brain activation causes changes in blood oxygenation leading to changes in decay parameter, T_2^*. Therefore, the parameter δz_t is included with T_2^* in the exponential function. The design matrix, X, consists of a single column of counting numbers representing the linear trend, and β_1 is the coefficient for a time trend t. The complex-valued observations at time t can then be described as

$$y_t = \qquad\qquad\qquad\qquad\qquad\qquad\qquad\qquad\qquad [2.18]$$
$$\left[\left(M_{t-1} e^{-TR/T_1} \cos(\phi) + M_0 \left(1 - e^{-TR/T_1} \right) \right) \sin(\phi) e^{-TE_t / (T_2^* + \delta z_t)} + x_t' \beta_1 \right] (\cos\theta + i\sin\theta)$$
$$+ (\eta_{R_t} + i\eta_{I_t}),$$

where $\left(\eta_{R_t}, \eta_{I_t} \right)' \sim N\left(0, \sigma^2 I_2 \right)$ as in Eq. [2.2].

Least squares estimation is a method of estimating parameters by minimizing the squared discrepancies on the observed data and their expected values. Working in the complex domain with the data having normally distributed noise and dealing with an over determined system allows for the use of a least squares estimator, which is a computationally convenient measure of fit. As the unknown parameters of this model, $\left(M_0, T_1, T_2^*, \delta, \beta_1, \theta \right)$ are nonlinear in the representation of the magnetization given by Eq.

[2.18], a nonlinear least squares estimation can be implemented. The nonlinear least

squares estimator, $\hat{\Theta}(M_0, T_1, T_2^*, \delta, \beta_1, \theta)$ can be obtained by minimizing the function,

$$
\sigma^2\left(M_0, T_1, T_2^*, \delta, \beta_1, \theta \middle| y_{R_t}, y_{I_t}, TR, \phi, TE_t, z_t\right) =
$$
$$
\frac{1}{2n}\sum_{t=1}^{n}\left[\left(y_{R_t} - M_t\cos\theta\right)^2 + \left(y_{I_t} - M_t\sin\theta\right)^2\right],
\qquad [2.19]
$$

with respect to the unknown parameters, $M_0, T_1, T_2^*, \delta, \beta_1, \theta$; where M_t is given by Eq.

[2.17]. In this objective function, y_{R_t} and y_{I_t} are the real and imaginary parts of the

observed signal, y_t, of an individual voxel at time t; and $M_t\cos\theta$ and $M_t\sin\theta$ are the

expected real and imaginary parts of the signal.

It is well known that the least squares procedure corresponds to the MLE when

appropriate probabilistic assumptions about underlying error distributions can be made,

as in the proposed model. Since the nonlinear least squares problem has no closed

solution and is usually solved by iterative refinement, the parameters of the model will be

determined numerically.

The main issue in fMRI is comparing images in a statistically meaningful way. In

the model presented in this chapter, the simple matter of detecting 'activation', the local

increase in the effect of the task, with most of the brain unaffected by the task, is the

primary focus of study. The model parameters are estimated under appropriately

constrained null and alternative hypotheses, after which activation is determined, which

is characterized by differential T_2^* contrast, δ, with a generalized likelihood ratio statistic.

According to the parameterization in the setting of the DeTeCT-ING Model,

"active" or "on" regions in the brain contain voxels with values $T_1 = T_{1_{GM}}$, $T_2^* = T_2^*{}_{GM}$,

and $\delta \neq 0$ while "inactive" or "off" regions contain voxels with $T_1 = T_{1_{GM}}$, $T_2^* = T_2^*{}_{GM}$,

and $\delta = 0$, where $T_{1_{GM}}$ and $T_2^*{}_{GM}$ are GM T_1 and T_2^* values. Maximum likelihood

estimates of the parameters, $\left(M_0, T_1, T_2^*, \delta, \beta_1, \theta \right)$, can therefore be determined for both

restricted alternative and null hypotheses. The hypotheses pair,

$$H_0 : T_1 = T_{1_{GM}}, T_2^* = T_2^*{}_{GM} \ , \ \delta = 0 \text{ vs.}$$

$$H_1 : T_1 = T_{1_{GM}}, T_2^* = T_2^*{}_{GM} \ , \ \delta \neq 0 \qquad\qquad [2.20]$$

detects task related voxel activation in GM.

According to the parameterization in the setting of the DeTeCT Model, in which

the GM relaxivities are not incorporated into activation statistics, "active" or "on" regions

in the brain contain voxels with values $\delta \neq 0$ while "inactive" or "off" regions contain

voxels with $\delta = 0$ as in the MO and CV Models. Maximum likelihood estimates of the

parameters $\left(M_0, T_1, T_2^*, \delta, \beta_1, \theta \right)$ can be determined for both alternative and null

hypotheses. The hypotheses pair,

$$H_0 : \delta = 0 \text{ vs.}$$

$$H_1 : \delta \neq 0 \qquad\qquad [2.21]$$

detects task related voxel activation without consideration of the tissue type.

Parameter estimates under the null hypothesis, $\left(\tilde{M}_0, \tilde{T}_1, \tilde{T}_2^*, \tilde{\delta}, \tilde{\beta}_1, \tilde{\theta} \right)$, and the

alternative hypothesis, $\left(\hat{M}_0, \hat{T}_1, \hat{T}_2^*, \hat{\delta}, \hat{\beta}_1, \hat{\theta} \right)$, for the DeTeCT and DeTeCT-ING Models

can be determined by numerical minimization of Eq. [2.19] with respect to the

parameters. The generalized likelihood ratio statistics, λ_C, the ratio of restricted null over alternative hypotheses leads to the large sample χ_1^2 distributed statistic, $-2\log\lambda_C$, that is given in Eq. [2.9]. Two-sided testing can then be performed using the signed likelihood ratio test given by Eq. [2.10].

2.3   Methods and Materials

2.3.1   Simulated Data

Part I: Simulated Phantom Data with the Fixed Parameter Setting

The first part of the simulation study theoretically illustrates the properties of the parameter estimates for the introduced models. For this part, a 96×96 slice of the human brain with two 7×7 region of interests (ROIs) was realistically simulated according to the Shepp-Logan phantom standards (Gach et al., 2008). Data for all models was generated to simulate voxel activation from a bilateral finger tapping fMRI block design experiment by using the magnitude of the magnetization, M_t, of the DeTeCT and DeTeCT-ING Models, given in Eq. [2.17]. The block design consisted of 20 s off followed by sixteen epochs of 15 s on and 15 s off with TR = 1 s. The simulation consisted of $n = 510$ time points where the true activation structure is known to be within ROIs so that the model can be evaluated. The considered ROIs that were designated to have activation are shown in Fig. 2.1. The presented results for this part of our simulation study were calculated over 500 simulations.
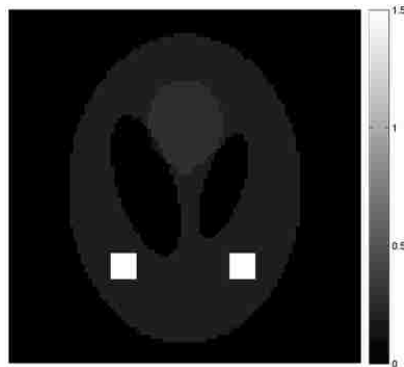
Figure 2.1: Anatomical mask with ROIs

The spin density and the relaxation parameter values of the simulated tissues measured at 3.0 Tesla (T) are given in Table 2.1 (Atlas, 2008). The parameter values of the voxels that consist of different kinds of tissue were obtained by averaging their values. For all voxels inside the phantom in this simulation, the phase angle, the linear trend coefficient, and the variance were generically selected to be $\theta = 45^\circ$, $\beta_1 = 0.01$, and $\sigma^2 = 0.0001$ which are values close to the those that are taken from a voxel in the activation region of a real data set. The differential T_2^* contrast, δ, was given a constant value of 1 for the voxels in ROIs while it was set to zero for the inactive regions. The value of δ was chosen based on the desired contrast-to-noise ratio (CNR = δ / σ) of 100. In generating the data, the RF flip angle is assumed to be $\phi = 90^\circ$ as it is commonly used in many MRI experiments. With this selection, the computational complexity of the numerical optimization problem is relatively reduced since the temporally varying magnitude of the magnetization, M_t, is simplified. The true maps of the spin density, M_0; longitudinal relaxation time, T_1; transverse relaxation time, T_2^*; differential T_2^* contrast, δ; linear trend, β_1, and phase angle, θ, are illustrated in Figs. 2.2a, 2.2b, 2.2c, 2.2d, 2.2e, and 2.2f, respectively.

Table 2.1: Spin density and the relaxation times for the Shepp-Logan Phantom.

Tissue	M_0	T_1 (in ms)	T_2^* (in ms)
Cerebrospinal Fluid (CSF)	1	4000	2200
Gray Matter (GM)	0.83	1331	42
White Matter (WM)	0.71	832	49
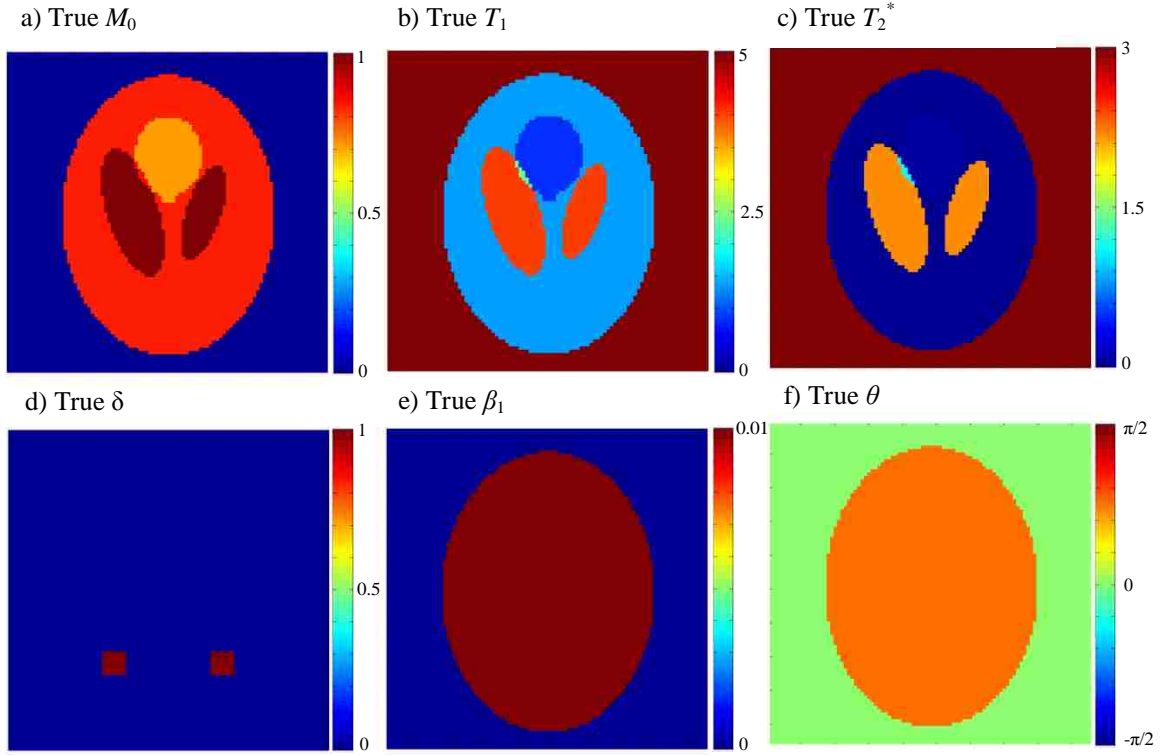
Figure 2.2: True parameter maps for the DeTeCT and DeTeCT-ING Models generated according to the Shepp-Logan phantom standards for a 96×96 slice. a) True M_0 map, b) true T_1 map (in s), c) true T_2^* map (in s), d) true δ map, e) true β_1 map, f) true θ map.

Simulated fMRI data was generated according to the proposed model given by Eqs. [2.17] and [2.18]. An fMRI block design experiment with an acquisition of 510 repetitions was used to estimate the model parameters. For each voxel, time depending echo time, TE_t, was assumed to consist of three parts. In the first part, it was fixed as having a value of 42.7 ms at the first 10 time points. In the second part, first 5 TE values were equispaced in the interval of [42.7 ms, 52.7 ms] that consists of the following TE

a) Echo time, TE$_t$ b) Reference function, z_t
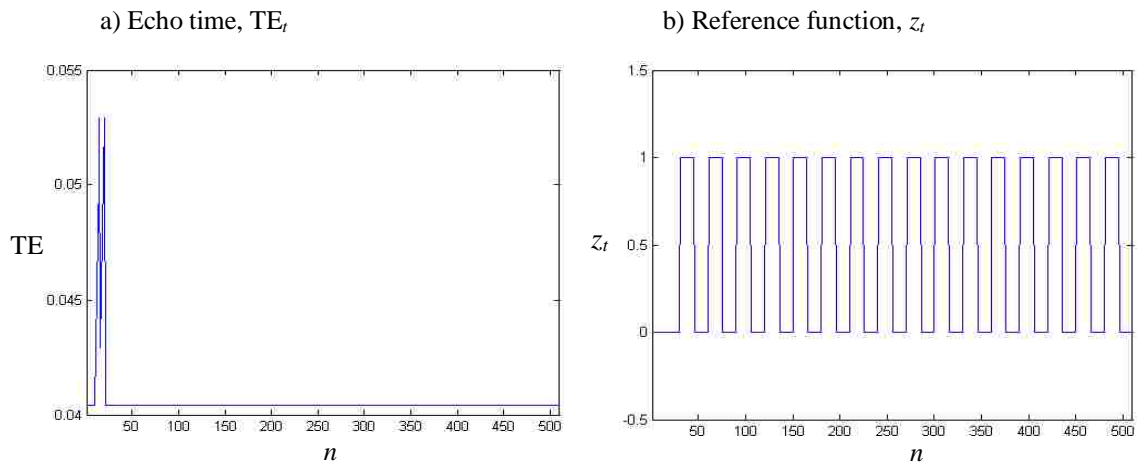
Figure 2.3: Imaging parameters. a) Echo time, TE$_t$; b) reference function, z_t.

values: 42.7, 45.2, 47.7, 50.2, 52.7; and this procedure was repeated again for the next 5

time points. Finally, the last 490 TE values were fixed as 42.7 ms as illustrated in Fig.

2.3a. The time trend X is a column of counting numbers, where the reference function, z_t,

which is illustrated in Fig. 2.3b, consists of blocks of 0's and 1's, as being related to the

block experimental design.

Part II: Simulated Data of Two Voxels with the Varying Parameter Setting

In this simulation study, we evaluate the performance of the considered models

for detecting activation with the use of the data generated from one active GM voxel in

an ROI area and one inactive GM voxel from outside of the ROIs at varying parameter

settings. For an effective evaluation of the models' performances, we created two sets of

scenarios that we vary a specific parameter, and analyze the models' detection

performance under these settings. These scenarios were created with the following

parameter settings: a) to analyze the models at different levels of the effect of the neural

activity in the signal: δ values of the active voxel varying from 0 to 1 with increments of

0.01, $\sigma^2 = 0.25$, and a commonly used threshold significance level, $\alpha = 0.05$; b) to

analyze the sensitivity of the models to the pre-specified threshold significance level, α,

level: α varying from 0.01 to 0.1 with steps of 0.0009, $\sigma^2 = 0.25$, and $\delta = 0.1$ for the

active voxel. The values of the fixed σ^2 and δ were selected as 0.25 and 0.1, respectively

to better observe the efficacy of the models in the presence of high standard deviation

noise level and low neural activity effect in the signal. All the other imaging parameters

were selected as the same as the ones in Part I. The number of simulations that were

performed for both voxels in each scenario was 1000. This simulation was used to

measure the accuracy of each model in recognizing the presence of the activation and

inactivation in order to compare the accuracy of the models' outcomes with the known

activation schemes.

Furthermore, in order to better analyze the overall performances of the models by

presenting the connection between the CRLBs and computed sample variances, we

created scenario "c" in which the data of the single active voxel was generated similarly

to scenario "a", with δ values varying from 0 to 1 with increments of 0.1, and threshold

significance level, $\alpha = 0.05$. For this scenario, we selected σ^2 to be 0.0001 in order to get

the same signal properties in our phantom simulation in Part I. The number of

simulations that were performed in scenario "c" was 1000.

2.3.2 Human Subject Data

To observe the performance of the proposed model in experimental data, an fMRI

experiment was performed on a single subject on a 3.0 T General Electric Signa LX

magnetic resonance imager. A bilateral finger-tapping task was performed with a visual

cue indicating whether to tap or rest. The paradigm followed a block design with an initial 20 s rest followed by 16 epochs of 15 s on and 15 s off. The data sets was composed of seven 2.5-mm-thick axial slices that are 96×96 in dimension for a 24-cm field of view (FOV), with the phase encoding direction oriented as posterior to anterior (bottom to top in images). A single slice was selected for the analysis. Acquired for a series of 510 TRs (repetitions), the data sets had a TR of 1 s, a flip angle of 90° and an acquisition bandwidth of 125 kHz. A time varying echo time, that is described in section 2.3.1 and presented in Fig. 2.3a, was used when acquiring the data.

As a common practice in fMRI studies, the first 3-5 observations are normally discarded and the reference function is usually chosen to be related to a block design consisting of epochs of on and offs starting at the 10th time point with a constant TE. As such, the signal that is acquired for the DeTeCT and DeTeCT-ING Models at the 11th – 20th time points is not acquired for the MO and CV Models. In order to imitate this common practice, the first 20 observations were excluded before applying the CV and MO Models to both simulated and acquired human brain data. Unlike traditional studies, these first observations were not discarded in the DeTeCT and DeTeCT-ING Models as they contain information on different tissue characterization. The "lsqnonlin" (least squares nonlinear solver) gradient based algorithm, available in the Matlab Optimization Toolbox (Matlab 2012) was used for the numerical minimization of Eq. [2.19] to estimate the parameters of the DeTeCT and DeTeCT-ING Models. The iterative Levenberg-Marquardt Method was chosen as the optimization method. The termination tolerances on the objective function and the parameter value were both set to 10^{-6}, while the maximum number of iterations allowed was 400 as the default values in Matlab's algorithm options.

The iteration process of Levenberg-Marquardt algorithm was terminated only when the convergence criterion, reaching the tolerance on either the objective function or the parameter value, was met. Activation from $-2\log\lambda$ likelihood ratio statistics which are given in Eq. [2.15] for the MO Model and Eq. [2.9] for the CV, DeTeCT and DeTeCT-ING Models, were thresholded at a 5% Bonferroni family-wise error rate (Logan and Rowe, 2004).

2.4   Results

2.4.1   Analysis

To observe the performance of the proposed models, the true parameter values and the theoretical minimum standard deviations are compared to the sample means and sample standard deviations of the model parameters computed from the simulation study presented in Part I of section 2.3.1.The parameter values that are assumed when generating the data for our simulation study are used as the true values of the parameters for the DeTeCT and DeTeCT-ING Models. For the parameters that only the CV and MO Models have, the analytically driven MLEs are used to compute true parameter values from the data with no added noise. Furthermore, the analytically driven CRLBs are used to calculate the theoretical minimum standard deviations for the CV and MO Models (Rowe, 2005a,b; Rowe, 2009) whereas the CRLBs of the DeTeCT and DeTeCT-ING Models are numerically calculated. The derivations of the analytical expressions for the partial derivatives of the likelihood function of the DeTeCT and DeTeCT-ING Models, which are used to numerically compute the CRLBs of the model parameters, are given in Appendix A. The CLRBs provide a quantitative measure of the attainable minimum

variance of the parameter estimates from a given set of observations. They give insight into the potential performance of the estimators, the performance of the implementation and the computation of the estimation models, and the efficiency of the estimators.

In order to better compare the estimated results and the theoretical values, first the sample mean and standard deviation of the parameter estimates under the alternative and null hypotheses for each model are computed. Then, the computed descriptive statistics are averaged across each tissue segment to obtain the "average voxel values" for each tissue type (GM: gray matter, WM: white matter, CSF: cerebrospinal fluid, Out: outside brain, and ROI). The computed average voxels values are presented in Tables 2.2-2.9. The first columns that correspond to each parameter represent the true value/theoretical minimum standard deviation values, the second and third columns represent the sample mean/standard deviation values computed from the null (Null) and the alternative (Alt) hypothesis, respectively. In the tables, the power of the estimation is given with a qualitative color code in which green represents a "good", orange represents a "fair", and red represents a "poor" estimate.

For the quantitative analysis of the activation detection performance of the models, the simulation results presented in Part II of section 2.3.1 were evaluated by utilizing three criteria. The first two are the true positive rate (TPR), proportion of the times that an active is correctly detected as active, and false positive rate (FPR), proportion of the times that an inactive voxel is incorrectly detected as active. The third criterion is the receiver operator characteristic (ROC), which is a qualitative plot of FPR (one minus the specificity) on the x-axis versus TPR (sensitivity) on the y-axis, that gives the tradeoff between the cost of failing to detect the activity against the cost of raising

false positives. First, we generate the TPR and FPR versus the parameters varied, δ and α, curves for scenarios "a" and "b", respectively, introduced in Part II of section 2.3.1. For the ROC curves, each varying parameter value (δ or α) determines a (x,y) point on the curve. To generate the ROC curves for scenarios "a" and "b", TPR and FPR for each δ or α value are computed from the data of the selected active and inactive voxels, respectively. The TPRs and FPRs are then averaged across 1000 simulated images to generate the (x,y) point. ROC curves range from (0,0) to (1,1), and a good model is expected to have a curve that is as close to the upper left quadrant (0,1) as possible.

The "efficiency" of a model's estimator can be considered as the closeness of the computed variance to the theoretical minimal variance of the estimator. In order to evaluate the efficiency of the models' estimators, the single voxel simulation that is performed under scenario "a" is used for the analysis of the properties of the parameter estimates. In the first part of this analysis, we compare the theoretical minimum standard deviations computed from CRLBs and the sample standard deviations of the parameters. Then, we perform a comparison between the mean squared errors (MSEs) of the estimators, which incorporate both the variance and the bias of the estimators.

All computations were performed on an HP Z600 with dual-quad core Xeon X5570 2.93 GHz processors, 24 GB of DDR3 RAM, 1 TB SATA-300 hard drive, 64 bit, Windows 7 in Matlab 2012. The computation times of the DeTeCT and DeTeCT-ING Models for the estimation of the model parameters and the activation statistics of a 96×96 human subject data that was acquired with the setting given in section 3.2 were found to be 77.36 minutes and 9.23 minutes, respectively. The reason of having higher

computation time for the DeTeCT Model can be explained by the computational

complexity of this model resulting from simultaneous estimation of seven parameters.

2.4.2 Simulated Data Results

Part I: Simulated Phantom Data with the Fixed Parameter Setting

The true value and the theoretical minimum standard deviation maps of the

parameters of the CV and MO Models were produced according to the MLEs and CLRBs

of the models by using the noiseless complex fMRI data (Rowe, 2005a,b). The average

voxel values of the true values as well as the calculated sample mean maps of the

estimated parameters under the null and alternative hypothesis for each tissue type are

given in Table 2.2 for the CV Model, and in Table 2.4 for the MO Model. Similar tables

for the theoretical minimum and computed sample standard deviation maps of the CV

and MO Models are also given in Table 2.3 and Table 2.5, respectively. It can be

observed that the CV and MO Models mostly yield "good" results. However, it should be

noted here that the results of these two models are compared with the true value and

theoretical minimum standard deviation maps calculated from the considered models

themselves. Furthermore, the CV and MO Models do not provide the proton spin density

and relaxation parameter estimates unlike the DeTeCT and DeTeCT-ING Models.

The true parameter maps of the DeTeCT and DeTeCT-ING Models were given in

Figs. 2.2a-2.2f. The calculated sample mean of the estimated parameters, M_0, T_1, T_2^*, δ,

β_1, θ, σ^2, from the DeTeCT Model are given in Figs. 2.4a-2.4g (left: alternative, right:

null hypothesis), respectively. It can be observed that the estimated parameters under the

alternative hypothesis appear to be similar to the true parameter values given in Fig. 2.1

Table 2.2: The average voxel values of the sample mean maps computed by using the CV Model from the data generated by the DeTeCT-ING Model. The results are presented for the true values (True), and the estimates under the alternative (Alt) and null (Null) hypothesis.

MEAN	β_0			β_1			β_2		
	β_0 True	β_0 Alt	β_0 Null	β_1 True	β_1 Alt	β_1 Null	β_2 True	β_2 Alt	β_2 Null
GM	2.7080	2.7080	2.7080	0.01	0.01	0.01	3.80E-16	-4.41E-08	0
WM	2.7580	2.7580	2.7580	0.01	0.01	0.01	1.64E-16	2.95E-07	0
CSF	2.7570	2.7570	2.7570	0.01	0.01	0.01	2.09E-16	-2.06E-06	0
Out	1.00E-14	-1.00E-06	-4.00E-07	1.00E-17	-2.00E-09	-2.00E-09	6.00E-31	1.00E-06	0
ROI	2.7076	2.7076	2.8322	0.01	0.01	0.01	0.2542	0.2542	0

MEAN	θ			σ^2		
	θ True	θ Alt	θ Null	σ^2 True	σ^2 Alt	σ^2 Null
GM	0.7854	0.7854	0.7854	0.0001	9.9E-05	0.0001
WM	0.7854	0.7854	0.7854	0.0001	9.9E-05	0.0001
CSF	0.7854	0.7854	0.7854	0.0001	9.9E-05	0.0001
Out	0	0.0002	-0.0005	0.0001	9.9E-05	0.0001
ROI	0.7854	0.7854	0.7854	0.0001	9.9E-05	0.0008

Table 2.3: The average voxel values of the sample standard deviation maps computed by using the CV Model from the data generated by the DeTeCT-ING Model. The results are presented for the minimum theoretical values (Min. Theo.), and the estimates under the alternative (Alt) and null (Null) hypothesis.

SD	β_0			β_1			β_2		
	β_0 Min. Theo.	β_0 Alt	β_0 Null	β_1 Min. Theo.	β_1 Alt	β_1 Null	β_2 Min. Theo.	β_2 Alt	β_2 Null
GM	0.0006	0.0006	0.0005	3.00E-06	3.20E-06	3.20E-06	0.0009	0.0009	0
WM	0.0006	0.0006	0.0005	3.00E-06	3.20E-06	3.20E-06	0.0009	0.0009	0
CSF	0.0006	0.0006	0.0005	3.00E-06	3.20E-06	3.20E-06	0.0009	0.0009	0
Out	0.0006	0.0008	0.0005	3.00E-06	4.10E-06	4.10E-06	0.0009	0.0002	0
ROI	0.0006	0.0006	0.0005	3.00E-06	3.20E-06	3.20E-06	0.0009	0.0009	0

SD	θ			σ^2		
	θ Min. Theo.	θ Alt	θ Null	σ^2 Min. Theo.	σ^2 Alt	σ^2 Null
GM	0.0001	0.0001	0.0002	5.00E-06	4.50E-06	4.50E-06
WM	0.0001	0.0001	0.0002	5.00E-06	4.50E-06	4.50E-06
CSF	0.0001	0.0001	0.0002	5.00E-06	4.50E-06	4.50E-06
Out	0.0001	0.9070	0.9015	5.00E-06	4.50E-06	4.50E-06
ROI	0.0001	0.0001	0.0002	5.00E-06	4.50E-06	5.70E-06

Table 2.4: The average voxel values of the sample mean maps computed by using the MO Model from the data generated by the DeTeCT-ING Model. The results are presented for the true values (True), and the estimates under the alternative (Alt) and null (Null) hypothesis.

MEAN	β_0			β_1			β_2		
	β_0 True	β_0 Alt	β_0 Null	β_1 True	β_1 Alt	β_1 Null	β_2 True	β_2 Alt	β_2 Null
GM	2.7080	2.7080	2.7080	0.01	0.01	0.01	2.00E-16	-1.60E-06	0
WM	2.7580	2.7580	2.7580	0.01	0.01	0.01	2.10E-16	-1.00E-06	0
CSF	2.7570	2.7570	2.7570	0.01	0.01	0.01	3.30E-16	-3.40E-06	0
Out	0	0.0130	0.0130	1.00E-17	0	0	6.10E-31	2.90E-07	0
ROI	2.7080	2.7080	2.8320	0.01	0.01	0.01	0.2542	0.2542	0

MEAN	σ^2		
	σ^2 True	σ^2 Alt	σ^2 Null
GM	0.0001	9.90E-05	9.90E-05
WM	0.0001	9.90E-05	9.90E-05
CSF	0.0001	9.90E-05	9.90E-05
Out	0.0001	4.20E-05	4.20E-05
ROI	0.0001	9.90E-05	0.0162

Table 2.5: The average voxel values of the sample standard deviation maps computed by using the MO Model from the data generated by the DeTeCT-ING Model. The results are presented for the minimum theoretical values (Min. Theo.), and the estimates under the alternative (Alt) and null (Null) hypothesis.

SD	β_0			β_1			β_2		
	β_0 Min. Theo.	β_0 Alt	β_0 Null	β_1 Min. Theo.	β_1 Alt	β_1 Null	β_2 Min. Theo.	β_2 Alt	β_2 Null
GM	0.0006	0.0006	0.0005	3.00E-06	3.00E-06	3.00E-06	0.0009	0.0009	0
WM	0.0006	0.0006	0.0005	3.00E-06	3.00E-06	3.00E-06	0.0009	0.0009	0
CSF	0.0006	0.0006	0.0005	3.00E-06	3.00E-06	3.00E-06	0.0009	0.0009	0
Out	0.0006	0.0004	0.0003	3.00E-06	2.00E-06	2.00E-06	0.0009	0.0006	0
ROI	0.0006	0.0006	0.0005	3.00E-06	3.00E-06	3.00E-06	0.0009	0.0009	0

SD	σ^2		
	σ^2 Min. Theo.	σ^2 Alt	σ^2 Null
GM	6.00E-06	6.30E-06	6.30E-06
WM	6.00E-06	6.30E-06	6.30E-06
CSF	6.00E-06	6.30E-06	6.30E-06
Out	6.00E-06	2.80E-06	2.90E-06
ROI	6.00E-06	6.30E-06	6.30E-06
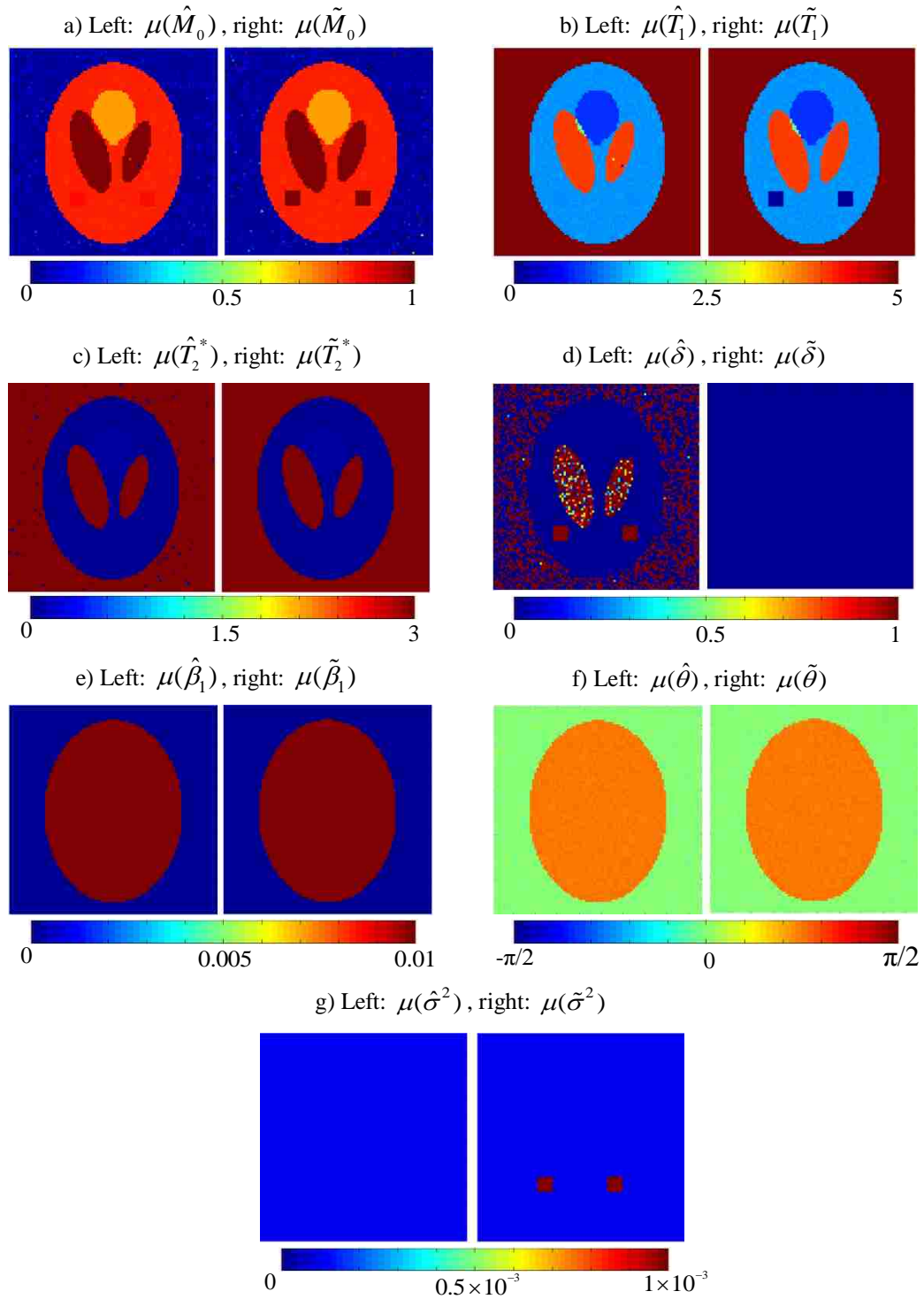
Figure 2.4: Calculated sample mean maps of the DeTeCT Model parameters. a) $\mu(\hat{M}_0)$ and $\mu(\tilde{M}_0)$, b) $\mu(\hat{T}_1)$ and $\mu(\tilde{T}_1)$ in s, c) $\mu(\hat{T}_2^*)$ and $\mu(\tilde{T}_2^*)$ in s, d) $\mu(\hat{\delta})$ and $\mu(\tilde{\delta})$, e) $\mu(\hat{\beta}_1)$ and $\mu(\tilde{\beta}_1)$, (f) $\mu(\hat{\theta})$ and $\mu(\tilde{\theta})$, g) $\mu(\hat{\sigma}^2)$ and $\mu(\tilde{\sigma}^2)$.

except the blurring that is the result of the noise in the signal as well as the systematic

error of the numerical optimization procedure. It can also be seen that the most apparent

difference between the null and alternative hypotheses estimation results occurs in ROIs

Table 2.6 provides a detailed comparison between the true value and the sample

mean estimated parameter values of the DeTeCT Model. One can observe that the

difference between the calculated sample means and the true values of T_2^* and δ is higher

in CSF, Out, and ROI areas compared to the difference for the other parameters in other

areas. The poor estimation that appears in such tissues could be considered as the result

of having a nonlinear objective function given in Eq. [2.19] and six different parameters

to be optimized in this system.

Table 2.7 illustrates a comparison between the theoretical minimum standard

deviations and the computed sample standard deviations of the estimated parameters of

the DeTeCT Model. Although the sample standard deviations of T_1, T_2^* and δ are higher

compared to the related CRLBs, mostly in CSF, Out, and ROI areas, the DeTeCT Model

mainly produces "good" results in terms of the variances of the estimated parameters.

The sample mean of the estimated parameters, M_0, δ, β_1, θ, and σ^2, of the

DeTeCT-ING Model under the null and alternative hypotheses are shown in Figs. 2.5a-

2.5e (left: alternative, right: null hypothesis), respectively. The average voxel values of

the true parameter values and the calculated sample mean maps are given in Table 2.8

whereas the CRLBs and the calculated sample standard deviations are shown in Table

2.9. Fig. 2.5 as well as Tables 2.8 and 2.9 show that the DeTeCT-ING Model has a high

statistical power in estimating the parameters. One can observe the only "fair" and "poor"

estimates appear to be in M_0 in WM and δ outside the phantom. However, better δ

estimates can be seen in Fig. 2.5b compared to Fig. 2.4d. It should be noted here that no signal areas, such as outside of the brain, have not been masked after estimation. It is thus expected that the parameters for the voxels outside the phantom may not have been estimated precisely as we expect.

Table 2.6: The average voxel values of the sample mean maps computed by using the DeTeCT Model from the data generated by the model itself. The results are presented for the true values (True), and the estimates under the alternative (Alt) and null (Null) hypothesis.

MEAN	M_0			T_1			T_2^*		
	M_0 True	M_0 Alt	M_0 Null	T_1 True	T_1 Alt	T_1 Null	T_2^* True	T_2^* Alt	T_2^* Null
GM	0.8300	0.8340	0.8330	1.3310	1.3270	1.3270	0.0420	0.0426	0.0425
WM	0.7100	0.7110	0.7110	0.8320	0.8300	0.8300	0.0490	0.0495	0.0495
CSF	1.0000	1.0300	1.0250	4.0000	4.0250	4.0210	2.2000	9.6711	14.0790
Out	0	0.0004	0.0006	1000.0	1001.7	1001.8	1000.0	773.3	921.5
ROI	0.8300	0.8563	9.4460	1.3310	1.3205	0.0783	0.0420	0.0407	0.0120

MEAN	δ			β_1		
	δ True	δ Alt	δ Null	β_1 True	β_1 Alt	β_1 Null
GM	0	7.30E-06	0	0.0100	0.0100	0.0100
WM	0	6.70E-06	0	0.0100	0.0099	0.0099
CSF	0	1.3170	0	0.0100	0.0099	0.0099
Out	1.00E-07	-57.1	0	1.00E-07	-3.00E-09	-3.00E-09
ROI	1	3.8050	0	0.0100	0.0099	0.0100

MEAN	θ			σ^2		
	θ True	θ Alt	θ Null	σ^2 True	σ^2 Alt	σ^2 Null
GM	0.7853	0.7853	0.7853	0.0001	9.90E-05	9.90E-05
WM	0.7853	0.7853	0.7853	0.0001	9.90E-05	9.90E-05
CSF	0.7853	0.7853	0.7853	0.0001	9.90E-05	9.90E-05
Out	0	0.0004	0.0004	0.0001	9.90E-05	9.90E-05
ROI	0.7853	0.7853	0.7853	0.0001	9.90E-05	0.0080

Table 2.7: The average voxel values of the sample standard deviation maps computed by using the DeTeCT Model from the data generated by the model itself. The results are presented for the minimum theoretical values (Min. Theo.), and the estimates under the alternative (Alt) and null (Null) hypothesis.

SD	M_0			T_1			$T_2{}^*$		
	M_0 Min. Theo.	M_0 Alt	M_0 Null	T_1 Min. Theo.	T_1 Alt	T_1 Null	$T_2{}^*$ Min. Theo.	$T_2{}^*$ Alt	$T_2{}^*$ Null
GM	0.0857	0.0856	0.0851	0.0358	0.0367	0.0365	0.0052	0.0055	0.0054
WM	0.0537	0.0537	0.0534	0.0237	0.0240	0.0238	0.0053	0.0055	0.0054
CSF	0.0718	0.8674	0.1191	0.0158	3.9971	0.5101	8.8591	20.285	25.833
Out	0.2807	1.1572	4.3318	3.14E-13	74.2	75.8	1.1E-19	7140.6	1203.4
ROI	0.0857	0.0586	3.0724	0.0358	0.0370	0.0271	0.0052	0.0029	0.0020

SD	δ			β_1		
	δ Min. Theo.	δ Alt	δ Null	β_1 Min. Theo.	β_1 Alt	β_1 Null
GM	0.0002	0.0002	0	3.00E-06	3.00E-06	3.00E-06
WM	0.0002	0.0002	0	3.00E-06	3.00E-06	3.00E-06
CSF	0.4659	24.7	0	3.00E-08	3.00E-08	3.00E-08
Out	5.00E-20	5053.6	0	9.00E-07	3.00E-08	3.00E-08
ROI	3.2462	6.8134	0	3.00E-06	3.00E-08	3.00E-08

| SD	θ			σ^2		
	θ Min. Theo.	θ Alt	θ Null	σ^2 Min. Theo.	σ^2 Alt	σ^2 Null
GM	0.0014	0.0014	0.0014	4.4E-06	4.4E-06	4.4E-06
WM	0.0014	0.0014	0.0014	4.4E-06	4.4E-06	4.4E-06
CSF	0.0014	0.0014	0.0014	4.4E-06	4.4E-06	4.4E-06
Out	6.70E-12	0.0830	0.0830	4.4E-06	4.4E-06	4.4E-06
ROI	0.0013	0.0013	0.0013	4.4E-06	4.4E-06	5.6E-06

Table 2.8: The average voxel values of the sample mean maps computed by using the DeTeCT-ING Model from the data generated by the model itself. The results are presented for the true values (True), and the estimates under the alternative (Alt) and null (Null) hypothesis.

MEAN	M_0			δ			β_1		
	M_0 True	M_0 Alt	M_0 Null	δ True	δ Alt	δ Null	β_1 True	β_1 Alt	β_1 Null
GM	0.8300	0.8299	0.8290	0	1.00E-06	0	0.0100	0.0100	0.0100
WM	0.7100	1.0801	1.0799	0	-2.00E-05	0	0.0100	0.0099	0.0099
CSF	1.0000	1.0881	1.0860	0	-2.00E-04	0	0.0100	0.0099	0.0099
Out	1.00E-11	1.9E-06	3.E-06	1E-17	45.1	0	1E-17	-2.80E-09	-3.20E-09
ROI	0.8300	0.8300	1.3820	1	1.0160	0	0.0100	0.0099	0.0100

MEAN	θ			σ^2		
	θ True	θ Alt	θ Null	σ^2 True	σ^2 Alt	σ^2 Null
GM	0.7853	0.7853	0.7853	0.0001	9.96E-05	9.97E-05
WM	0.7853	0.7853	0.7853	0.0001	9.98E-05	9.99E-05
CSF	0.7853	0.7853	0.7853	0.0001	0.0001	0.0001
Out	0	0.0001	0.0002	0.0001	9.95E-05	9.96E-05
ROI	0.7853	0.785	0.7853	0.0001	9.96E-05	0.0080

As previously noted, activations are calculated from the likelihood ratio statistics, $-2\log\lambda_M$, for the MO Model, and $-2\log\lambda_C$ for the CV, DeTeCT, and DeTeCT-ING Models given in Eqs. [2.9] and [2.15], respectively. The sample mean and the standard deviation of the activation statistics maps, Z-statistics for the CV, DeTeCT and DeTeCT-ING Models and t-statistics for the MO Model, that were thresholded at a 5% Bonferroni family-wise error rate are given in Figs. 2.6a-2.6d and Figs. 2.6e-2.6h, respectively. None of the models appears to produce false positives due to the low uncertainty in the simulated data. However, Figs. 2.6e-2.6h show that DeTeCT-ING Model produces lower variance in all tissue types in the phantom compared to the other models.

a) Left: $\mu(\hat{M}_0)$, right: $\mu(\tilde{M}_0)$

b) Left: $\mu(\hat{\delta})$, right: $\mu(\tilde{\delta})$

c) Left: $\mu(\hat{\beta}_1)$, right: $\mu(\tilde{\beta}_1)$

d) Left: $\mu(\hat{\theta})$, right: $\mu(\hat{\theta})$

e) Left: $\mu(\hat{\sigma}^2)$, right: $\mu(\tilde{\sigma}^2)$
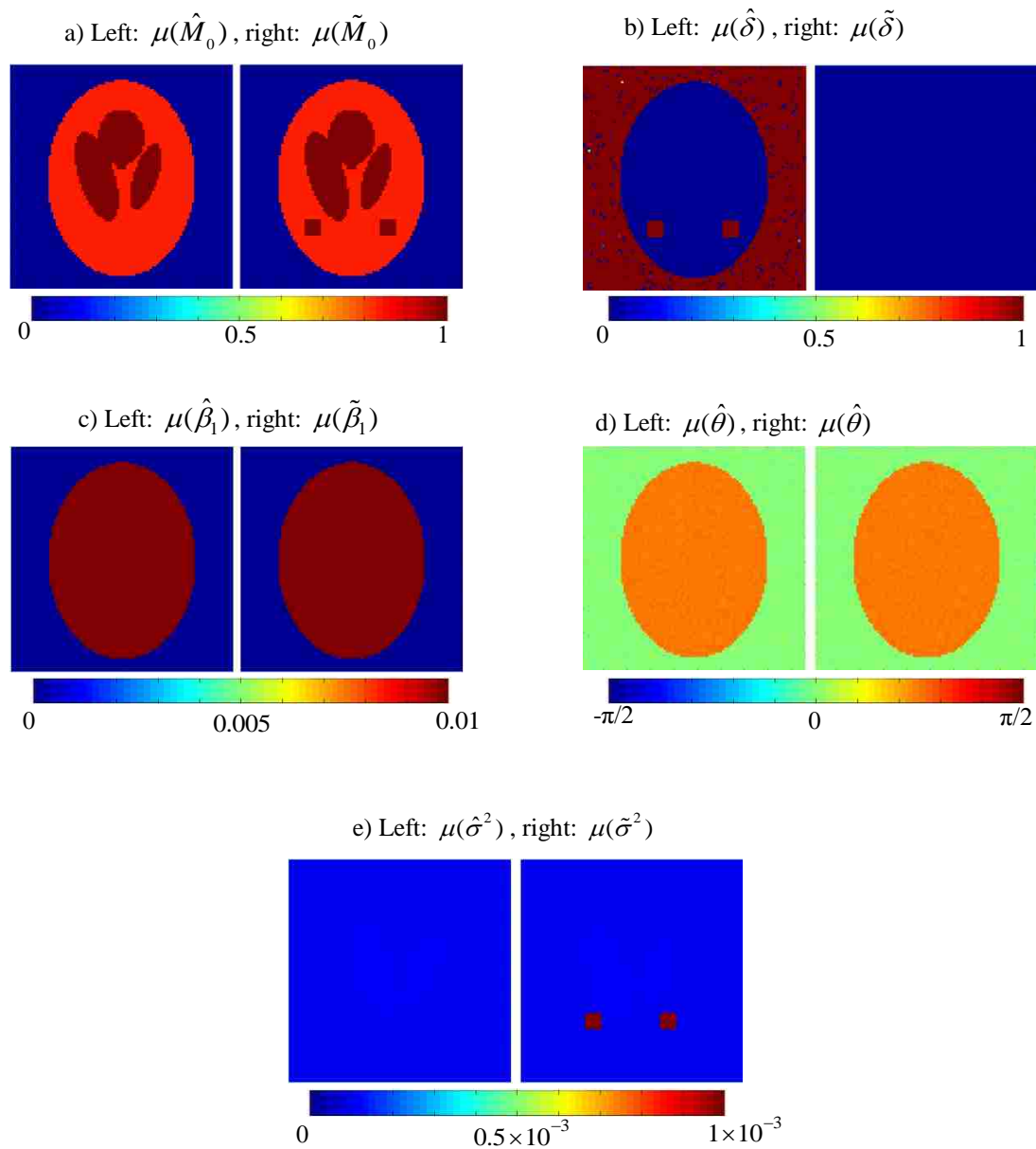
Figure 2.5: Calculated sample mean maps of the DeTeCT-ING Model parameters. a) $\mu(\hat{M}_0)$ and $\mu(\tilde{M}_0)$, b) $\mu(\hat{\delta})$ and $\mu(\tilde{\delta})$, c) $\mu(\hat{\beta}_1)$ and $\mu(\tilde{\beta}_1)$, (d) $\mu(\hat{\theta})$ and $\mu(\tilde{\theta})$, e) $\mu(\hat{\sigma}^2)$ and $\mu(\tilde{\sigma}^2)$.
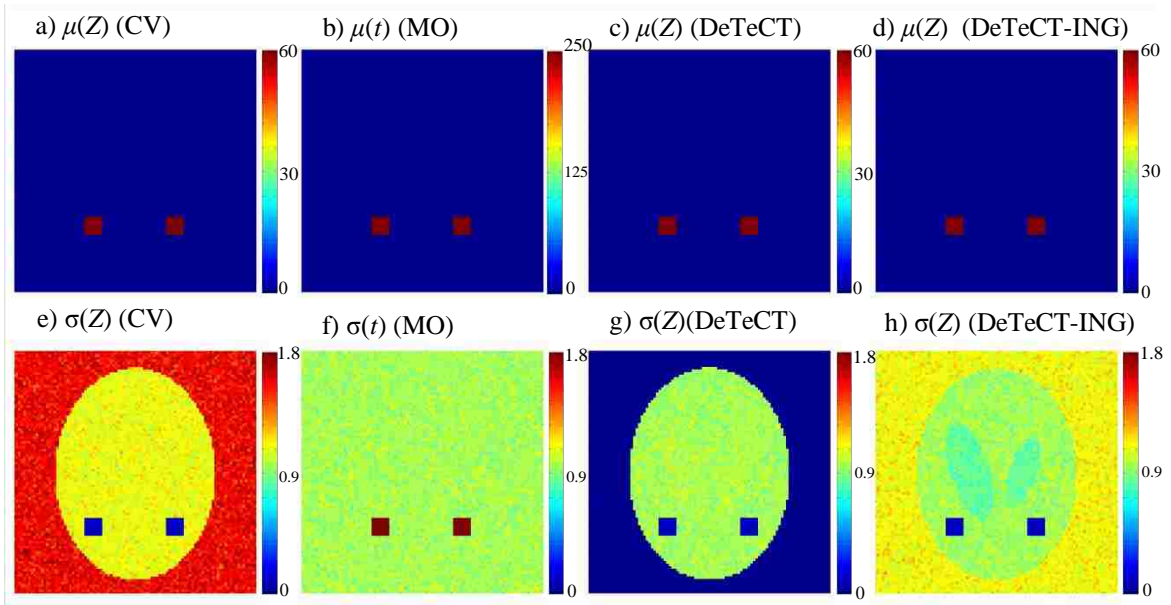
Figure 2.6: First row: Calculated sample means of the activation statistics (Z or t) of the models. a) $\mu(Z)$ (CV Model), b) $\mu(t)$ (MO Model), c) $\mu(Z)$ (DeTeCT Model), d) $\mu(Z)$ (DeTeCT-ING Model) Second row: Calculated sample standard deviations of the activation statistics (Z or t) of the models, e) $\sigma(Z)$ (CV Model), f) $\sigma(t)$ (MO Model), g) $\sigma(Z)$ (DeTeCT Model), h) $\sigma(Z)$ (DeTeCT-ING Model).

Table 2.9: The average voxel values of the sample standard deviation maps computed by using the DeTeCT-ING Model from the data generated by the model itself. The results are presented for the minimum theoretical values (Min. Theo.), and the estimates under the alternative (Alt) and null (Null) hypothesis.

SD	M_0			δ			β_1		
	M_0 Min. Theo.	M_0 Alt	M_0 Null	δ Min. Theo.	δ Alt	δ Null	β_1 Min. Theo.	β_1 Alt	β_1 Null
GM	0.0857	0.0048	0.0044	2.30E-06	2.30E-06	0	3.00E-06	3.00E-06	3.00E-06
WM	0.0537	0.0048	0.0044	2.30E-06	1.70E-06	0	3.00E-06	3.00E-06	3.00E-06
CSF	0.0718	0.0048	0.0044	0.4926	1.70E-06	0	3.00E-06	3.00E-06	3.00E-06
Out	0.2807	0.0063	0.0058	0	709.2	0	1.00E-06	4.00E-06	4.00E-06
ROI	0.0857	0.0048	0.0044	3.2462	0.1364	0	3.00E-06	3.00E-06	3.00E-06

SD	θ			σ^2		
	θ Min. Theo.	θ Alt	θ Null	σ^2 Min. Theo.	σ^2 Alt	σ^2 Null
GM	1.40E-06	1.40E-06	1.40E-06	4.00E-06	4.00E-06	4.00E-06
WM	1.40E-06	1.40E-06	1.40E-06	4.00E-06	4.00E-06	4.00E-06
CSF	1.40E-06	1.40E-06	1.40E-06	4.00E-06	5.00E-06	5.00E-06
Out	0	0.8375	0.8579	4.00E-06	4.00E-06	4.00E-06
ROI	1.30E-06	1.30E-06	1.30E-06	4.00E-06	4.00E-06	5.60E-06

We give a comparison between the CRLBs, which provide a quantitative measure of the attainable variance of parameter estimates, of the considered models in Tables 2.10 and 2.11. It can be observed from Table 2.10 and the results of a previous study (Rowe, 2005a) that the CRLB for the variance of the estimate of the observation variance is two times larger in the MO Model than in the CV Model. Table 2.11 shows that the CRLBs of the estimates of the common parameters of the DeTeCT and DeTeCT-ING Models are the same since these models have the same likelihood functions. It can also be seen from Tables 2.10 and 2.11 that the common parameters of all four models such as β_1 and θ appear to have the same CRLBs. The minimal theoretical standard deviations of the estimates of M_0, T_1 and T_2^* are higher compared to those of the other parameters. The DeTeCT and DeTeCT-ING Models appear to have higher CRLBs of the estimate of δ in CSF and ROI areas compared to the other areas. It should be noted here that the CRLBs of the MO and CV Models and the DeTeCT and DeTeCT-ING Models are not based on the same number of TRs since the first 20 observations are excluded for the MO and CV Models.

Table 2.10. The average voxel values of minimal theoretical standard deviation maps computed by using the MO and CV Models from the data generated by the DeTeCT-ING Model.

SD	MO				CV				
	β_0	β_1	β_2	σ^2	β_0	β_1	β_2	θ	σ^2
GM	0.0006	3.00E-06	0.0009	6.00E-06	0.0006	3.00E-06	0.0009	0.0001	5.00E-06
WM	0.0006	3.00E-06	0.0009	6.00E-06	0.0006	3.00E-06	0.0009	0.0001	5.00E-06
CSF	0.0006	3.00E-06	0.0009	6.00E-06	0.0006	3.00E-06	0.0009	0.0001	5.00E-06
Out	0.0006	3.00E-06	0.0009	6.00E-06	0.0006	3.00E-06	0.0009	0.0001	5.00E-06
ROI	0.0006	3.00E-06	0.0009	6.00E-06	0.0006	3.00E-06	0.0009	0.0001	5.00E-06

Table 2.11. The average voxel values of minimal theoretical standard deviation maps computed by using the DeTeCT and DeTeCT-ING Models from the data generated by the models themselves.

SD	DeTeCT						
	M_0	T_1	T_2^*	δ	β_1	θ	σ^2
GM	0.0857	0.0358	0.0052	0.00023	3.08E-06	1.44E-04	4.43E-06
WM	0.0537	0.0237	0.0053	0.00024	3.08E-06	1.42E-04	4.43E-06
CSF	0.0718	0.0158	8.8591	0.46598	3.08E-06	1.41E-04	4.43E-06
Out	0.2807	3.00E-13	1.14E-19	5.65E-20	9.54E-07	6.72E-12	4.43E-06
ROI	0.0857	0.0358	0.0052	3.2462	3.08E-06	1.38E-04	4.43E-06

SD	DeTeCT-ING				
	M_0	δ	β_1	θ	σ^2
GM	0.0857	0.000233	3.08E-06	1.44E-04	4.43E-06
WM	0.0537	0.000244	3.08E-06	1.42E-04	4.43E-06
CSF	0.0718	0.492673	3.08E-06	1.41E-04	4.43E-06
Out	0.2807	0	9.54E-07	6.72E-12	4.43E-06
ROI	0.0857	3.246212	3.08E-06	1.38E-04	4.43E-06

Part II: Simulated Data of Two Voxels with the Varying Parameter Setting

Figs. 2.7a, 2.7b and 2.8a, 2.8b illustrate the TPR and FPR plots against the varied parameter δ and α under scenarios "a" and "b", respectively. Furthermore, Fig. 2.8c shows the ROC curves plotted while α is varied under scenario "b". ROC curve at varying δ is not presented because the FPR computed from the inactive voxel is not affected by the varying parameter, δ, as it is zero for the inactive voxel. In the plots presented in Figs. 2.7 and 2.8, the colors red, green, blue and black represents the CV, MO, DeTeCT and DeTeCT-ING Models, respectively.

Figs. 2.7a and 2.7b show the plots of TPR and FPRs for each model against δ for an $\alpha = 0.05$ significance level, which are based on 1000 simulated time series with $\sigma^2=0.25$. As seen in Fig. 2.7a, even though TPRs of the models seem to coincide with

each other, the MO and CV Models have slightly higher TPRs especially at low δ values. However, there seems to be a trade-off between the TPRs and FPRs of the CV and MO Models, as Fig. 2.7b shows that FPRs of the CV and MO models are also higher than the DeTeCT and DeTeCT-ING Models' FPRs. This may be explained by the fact that our simulations are based on fitting the models to the data generated from the magnetization modeled by the DeTeCT and DeTeCT-ING Models. One can observe that the FPR of the DeTeCT and DeTeCT-ING Models do not converge to the significance level of α=0.05 in Fig. 2.7b, possibly due to some kind of bias that might have been created during the nonlinear numerical optimization process.
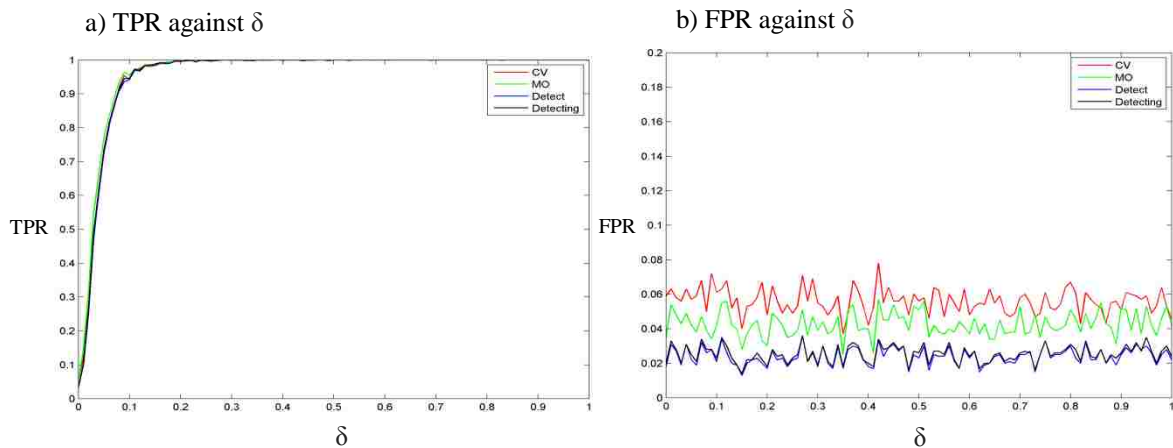
Figure. 2.7: a) TPR and b) FPR plots against the varied parameter, δ, under scenario "a" in which σ^2=0.25, and α=0.05.

Figs. 2.8a-2.8c show the plots of TPR and FPRs for each model against the significance level, α, as well as the ROC scatter plot generated at varying α for $\delta = 0.1$ for the active voxel, which are based on 1000 simulated time series with $\sigma^2 = 0.25$. The TPR plots of the CV, DeTeCT and DeTeCT-ING Models seem to slightly differ from each other whereas the MO Model has insignificantly higher TPRs at almost all α values.

As expected, it can be observed in Fig. 2.8b that the FPRs of the models increase with the significance level, α. Moreover, the DeTeCT and DeTeCT-ING Models show lower FPRs than the MO and CV Models at all α levels. ROC scatter plots in Fig. 2.8c show the full picture of trade-off between the TPR and FPR across a series of α values. Since more accurate activation detection model is expected to have a closer ROC curve to the upper-left border of the ROC space, the DeTeCT and DeTeCT-ING Models can be observed to be more accurate as producing less trade-off between FPR and TPRs. It can also be seen in Fig. 2.8c that the FPRs of the DeTeCT and DeTeCT-ING Models are not as high as the ones of the MO and CV Models at any significance level, α.
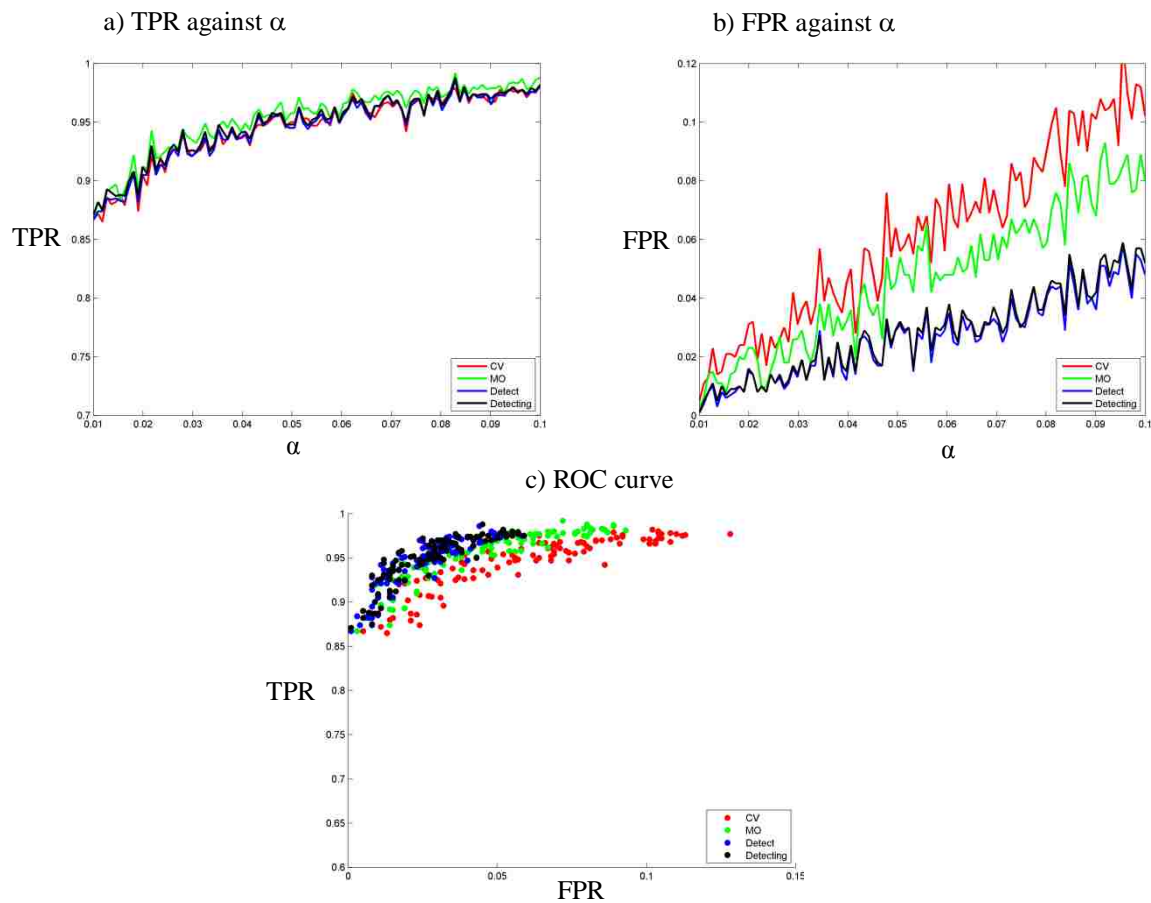
Figure. 2.8: a) TPR, b) FPR plots against the varied parameter, α, and (c) ROC curve under scenario "b" in which $\sigma^2 = 0.25$, and $\delta = 0.1$.

Fig. 2.9 shows the plots of CRLBs and the sample variances of the models'
parameters against δ for the single active voxel data generated based on scenario "c" in
which $\alpha = 0.05$, $\sigma^2 = 0.0001$ and δ varying from 0 to 1 with increments of 0.1. Since the
CV and MO Models do not include M_0, T_1, T_2^* and δ; the MO Model does not include θ;
and the DeTeCT and DeTeCT-ING Models do not include β_0 and β_2, the corresponding
panels of Fig. 2.9 do not include such parameters. Further, Fig. 2.10 shows the plots of
sample means and MSEs of the estimated σ^2's under each model against δ that are
computed from the same single voxel data generated under scenario "c". We prefer to
present the MSE plots of σ^2 since the MSEs of the other parameters are significantly
close to the variance plots presented in Fig. 2.9 as a result of low bias of the estimators.
In the plots presented in Figs. 2.9 and 2.10, the colors red, green, blue and black
represents the sample variances, MSEs or sample means of the CV, MO, DeTeCT and
DeTeCT-ING Models, whereas in Fig. 2.9, pink, cyan, and yellow represents the CRLBs
of the CV, MO, and DeTeCT/DeTeCT-ING Models, respectively. As noted before, the
DeTeCT and DeTeCT-ING Models have the same CRLBs since these models have the
same likelihood functions.

It can be seen in Figs. 2.9a, 2.9c and 2.9d that the sample variances of the
estimated M_0, T_2^* and δ for the DeTeCT model (in blue) appear to be close but not
coincident to the CRLB values (in yellow) whereas the sample variances of the estimated
M_0 and δ for the DeTeCT-ING model (in black) can be observed to be lower than CLRBs
(in yellow) at all δ values. The sample variance plot of the estimated T_1 that is given in
Fig. 2.9b appears to coincide with its CRLB at α values higher than 0.4. It can be seen in
Fig. 2.9e that the variances of β_1 for all models achieve their CRLBs. It should be noted

a) CRLB and sample var. of M_0 b) CRLB and sample var. of T_1 c) CRLB and sample var. of T_2^*

d) CRLB and sample var. of δ e) CRLB and sample var. of β_1 f) CRLB and sample var. of θ

g) CRLB and sample var. of β_0 h) CRLB and sample var. of β_2 i) CRLB and sample var. of σ^2
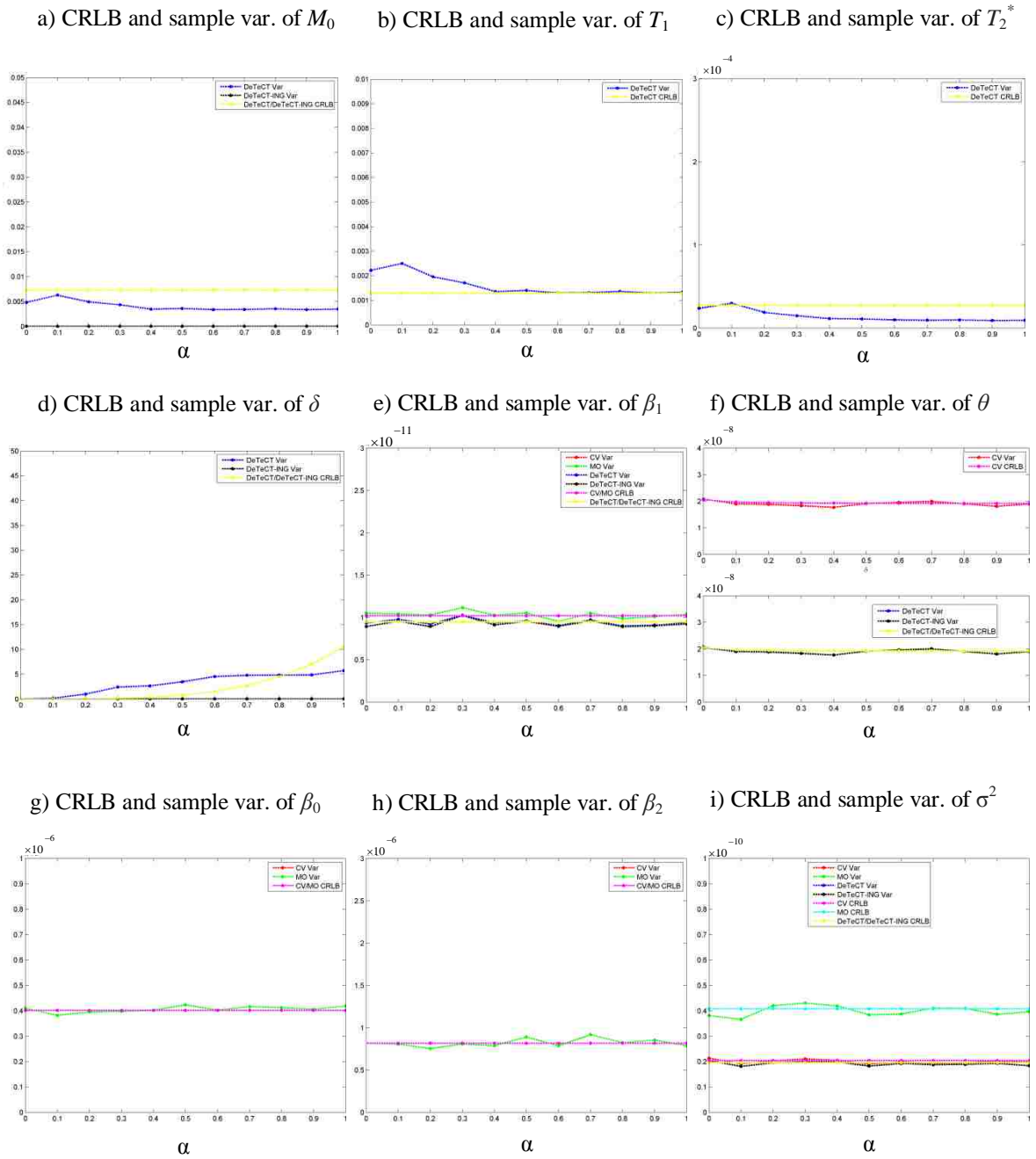
Figure 2.9: CRLB and sample variance plots of the parameters against δ for the single active voxel data generated based on scenario "c" in which $\alpha = 0.05$, $\sigma^2 = 0.0001$. a) M_0, b)T_1, c) T_2^*, d) δ, e) β_1, f) θ, g) β_0, h) β_2, and i) σ^2.

here that the DeTeCT and DeTeCT-ING Models' CRLBs (yellow) are lower than the CV and MO Models' CRLBs (pink) for the coefficient β_1. In Figs. 2.9f and 2.9g, the variance of θ appears to achieve its CRLBs for all models considered. Further, the variances of the coefficients β_0 and β_2 for the CV and MO Models (in red and yellow), presented in Figs. 2.9h and 2.9i, appear to achieve their CRLBs (in pink). Error variance estimate, given in Fig. 2.9i, are approximately twice as large for the MO Model than for the CV, DeTeCT and DeTeCT-ING Models. This observation was verified by the fact that the CRLB for the variance of the observation variance is two times larger in the MO Model than the CV Model (Rowe, 2005a). As such, the CRLBs for the variance of σ^2 in the DeTeCT and DeTeCT-ING Models are also found to be very close to the CRLBs for the variance of σ^2 in the CV Model. Furthermore, the estimated variances of all models appear to be very close to their corresponding CRLBs.

In Fig. 2.10a, we present the computed sample means of σ^2 for all models as well as the true σ^2 value that we used when generating the data. Furthermore, we present the MSEs of σ^2 for the models at varying δ in Fig. 2.10b. It can observed in Fig 2.10a that the sample means of σ^2 computed from the CV, DeTeCT and DeTeCT-ING Models appear to be very close to each other and also to the true σ^2 value. The MO Model seems to produce a lower error compared to the other models mostly at higher δ points. However, as a result of the MO Model's higher minimal theoretical error variance, the MSE of σ^2 for the MO Model appears to be higher than the other models, as it can be seen in Fig. 2.10b. Furthermore, the DeTeCT and DeTeCT-ING Models seem to have slightly lower MSEs for σ^2 than the CV Model. Since the MSE decomposes into a sum of the bias and

variance of the estimator, MSE of the estimators need to be as small as possible in order to achieve a good estimation performance.
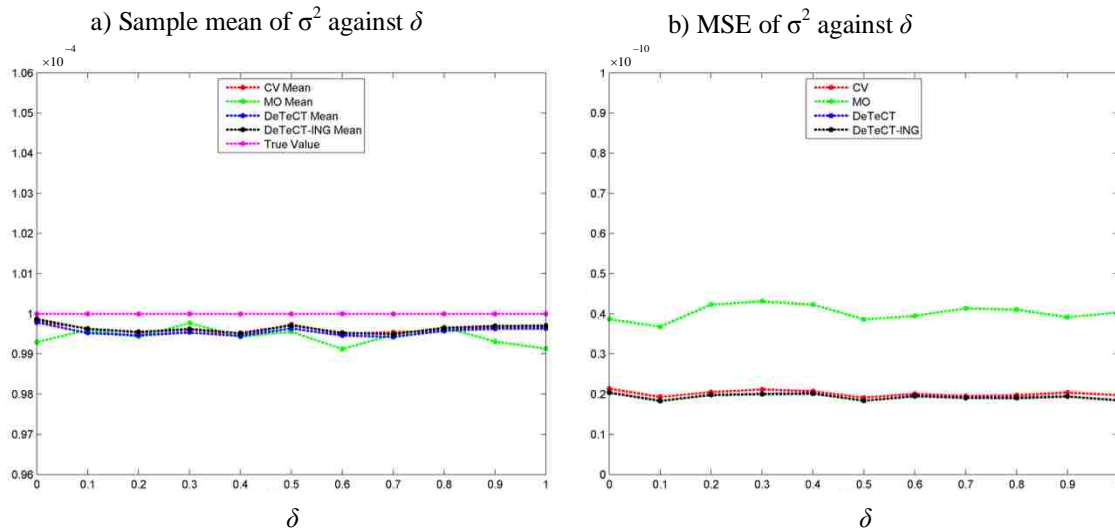
Figure 2.10: a) Sample mean, and b) MSE plots of σ^2 against δ for the single active voxel data generated based on scenario "c" in which $\alpha = 0.05$, $\sigma^2 = 0.0001$.

In general, the parameter estimates for the CV, DeTeCT and DeTeCT-ING Models appear to be more efficient than the MO Model at the considered δ levels. It should also be noted here that the CV and MO Models provide only activation detection whereas the DeTeCT and DeTeCT-ING Models extracts more information from fMRI data by also providing M_0, T_1 and T_2^* estimates as illustrated in Fig. 2.5. Lower variance and bias of the variance estimator, σ^2 implies a more stable variance of the model. Furthermore, lower mean of the variance estimator σ^2 provides better stability of the other parameter estimates since the CRLBs of all estimators depend on σ^2. As such, a better accuracy and stability in the parameter estimates of the DeTeCT and DeTeCT-ING Models can lead to better activation detection by providing lower FPRs and higher TPRs, especially at extreme situations such as at low δ and very low or high α levels.

2.4.3 Human Subject Data Results

The "noise" in the acquired human subject data is often plagued by the physiological effects and possible motion. Nonlinearity and the number of the parameters to be estimated in the system as well as the noise in the acquired data may pose computational difficulty when performing the nonlinear least squares estimation. A good selection of initial values of the parameters can be helpful to overcome such problems. In order to develop a hybrid approach to the nonlinear estimation, the MLEs of M_0, β_1, and θ were analytically driven under the restricted null hypothesis of the DeTeCT-ING Model to be used as initial values. The derivations of the MLEs of the null hypothesis of the DeTeCT-ING Model are given in Appendix B.

The tissue parameter maps, M_0, T_1, and T_2^*, estimated from the alternative hypothesis of the DeTeCT Model given in Eq. [2.21] by using the numerical nonlinear estimation are shown in Figs. 2.11a-2.11c. It can be observed that M_0 and T_1 values are highly indicative of GM bordered in Figs. 2.11a and 2.11b. As it is given in Table 2.1, the GM T_1 values appear to be higher than WM T_1 values. Although the tissue segmentation in T_2^* map, presented in Fig. 2.11c, does not appear to be as good as the one in T_1 map, presented in Fig. 2.11b, corresponding tissues can still be distinguished.

Figs. 2.12a-2.12c show the computed activation maps using the likelihood ratio test from the CV, MO and DeTeCT-ING Models, respectively. Fig. 2.12 shows a high correspondence between decay coefficients deemed to be GM and bordered active areas that should be in GM. It can be observed that the CV and DeTeCT-ING Models demonstrate superior power of detection over the MO Model in left motor cortex and supplementary motor area in which the activation occurs. A higher power of detection

can be seen in the bordered left motor cortex in Fig. 2.12c compared to the corresponding areas in Figs. 2.12a and 2.12b. This observation is consistent with the outcomes of our simulation study presented in Fig. 2.8 in Part II of section 2.4.2 which shows that the DeTeCT-ING Model has a better activation detection power than the CV and MO Models after applying a 5% Bonferroni family-wise error rate thresholding. Fig. 2.12c also shows that the DeTeCT-ING Model produces no false positives outside brain unlike the CV Model. Even though the false positive detections of this kind, which are distant from the tissues, can be easily masked, this outcome can be considered as the evidence of the DeTeCT-ING Model's benefit of theoretically eliminating false positive rates without the need of researchers' decision for manual masking after the statistical analysis of the observed fMRI data. A few false positives that are not present in the activation maps of the CV or MO Models, in Figs. 2.12a and 2.12b, can be observed in the upper left side of the brain which is very close to no signal area in Fig. 12c. Such false positives can be caused by the signal changes due to the non-uniform sources of noise and artifact that are hard to be described and modeled. Furthermore, the assumption of independence of the observations in time or space may not be true in the human subject data. Such assumptions that are difficult to be satisfied can cause poor estimates and thus false positive rates especially in the areas near the edges of the brain. As such, these voxels that are incorrectly detected as active most possibly have task related signal changes that are of no biological origin.
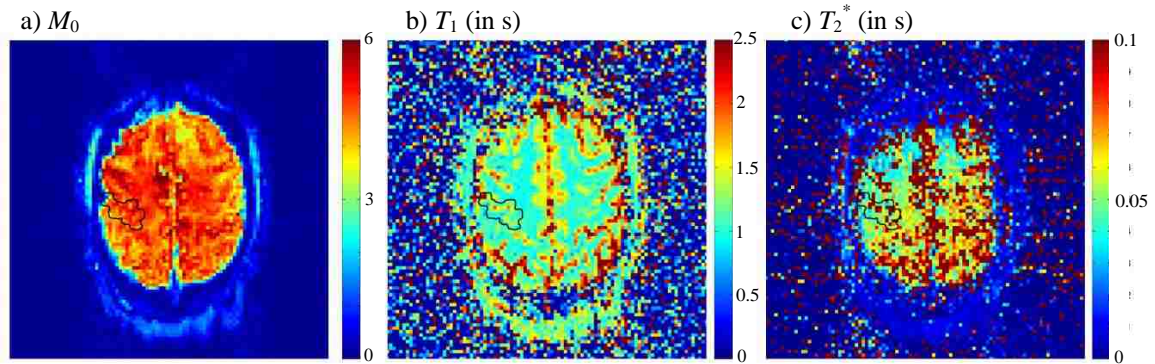
Figure 2.11: Estimated M_0, T_1, and T_2^* maps from the alternative hypothesis of the DeTeCT Model. a) M_0, b) T_1 (in s), c) T_2^* (in s).
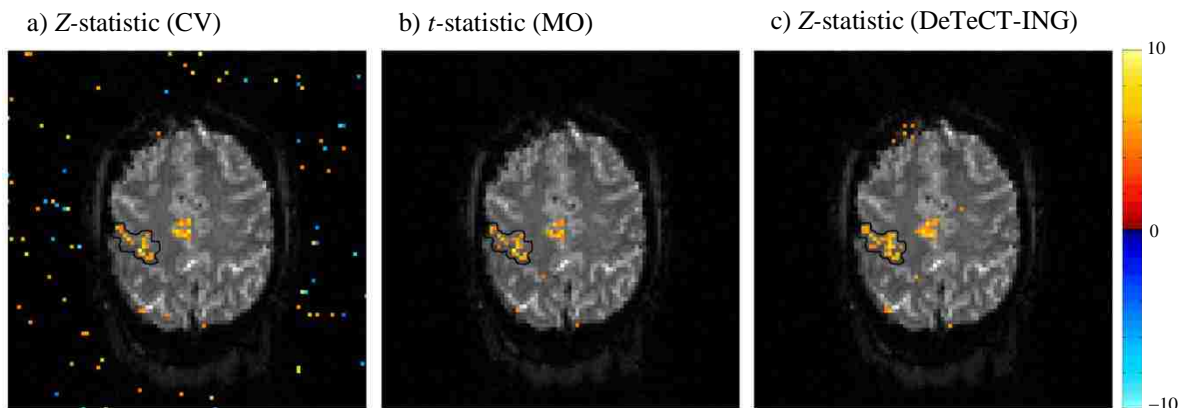
Figure 2.12: Human subject data activation statistic maps computed by using the CV, MO, DeTeCT-ING Models. a) Z-statistics map from the CV Model, b) t-statistics map from the MO Model, and c) Z-statistics map from the DeTeCT-ING Model. The presented maps are thresholded at a 5% Bonferroni family-wise error rate.

2.5   Discussion

This chapter proposes a new statistical fMRI model for differential T_2^* contrast, so called the DeTeCT-ING Model, by incorporating T_1 and T_2^* of gray matter tissue, considering the fact that the active voxels are located in gray matter. Furthermore, the physical magnetization equation is included into the model rather than using a linear model to describe the magnetization. Unlike the previously presented fMRI activation

models, the first scans of the fMRI data are not discarded since they have biological

information about the brain, including the tissue parameters such as relaxation parameter

and spin density of the tissues.

The selection of the imaging parameters, TR, TE and flip angle, plays an

important role for determining accurate measure of tissue parameters. The acquisition

parameters for this study are selected to be appropriate for both T_1 and T_2^* estimation and

brain activation detection since we perform them from a single pulse sequence. The

selection of 90° flip angle is made in order to simplify the temporarily varying magnitude

M_t, given in Eq. [2.17] so that the magnetization at time for the DeTeCT and DeTeCT-

ING Models does not depend on the magnetization at previous time points. As such, the

computational complexity of the numerical optimization of the log likelihood function is

relatively reduced. It should be noted here that it is possible to reduce TR and TE to

increase T_1 and T_2^* contrast since T_1 and T_2^* are influenced by TR and TE, respectively.

There are three main contributions of the developed model to the current studies

in the field by utilizing the aforementioned neglected information. First, the proposed

method provides a significant step to modeling the fMRI data closer to that actually seen

in the real experiments with the use of physical magnetization equation. Second,

utilization of the gray matter tissue relaxation parameters in the statistical fMRI

activation model provide a theoretical elimination of the possible false positives in the

process of hypothesis testing while computing activation statistics. Third, the model

allows one to simultaneously estimate the relaxation parameters which could be used for

tissue characterization, by utilizing the information in the first few images.

Chapter 3: Incorporating MR Relaxivities to More Accurately Reconstruct MR Images

The mathematical models that have been used for detecting brain activity, that are introduced in the previous chapter, and the models that determine brain connectivity use the reconstructed image measurements rather than directly using the acquired frequency space measurements. These models do not take into account the artifacts that are based upon the physical mechanisms that occur in the signal encoding and data acquisition processes. As such, the accuracy of the final analyses performed by the fMRI and fcMRI models significantly depends on the accuracy of the reconstructed image measurements. In MRI, the complex-valued measurements of the acquired signal at each point in the frequency space are expressed as a Fourier transformation of the proton spin density weighted by Fourier encoding anomalies: T_2^* and T_1 relaxation times, and a phase determined by the magnetic field inhomogeneity, ΔB, according to the MR signal equation. Such anomalies alter the expected symmetry and the signal strength of the k-space observations, resulting in images distorted by image warping, blurring, and loss in image intensity. Although T_2^* and ΔB corrections have been a focus of research, the T_1 recovery term is typically neglected by assuming a long repetition time. As T_1 relaxation time provides valuable quantitative information on tissue characteristics, the model presented in this chapter aims to account for the effects of T_2^*, ΔB and T_1 during the image reconstruction. Accounting for T_1 effects in image reconstruction is shown to recover image contrast that exists prior to T_1 equilibrium. The use of the proposed model in future studies could provide better precision in image registration by improving tissue

segmentation. Such correction is also shown to induce negligible correlation in the reconstructed images and preserve functional activations.

3.1   Introduction

In fMRI, data is acquired in the spatial frequency domain and reconstructed through an inverse Fourier transform, into images of the object in the image domain. Thus, the measured k-space data, encoded in time, is ideally assumed to be the Fourier transform of the proton spin density. However, in the process of Fourier encoding, the detected MRI signal is subject to the MR relaxivities, T_2^* and T_1, as well as magnetic field inhomogeneity, ΔB, commonly referred to as Fourier anomalies. The nature of the Fourier encoding process causes image artifacts or image distortions. One such effect is the one caused by acquiring measurements of k-space at different times after the RF excitation pulse. Due to the non-instantaneous acquisition of each k-space line, the first points sampled have a lower T_2^* weighting than the subsequent points. Considering that the "ideal" image would be reconstructed from the "ideal" k-space measurements, in which every point is sampled with the exact same weighting, the "actual" acquired k-space measurements in practice are scaled according to the time by a factor determined by T_2^* (Stroman, 2011; Haacke et al., 1999). As such, the "actual" reconstructed image, which is obtained by an inverse Fourier transformation of the "actual" k-space measurements, has a blurring effect in the phase encoding direction as a result of the inverse Fourier transformation of this weighting pattern. Moreover, the differences in magnetic susceptibility between tissues or magnetic materials lead to incorrect sampling of k-space by introducing errors in the gradients. Thus, the point in k-space that is believed to be sampled is not the actual location. As such, magnetic field inhomogeneities incur spatial

distortions including image warping and phase generation. Although the weighting through T_1 is not affected by the non-instantaneous sampling of k-space, it can modulate the MR signal resulting in signal loss and image weighting that depend on the tissue characteristics. The artifacts resulting from T_2^* relaxation during sampling, the inhomogeneities in the magnetic field, and the alteration in the signal arising from the longitudinal relaxation can be considered as T_2^*, ΔB and T_1 effects, respectively,

Correcting the image warping effects of both the static and dynamic magnetic field inhomogeneities (Jezzard and Balaban, 1995; Reber et al., 1998; Kannengiesser et al, 1999; Hahn and Rowe, 2012; Hahn et al., 2012), and the T_2^* blurring effect (Maclaren et al., 2008; Bernstein et al., 2004, Zhou et al., 1993; Robitaille and Berliner, 2007) in echo planar imaging sequences have been active areas of research in brain imaging. Despite such efforts for correcting T_2^* and ΔB effects, conventional studies do not account for a recovery of the longitudinal relaxation time; instead they use the standard assumption of a long repetition time. However, this assumption is not always valid, and the signal amplitude becomes dependent on T_1 when performing fast repetitive image excitations with incomplete recovery of the longitudinal magnetization. Moreover, T_1 relaxation time provides a robust contrast mechanism for distinguishing tissue type (Mazaheri et al., 2006). As such, this quantitative knowledge of tissue characteristics, which can be extracted from data acquired during the transient state prior to T_1 equilibrium, can be incorporated into the reconstructed time series image-space. As noted before, the Fourier anomalies appear as exponential terms in the traditional signal equation, the observed k-space measurements can be considered as the Fourier transform of the proton spin density, weighted by the Fourier anomalies. Since the k-space measurements are subject to the

effects of such weighting during data acquisition, these effects can be accounted for separately or simultaneously in the process of Fourier reconstruction.

In order to relate the signal and noise characteristics of k-space measurements to reconstructed voxel measurements, the complex-valued matrix application of the inverse Fourier transformation was described through a real-valued isomorphism by Rowe et al. (2007). Representing the Fourier reconstruction as a single matrix operator formed the basis for the study in (Nencka et al., 2009a) where a mathematical framework, AMMUST-k (A Mathematical Model for Understanding the STatistical effects of k-space preprocessing), was developed to represent various spatial processing operations performed on acquired spatial frequencies in terms of real-valued linear isomorphisms. Representing the reconstruction and image processing operations in this way made it possible to directly compute the exact covariance structure, and ultimately correlation induced into the image-space data, which can result in misleading conclusions in fcMRI and fMRI studies (Nencka et al., 2009; Bruce et al., 2011).

In this chapter, we expand upon the AMMUST-k framework by modifying the real-valued Fourier reconstruction (FR) operator in such a way that it can account for the effects of T_2^*, ΔB, and T_1 on the image-space data. As noted before, the measured "actual" k-space data is scaled according to time that has elapsed since the RF excitation pulse and the factor determined by the terms include T_2^*, ΔB, and T_1. As such, we first develop a real-valued Fourier encoding (FE) operator that considers such weighting, then, we create the modified FR operator by simply inverting the modified FE operator to account for the encoding effects in image space. The use of a modified FR operator within this framework makes it possible to more accurately reconstruct the image space

voxel values from measured spatial frequencies, and also precisely quantify the statistical effects of such correction on the reconstructed data.

The linear Fourier reconstruction operators are first developed by considering different combinations of the Fourier anomalies and examples of each anomaly are shown on a small 8×8 data set. The Fourier operators are then used to theoretically examine the image space data associated with the effects of the Fourier anomalies on a 96×96 noiseless digital phantom. The exact mean and induced correlations modified by the adjusted FR operators on both complex-valued and magnitude-squared data are also illustrated by using the proposed model. The results of the proposed FE anomaly correction framework is also illustrated on acquired experimental human subject fMRI data by focusing on the incorporation of the longitudinal relaxation time, T_1. Finally, a comparison is made between the activation statistics computed from the reconstructed data with and without the incorporation of T_1 effects with the use of both conventional magnitude-only (Bandettini et al., 1993) and newer complex-valued fMRI activation models (Rowe and Logan, 2004; Rowe, 2005a,b).

3.2   Theory

3.2.1   Complex-valued Image Reconstruction in MRI

In fMRI, complex-valued measurements are acquired discretely in time corresponding to two-dimensional spatial frequency measurements. The measurements are then reconstructed into a complex-valued image by applying the complex-valued inverse Fourier transformation. Although the original object, proton spin density, is real-valued, imperfections in the imaging process lead to a complex-valued image.

When the complex-valued Fourier reconstruction is described through a real-valued isomorphism (Rowe et al., 2007), a vector of the reconstructed image, y, can be written as the product of a FR operator, Ω, with a vector of the observed k-space observation, s, by

$$y = \Omega s . \qquad [3.1]$$

Similarly, the vector of the k-space observation, s, can be written as the product of a FE operator, $\bar{\Omega} = \Omega^{-1}$, with a vector of the reconstructed image, y, as

$$s = \bar{\Omega} y . \qquad [3.2]$$

In Eqs. [3.1] and [3.2], $y = (y_R', y_I')'$ is a $2p \times 1$ vector with the real parts of p image values, $y_R = (y_{R1}, \ldots, y_{Rp})'$, stacked above the imaginary parts of p image values, $y_I = (y_{I1}, \ldots, y_{Ip})'$, for an $u \times v$ image of $p = uv$ voxels. Similarly, $s = (s_R', s_I')'$ is a $2p \times 1$ vector with p real parts, $s_R = (s_{R1}, \ldots, s_{Rp})'$, stacked above p imaginary parts, $s_I = (s_{I1}, \ldots, s_{Ip})'$, for a Cartesian acquisition of k-space. Thus, the FR and FE operators, Ω and $\bar{\Omega}$, have dimensions of $2p \times 2p$. The Cartesian FR operator can be represented as

$$\Omega = \begin{pmatrix} \mathrm{Re}(\Omega_C) & -\mathrm{Im}(\Omega_C) \\ \mathrm{Im}(\Omega_C) & \mathrm{Re}(\Omega_C) \end{pmatrix}, \qquad [3.3]$$

where $\mathrm{Re}(\cdot)$ and $\mathrm{Im}(\cdot)$ denote the real and imaginary parts of their respective arguments. The matrix Ω_C is defined as the Kronecker product of the matrices, Ω_x and Ω_y, as $\Omega_C = \Omega_x \otimes \Omega_y$, where the matrices Ω_x and Ω_y Fourier transform the columns and the rows of the acquired k-space measurements, respectively. The jk^{th} element of the FR operator Ω_x can be written as $(\Omega_x)_{jk} = w^{((-n/2)+(j-1))((-n/2)+(k-1))}$, where j and k are the indices from 1 to n and $w = (1/n)\exp(i2\pi/n)$. The Fourier encoding operator, $\bar{\Omega}$, has a similar skew

symmetric form to Ω where $w=\exp(-i2\pi/n)$. The operators, Ω and $\overline{\Omega}$, will be considered as the standard FR and FE operators as they do not account for any Fourier anomalies.

As the real-valued spatial frequency vector, s, contains complex-values, the application of the FR operator in Eq. [3.1] produces a covariance between the real measurements, between the imaginary measurements, and between the real and imaginary measurements. If the k-space vector, s, has a covariance matrix, Γ, then the covariance matrix of the reconstructed image, y, becomes

$$\text{cov}(y) = \Omega\Gamma\Omega', \qquad\qquad\qquad [3.4]$$

where the operator "$'$" denotes the transpose of a matrix.

To produce the required k-space vector, s, the acquired k-space array, which is observed as a pairing of real and imaginary component of each frequency can be reordered by reversing the alternating rows of measurements and segregating real and imaginary observations through permutation matrices, P_A and P_S. Since the k-space data includes extra points acquired during the phase encoding blips in echo planar imaging, the acquired measurements also needs to be censored by the censoring matrix, P_E. Additionally, Nyquist ghosting can be corrected through a series of linear operators that reorders to group the real and imaginary observations from each line together (P_R), Fourier transform each row (Ω_R), shift the phase of the each transformed row (Φ_N), and finally apply the inverses of Ω_R and P_R. These k-space operators together with additional operators that can include Fourier homodyne interpolation, H, zero-filling, F, apodization, A, and explicit image space smoothing operator, S, can be combined into a single operator, O, that signifies the series of all linear operators applied to s (Nencka et al., 2009). Therefore, the reconstruction in Eq. [3.1] simplifies to

$$y = Os \, , \tag{[3.5]}$$

where O represents a multiplication of operators applied throughout the image reconstruction process,

$$O = S\Omega AFHP_R^{-1}\Omega_R^{-1}\Phi_N\Omega_R P_R P_S P_A P_E \, . \tag{[3.6]}$$

If $E(s) = s_0$ and $\Gamma = \mathrm{cov}(s)$, then mean and covariance of the reconstructed image vector, y, are altered by the final operator, O, to become

$$E(y) = Os_0$$

and

$$\mathrm{cov}(y) = O\Gamma O' \, . \tag{[3.7]}$$

The correlation structure between voxels in y can be calculated from $cov(y)$ by

$$corr(y) = D^{-1/2}O\Gamma O'D^{-1/2} \, , \tag{[3.8]}$$

where D is a diagonal matrix of the variances drawn from the diagonal of the covariance matrix, $O\Gamma O'$, and the $-1/2$ superscript denotes that the diagonal elements are inverted after taking the square root. The covariance matrices of both the spatial frequencies and the reconstructed image-space values include the following covariance pairs: real by real, imaginary by imaginary, and real by imaginary components of s and y, respectively.

An assumption of normality allows the derivation of the covariance of the square of the magnitude data from the covariance matrix, $cov(y) = O\Gamma O'$ (Rowe and Nencka, 2009; Nencka et al., 2009). Both magnitude-squared and complex-valued data can be used to analyze changes made to the acquired correlation structures as the correlation of

magnitude-squared data is asymptotically equivalent to the magnitude-only correlation and linear in nature.

3.2.2   Acquired *k*-space Signal and Fourier Anomalies

Under the assumption that the complex-valued matrix of two dimensional spatial frequencies is measured instantaneously at the echo time, TE, the acquired *k*-space signal can be expressed through the MR signal equation,

$$s(k_x, k_y) = \int_{-\infty}^{\infty} \int_{-\infty}^{\infty} M_0(x, y)\left(1 - e^{-TR/T_1(x,y)}\right) e^{-TE/T_2^*(x,y)} e^{i\gamma\Delta B(x,y)TE} e^{-i2\pi(k_x x + k_y y)} dx dy \,, \qquad [3.9]$$

where TR is the repetition time and $M_0(x,y)$ is the proton spin density. The gyromagnetic ratio, γ, of the hydrogen nuclei is equal to 42.58 MHz/T in Eq. [3.9].

Since the signal for different points in *k*-space is measured at different times, the *k*-space observation process occurs over a finite duration of time and the signal equation in Eq. [3.9] can be more accurately expressed as

$$s(k_x, k_y) = \int_{-\infty}^{\infty} \int_{-\infty}^{\infty} M_0(x, y)\left(1 - e^{-TR/T_1(x,y)}\right) e^{-t/T_2^*(x,y)} e^{i\gamma\Delta B(x,y)t} e^{-i2\pi(k_x x + k_y y)} dx dy \,, \qquad [3.10]$$

where the *k*-space point (k_x, k_y) is sampled at time $t = t(k_x, k_y)$. As the variable $t = t(k_x, k_y)$ varies for each *k*-space measurement, both T_2^* and ΔB break the Hermitian symmetry of the *k*-space observations, and could therefore cause artifacts and distortions in the reconstructed images. Moreover, the longitudinal relaxation time, T_1, causes changes in signal intensity depending on the tissue characteristics.

In conventional studies, the term $(1-\exp(-TR/T_1))$ in Eq. [3.10] is assumed to be approximately 1, by choosing TR to be much greater than T_1. This reduces Eq. [3.10] to depend only on T_2^* by

$$s(k_x,k_y) = \int_{-\infty}^{\infty} \int_{-\infty}^{\infty} M_0(x,y)e^{-t/T_2^*(x,y)}e^{i\gamma\Delta B(x,y)t}e^{-i2\pi(k_x x+k_y y)}dxdy , \qquad [3.11]$$

and thus leads to T_2^*-weighted images.

The assumption of an infinite TR however can never be reached directly since the goal is to image the brain as quickly as possible, thus fast acquisitions are needed. The neglected term, $(1-\exp(-TR/T_1))$, therefore takes non-negligible values with the parameter settings that are commonly used in fMRI experiments. Presented in Table 3.1 are the values that $(1-\exp(-TR/T_1))$ outputs when the relaxation parameter values of GM and WM tissues measured at 3.0 T (Atlas, 2008) and two commonly used TR values, 1000 ms and 2000 ms, are used. It is of note here that the value of $(1-\exp(-TR/T_1))$ is expected to be slightly lower at 7.0 T which has been widely used in high-field fMRI for study of the human brain. Furthermore, the variations in the value of TR have an essential effect on the control of image contrast characteristics. As such, accounting for T_1 effects has the potential of retaining the image contrast over the time series that exists prior to T_1 equilibrium. The regular FR operator, Ω, is thus modified with the aim of analyzing and accounting for the effects of Fourier anomalies: T_2^*, ΔB and T_1.

Table 3.1: T_1 exponential term values at 3.0 T.

1-exp(-TR/T_1(x,y))	TR = 1000 ms	TR = 2000 ms
GM (T_1 = 1331 ms.)	0.5283	0.7750
WM (T_1 = 832 ms.)	0.6994	0.9096

3.2.3 Incorporating MR Relaxivities in the Fourier Reconstruction Process

In this section, we develop a modified Fourier image reconstruction operator that produces the "ideal" image space vector, y_{Id}, from the "actual" measured k-space vector, s_{Act}, that is affected by the exponential terms for T_2^*, ΔB, and T_1 during the Fourier encoding process. Consider that the "ideal" image space vector, y_{Id}, would be constructed from the "ideal" k-space vector, s_{Id}, that is not affected by FE anomalies and the "actual" measured signal, s_{Act}, that we acquire in practice is scaled according to a weighting determined by FE anomalies.

As each k-space measurement is approximately expressed as the forward Fourier transform of the spin density, weighted by the MR relaxivities and the magnetic field inhomogeneities at a single point in k-space, we can first incorporate the exponential terms for T_2^*, T_1, and ΔB into the FE operator, $\overline{\Omega}$. Then, we construct the modified FR operator by simply taking the inverse of the modified FE operator matrix.

As with the Cartesian Fourier reconstruction operator given in Eq. [3.3], the Cartesian FE operator is expressed as

$$\overline{\Omega} = \begin{pmatrix} \operatorname{Re}(\overline{\Omega}_C) & -\operatorname{Im}(\overline{\Omega}_C) \\ \operatorname{Im}(\overline{\Omega}_C) & \operatorname{Re}(\overline{\Omega}_C) \end{pmatrix}, \qquad\qquad [3.12]$$

where $\overline{\Omega}_C$ is defined as $\overline{\Omega}_C = \overline{\Omega}_x \otimes \overline{\Omega}_y$, and the jk^{th} element of $\overline{\Omega}_x$ can be written as

$(\overline{\Omega}_x)_{jk} = w^{((-n/2)+j)((-n/2)+k)}$ when $w = \exp(-i2\pi/n)$.

Regardless of the relaxation times or ΔB that cause the weighting difference, in the general case, we can describe the weighting of the MR signal at each point with a two-dimensional array, W, as

$$W(k_x, k_y, x, y) = \left(1 - e^{-TR/T_1(x,y)}\right) e^{-t\left(k_x, k_y\right)/T_2^*(x,y)} e^{i\gamma\Delta B(x,y)t\left(k_x, k_y\right)} .$$ [3.13]

Two dimensional FE anomaly weighting function, W, can be constructed as

$$W(k_x, k_y, x, y) = \begin{bmatrix} W(1,1,1,1) & \cdots & W(u,v,1,1) \\ \vdots & \ddots & \vdots \\ W(1,1,u,v) & \cdots & W(u,v,u,v) \end{bmatrix},$$

for an $u \times v$ image.

In order to achieve the ideal image space vector, y_{Id}, after reconstruction, we first modify $\bar{\Omega}$ in Eq. [3.12], by including W into the real-valued isomorphism. The modified FE operator, $\bar{\Omega}_a$, can be created by first performing an element-wise multiplication of the Kronecker product, $\bar{\Omega}_a$, by the FE anomaly weighting function as

$$\bar{\Omega}_{C,a} = \left(\bar{\Omega}_x \otimes \bar{\Omega}_y\right) \circ W\left(k_x, k_y, x, y\right),$$ [3.14]

where $\circ$ represents an element-wise Hadamard product.

Finally, the modified FE operator, $\bar{\Omega}_a$, can be expressed as

$$\bar{\Omega}_a = \begin{pmatrix} \text{Re}\left(\bar{\Omega}_{C,a}\right) & -\text{Im}\left(\bar{\Omega}_{C,a}\right) \\ \text{Im}\left(\bar{\Omega}_{C,a}\right) & \text{Re}\left(\bar{\Omega}_{C,a}\right) \end{pmatrix}.$$ [3.15]

The modified FR operator, Ω_a, can then be calculated by $\Omega_a = \bar{\Omega}_a^{-1}$.

With the modified Fourier FR operator that accounts for the effects of the FE anomalies, the operator, O, in Eq. [3.6] can be updated to

$$O_a = S\Omega_a AFHP_R^{-1}\Omega_R^{-1}\Phi_N\Omega_R P_R P_S P_A P_E .$$ [3.16]

The complete process given in Eq. [3.5] can be written in such a way that the operator, O_a, reconstructs the "actual" measured k-space vector, s_{Act}, into the "ideal" corrected image space vector, y_{Id}, as

$$y_{Id} = O_a s_{Act} .$$ [3.17]

The inclusion of T_2^*, ΔB, and T_1 finely alters the structure of the standard FE and FR operators, $\overline{\Omega}$ and Ω to arrive at $\overline{\Omega}_a$ and Ω_a. The alterations caused by the FE anomalies in the FE operator, and in the FR operator that accounts for such alterations can be better seen in a low-dimensional example than a real size data set. Presented for an 8×8 example, the 128×128 arrays in Figs. 3.1a and 3.1b are the FE and FR operators that either do not account for any terms (standard operators), or separately accounts for the T_2^* decay, ΔB in the frequency encoding direction, and the T_1 recovery term. T_2^* and T_1 maps were considered in the example map which were scaled to values from 80 to 100 ms and 800 to 1000 ms inside the phantom, respectively. The ΔB term was modeled as a linear gradient ranging from 0 to $2.5×10^{-6}$ T. It can be seen in the second panel of Fig. 3.1a that the modified FE operator that includes T_2^* is visually different from the standard FE operator. Since $\exp(-t/T_2^*)$ in Eq. [3.13] converges to 0 for the voxels that have small T_2^* values, the element values of the modified FE operator tend toward zero in the portions that correspond to these voxels with low T_2^* value. Moreover, it can be seen in the third panels of Figs. 3.1a and 3.1.b that the incorporation of T_1 recovery causes a significant amplitude change in the modified FE and FR operators for the considered TR of 1 s. The operators that incorporate ΔB effects that are given in the fourth panel of Fig. 3.1a and 3.1b appear to be clearly different than the standard arrays as a result of the linear gradient change in magnetic field.
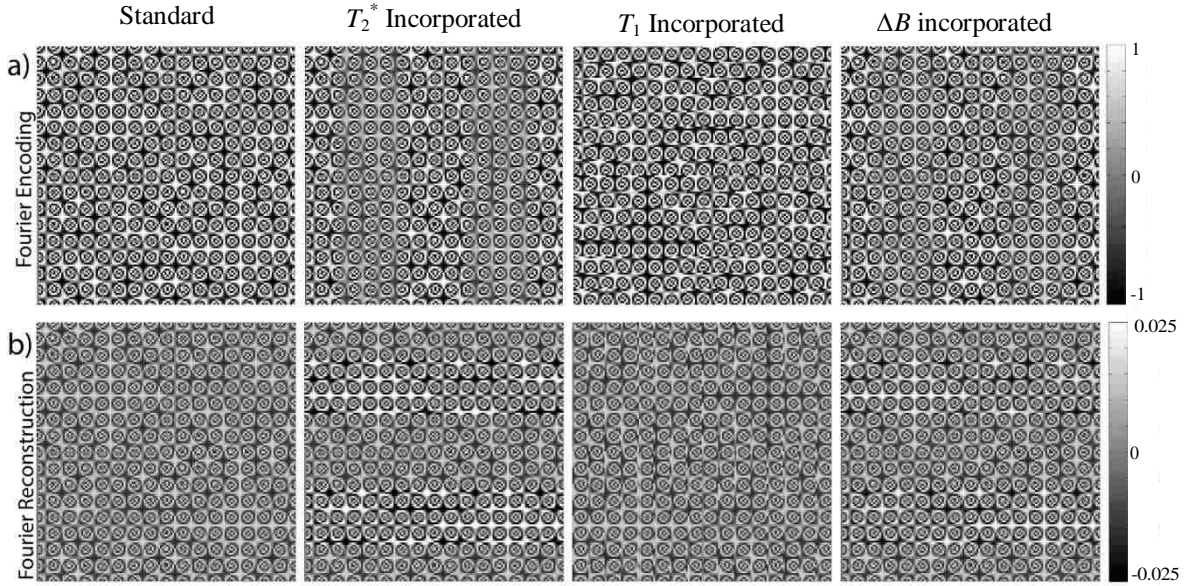
Figure 3.1: a) FE operators: standard FE operator, $\overline{\Omega}$, in the first panel; modified FE operator, $\overline{\Omega}_a$, that separately includes the effects of T_2^*, T_1, or ΔB in the second, third, and fourth panels, respectively. b) FR operators: standard FR operator, Ω, in the first panel; modified FR operator, Ω_a, that separately accounts for the effects of T_2^*, T_1, or ΔB in the second, third and fourth panels, respectively.

3.3   Methods

3.3.1   Theoretical Illustration

To theoretically illustrate the performances of the developed Fourier reconstruction operators, a single-slice of data was generated from a noiseless digital brain phantom. Simulated at 3 T, the proton spin density, M_0, in a 96×96 phantom in Fig. 3.2a was used with model T_2^* and T_1 values that vary from 42 to 2200 ms for T_2^* and from 832 to 4000 ms for T_1, as given in Figs. 3.2b and 3.2c (Atlas, 2008). The ΔB was considered as a left to right gradient from 0 to 2.5×10^{-6} T, as shown in Fig. 3.2d. The timing of the k-space sampling scheme is as in a standard EPI pulse sequence for a 96×96 acquisition matrix, with a bandwidth of 250 kHz, an effective echo spacing of 0.72 ms, an echo time of 50 ms, and a TR of 1 s.
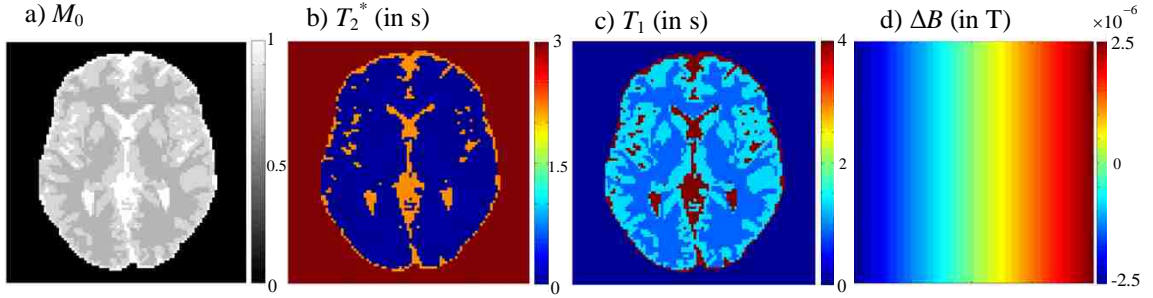
Figure 3.2: Parameters considered in theoretical calculations. (a) Proton spin density, M_0, (b) intra-acquisition decay, T_2^*, (in s), (c) longitudinal relaxation time, T_1, (in s), (d) B-field inhomogeneity, ΔB, (T).

In our calculations for the theoretical illustration, we consider the k-space operators: P_E, P_A, P_S, P_R, Ω_R, Φ_N, Ω_R^{-1}, P_R^{-1} and the FR operator, Ω or Ω_a, depending on our analysis. Thus, the altered mean and the induced covariance matrix by the applied operators can be calculated according to Eq. [3.7] by

$$E(y_{Id}) = \Omega_a P_R^{-1} \Omega_R^{-1} \Phi_N \Omega_R P_R P_S P_A P_E s_{Act}$$

and

$$\text{cov}(y_{Id}) = \left(\Omega_a P_R^{-1} \Omega_R^{-1} \Phi_N \Omega_R P_R P_S P_A P_E \right) \Gamma \left(P_E' P_A' P_S' P_R' \Omega_R' \Phi_N' (\Omega_R^{-1})' (P_R^{-1})' \Omega_a' \right). \qquad [3.18]$$

It should be noted that if $\Gamma = I$, then Eq. [3.18] reduces to

$$\text{cov}(y_{Id}) = \Omega_a \Omega_a', \qquad [3.19]$$

since when each of the operators, except Ω_a, in Eq. [3.18] are multiplied by their transposes, the products yield identity matrices. Therefore, the altered covariance and correlations will only result from the use of the modified FR operator, Ω_a.

In order to examine the effects of FE anomalies on the reconstructed image space data, we use the data that is generated by considering the individual and sequential effects of T_2^*, ΔB, and T_1 in the frequency space. Then, we perform the Fourier reconstruction

with the use of the standard FR operator, Ω, to visually illustrate the alterations that are caused by the FE anomalies if they are not accounted for. Finally, we perform the Fourier reconstruction with the use of the proposed modified FR operator, Ω_a, on the same data set in order to present the performance of Ω_a in accounting for such effects. Presented in Fig. 3.3 are the magnitude, phase, real, and imaginary images that are reconstructed from the data sets generated with the effects of T_2^* in Figs. 3.3a$_1$, and 3.3a$_2$, the effects of ΔB in Figs. 3.3b$_1$, and 3.3b$_2$, the effects of T_1 in Figs. 3.3c$_1$, and 3.3c$_2$, and finally the combined effects of T_2^*, ΔB, and T_1 in Figs. 3.3d$_1$, and 3.3d$_2$. Figs. 3.3a$_1$, 3.3b$_1$, 3.3c$_1$, and 3.3d$_1$ show the images that are reconstructed with the use of the standard FR operator, Ω, whereas Figs. 3.3a$_2$, 3.3b$_2$, 3.3c$_2$, and 3.3d$_2$ illustrate the images that are reconstructed with the use of the modified FR operator, Ω_a. In this chapter, we denote the images as "standard-reconstructed" when the standard FR operator is used for reconstruction while we denote images as "modified-reconstructed" when the FR operator, modified to correct the effects of the respective FE anomaly, is used. When generating data for the results presented in Fig. 3.3, the "true" magnitude of each image is assumed to be the proton spin density as given in Fig. 3.2a, and the phase is originally assumed to be zero throughout the image.

The reconstructed image results that are presented in Figs. 3.3a$_1$ and 3.3a$_2$ are obtained from the frequency space data that is generated by incorporating only the exponential term, $\exp(-t(k_x,k_y)/T_2^*(x,y))$, in such a way that the FE anomaly weighting function, introduced in Eq. [3.13], is assumed to be $W(k_x,k_y,x,y)=\exp(-t(k_x,k_y)/T_2^*(x,y))$. It can be seen in Fig. 3.3a$_1$ that the magnitude and real images show blurring and loss of image intensity effect that T_2^* causes on the edges of the phantom when the considered

T_2^* effect is not corrected. One can also observe that the standard-reconstructed phase

image is not uniform in CSF or in space. The standard-reconstructed imaginary image

shows some artificial imaginary data mostly at the edges of the phantom. The modified-

reconstructed magnitude, phase, real and imaginary images, that are given in Fig. 3.3a$_2$,

appear to be exactly the same as the true magnitude, phase, real and imaginary images.

This outcome illustrates that Ω_a successfully corrects the T_2^* effect on the reconstructed

images.

Fig. 3.3b$_1$ illustrates the standard-reconstructed images whereas Fig. 3.3b$_2$

presents the modified-reconstructed images from the data generated with only B-field

inhomogeneity effects. The frequency space data is generated by considering only the

exponential term, $\exp(-i\gamma\Delta B(x,y)t(k_x,k_y))$, in such a way that the FE anomaly weighting

function in Eq. [3.13] is assumed to be $W(k_x,k_y,x,y)=\exp(-i\gamma\Delta B(x,y)t(k_x,k_y))$. The B-field

inhomogeneity, ΔB, is known to produce image warping and bulk shift in the phase

encoding direction in magnitude and real images, as it can be seen in Fig. 3.3b$_1$. Slight

warping can also be observed in the vertical frequency encoding direction because of the

higher sampling width. Fig. 3.3b$_1$ shows some non-ideal imaginary data that is more

significant at the right portion of the phantom. It can also be observed that the phase

image is not uniform in CSF and in space. As seen in the case that we examine T_2^*

effects, the modified-reconstructed images, that are given in Fig. 3.3b$_1$ have been

successfully corrected through Ω_a.

Presented in Fig. 3.3c$_1$ and Fig. 3.3c$_2$ the standard- and modified-reconstructed

images from the data generated with only T_1 recovery term effects. As explained in

previous cases, the frequency data generation is performed by assuming that the FE

anomaly weighting function in Eq. [3.13] is $W(k_x,k_y,x,y)=(1-\exp(-TR/T_1(x,y)))$. The standard-reconstructed magnitude and real images in Fig. $3.3c_1$ exhibit decreased image intensity throughout the phantom. The expected increase in tissue contrast, when the images are modified- reconstructed by the operator, Ω_a, are not observable in this simulation since the assumed proton spin density already has significant contrast information. Similarly with the previous results, the modified-reconstructed images have successfully been corrected compared to a standard reconstruction as it is apparent in Fig. $3.3c_1$.

Figs. $3.3d_1$ and $3.3d_2$ illustrate the standard- and modified-reconstructed images from frequency space data that is generated with a combination of T_2^*, ΔB, and T_1. The effects of all three terms (blurring, image warping and loss of image intensity) can be observed in the standard-reconstructed images in Fig. $3.3d_1$ while the modified-reconstructed images in Fig. $3.3d_2$ are same as the true maps.

The correction of FE anomalies can be considered as a means of data processing, and thus could potentially induce artificial correlations. Our proposed model allows one not only to account for their effects but also to compute the exact image-space statistics (mean, variance and correlation). As explained in section 3.2.1, the correlation matrix produced by Eq. [3.7] is partitioned into the quadrants that include the correlation between the real components (real/real), between the imaginary components (imaginary/imaginary), and between the real and imaginary components (real/imaginary) of the reconstructed image. Furthermore, the correlations of the magnitude-squared data (square of the magnitude-only data) can be derived from the computed complex-valued correlation matrix and can be considered in the analysis of the correlation structure
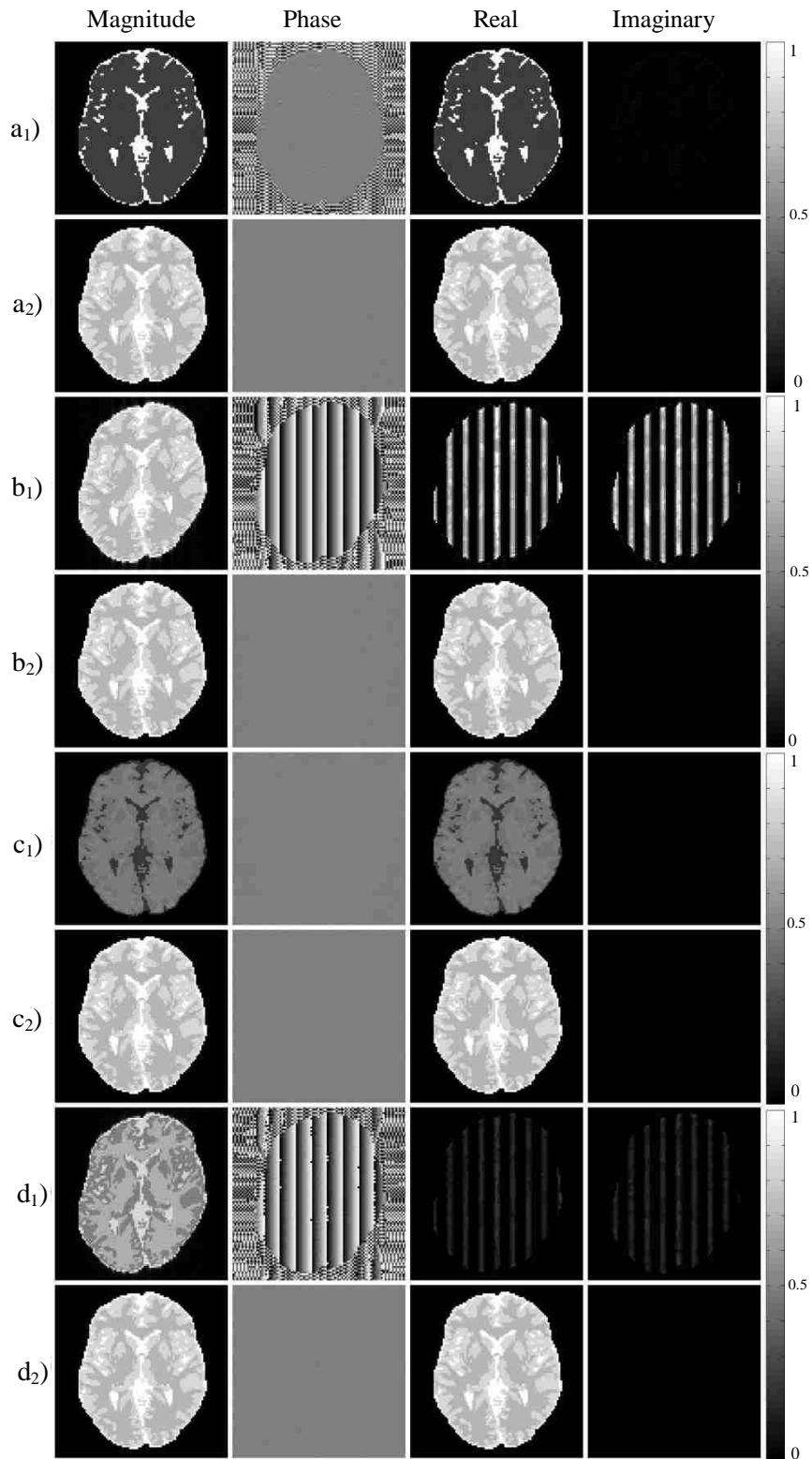
Figure 3.3: Reconstructed magnitude, phase, real, and imaginary images from the frequency space data that is generated with the effects of the following FE anomalies: T_2^* in a_1) and a_2), ΔB in b_1 and b_2, T_1 in c_1 and c_2, and T_2^*, ΔB, and T_1 in d_1 and d_2. The images on the rows of a_1, b_1, c_1, and d_1 are standard-reconstructed whereas the images on the rows of a_2, b_2, c_2, and d_2 are modified-reconstructed from the data.

induced by FE anomaly correction during image registration. In order to present the computed correlation structure, we choose the voxel located in the center of the image as the seed voxel and show the correlation between the measurements of the center voxel, and those from all other voxels. The center voxel's induced magnitude-squared, real/real, imaginary/imaginary, and real/imaginary correlations by the modified FR operator, that are illustrated in Figs. 3.4a and 3.4b, are produced by superimposing the computed correlation structure of the center voxel on a gray-scale anatomical phantom image. Presented in Fig. 3.4a are the induced correlation maps for the center voxel when T_2^* is incorporated. Since we have found that separately accounting for ΔB and T_1 effects yield the same results, the maps presented in Fig. 3.4b represents the correlation structure induced by ΔB or T_1 incorporation. It can be seen that the process of accounting for FE anomalies induces a very small amount of correlation in the maps in Fig. 3.4a and no
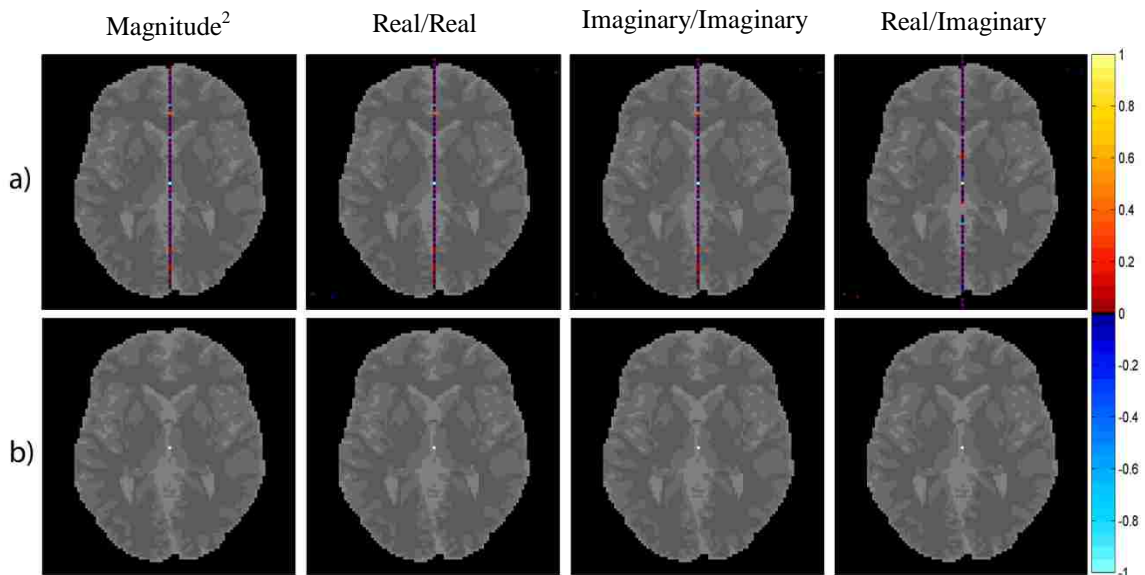
Figure 3.4: Presented on a magnitude brain phantom underlay are theoretical image-space magnitude-squared, real/real, imaginary/imaginary, and real/imaginary correlations about the center voxel induced by the modified Fourier reconstruction operator, Ω_a, that accounts for a) T_2^* effects, b) ΔB or T_1 effects. The correlation maps are computed by the linear model, $corr(y) = D^{-1/2}\Omega_a \Gamma \Omega_a' D^{-1/2}$, with the assumption of an identity initial spatial covariance, $\Gamma = I$, between voxels.

visible correlation in Fig. 3.4b. Since little to no correlation is induced, this FE anomaly correction method is ideal for use in experimental human experiments.

3.3.2   Experimental Illustration

A set of human data from a bilateral finger tapping fMRI block design experiment was acquired for a series of 510 TRs with a 3.0 T General Electric Signa LX magnetic resonance imager to further illustrate the performance of the proposed modified FR operator. The data set was comprised of seven 2.5 mm thick axial slices that are 96×96 in dimension for a 24.0 cm FOV, with the phase encoding direction oriented as posterior to anterior (bottom to top in images). The data set had an effective echo spacing of 0.72 ms, a flip angle of 90°, and an acquisition bandwidth of 250 kHz. A time varying TE array was constructed to utilize the resulting signal change that allows for the estimation of the relaxation parameters, T_1 and T_2^*. The echo time was fixed at 42.7 ms for the first 10 and the last 490 time points, i.e. $1 \leq t \leq 10$ and $21 \leq t \leq 510$. TE values were then equispaced in the interval of [42.7 ms, 52.7 ms] for $11 \leq t \leq 15$ and $16 \leq t \leq 20$.

The application of the proposed linear framework on the acquired data sets is a two-step process, involving the estimation of T_2^*, T_1, and/or ΔB followed by the incorporation of the estimates during the image reconstruction with the use of the modified FR operator. The framework works well when the estimated T_2^*, ΔB and T_1 maps are close to the actual maps. The use of underestimated or overestimated parameter maps in the proposed framework can potentially cause undesired artifacts in the reconstructed images. Since the estimation of T_2^* and ΔB is not the focus of this thesis, we perform the incorporation of only T_1 into the FR process for the experimental illustration of the proposed framework. However, with accurate estimates of T_2^* and

static ΔB maps, the proposed framework can be utilized to incorporate the other Fourier encoding anomalies.

MRI pulse sequences consist of repeated excitation pulses and the magnetization changes in the same way during each repetition. After a number of excitation pulses, the magnetization reaches a steady-state, where the amount of the magnetization at some point in the sequence is the same from one repetition to the next. After reaching the steady-state, the magnetization begins at equilibrium on each repetition. With an assumption of a 90° flip angle, the estimation of T_1 map can be performed from the ratio of the first echo planar imaging time course image and the average steady state image by using a fast T_1 mapping technique introduced in (Bodurka et al., 2007). The steady-state signal for a 90° flip angle is

$$M_{ss} = M_0 \left(1 - e^{-TR/T_1}\right) e^{-TE/T_2^*} ,$$ [3.20]

whereas the signal for the first echo planar imaging volume is

$$M_1 = M_0 e^{-TE/T_2^*} .$$ [3.21]

By using the ratio of M_1 in Eq. [3.21] over M_{ss} in Eq. [3.20], $R = M_1/M_{ss}$, the value of T_1 for one voxel can be calculated by

$$T_1 = \frac{TR}{\ln\left(\frac{R}{R-1}\right)} .$$ [3.22]

For the estimation of T_1 map from the acquired data set that we use in our experimental illustration, the steady state signal, M_{ss}, is computed as the average magnitude images at $6 \leq t \leq 10$ over five time points for each voxel. The estimated T_1 map

that is computed by Eq. [3.22] is shown in Fig. 3.5. In order to reduce the errors in the

final modified-reconstructed images that could result from the T_1 estimation process, the

region outside of the brain is masked out in the presented T_1 map. First, the magnitude

images at $21 \leq t \leq 510$ are averaged over the last 490 points of the time series since the data

was acquired with a time varying TE in the first 20 time points. In order to generate the

binary two-dimensional brain mask that identifies the outside of the brain, the average

magnitude image is used as reference. The voxels whose average magnitude values are

larger than the threshold value, which is set as the 26 % of the maximum value in the

average magnitude image, are given a value of 1 (denoting being in the brain) while the

voxels whose values are smaller than or equal to this threshold are set to 10^{-6} (denoting

being outside the brain) in the binary mask. The estimated T_1 map is then multiplied by

the binary mask image on a voxel-by-voxel basis to mask out the voxels in the region

outside the brain.
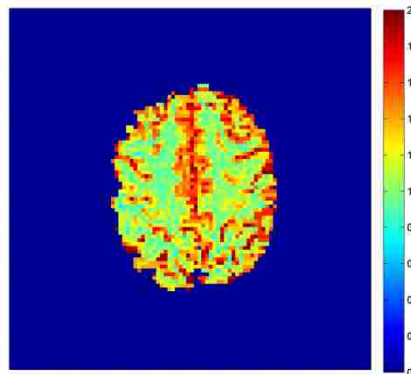
Figure 3.5: Estimated T_1 map (s) from the ratio of the first
time course image and the average steady state image. The
voxel values outside of the brain region is set to 10^{-6} s.

In order to illustrate the benefits of the incorporation of T_1 into the FR process, we

show the magnitude, phase, real and imaginary images that are acquired at the 21st time

point, and reconstructed both with the standard FR operator, Ω, and the modified FR operator, Ω_a. Fig. 3.6a shows the standard-reconstructed magnitude, phase, real and imaginary images whereas Fig. 3.6b shows the modified-reconstructed images. It can be observed from Fig. 3.6 that the incorporation of T_1 leads to an increase in image intensity as well as significantly improved tissue contrast in the magnitude images. Such correction does not alter the phase image while increasing the intensity of the magnitude, real, and imaginary images.
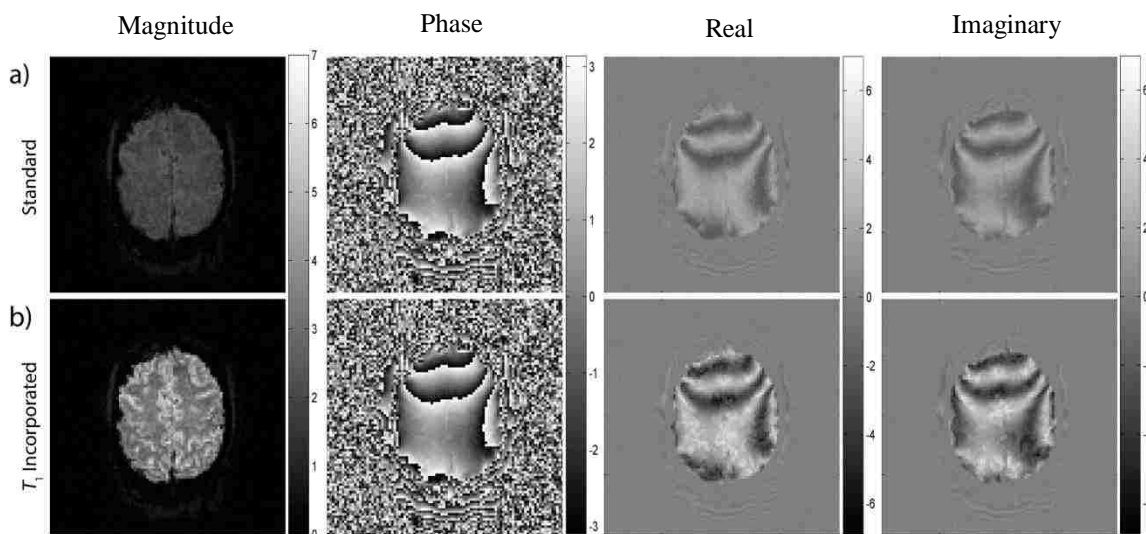
Figure 3.6: Reconstructed magnitude, phase, real, and imaginary images at time point $n=21$. a) Images that are reconstructed with the standard FR operator, Ω, b) Images that are reconstructed with the modified FR operator, Ω_a.

In order to analyze the possible effects of such correction on the functional activations computed from T_1 incorporated reconstructed images, we show the activation statistics of both standard-reconstructed and modified-reconstructed images in Figs. 3.7a, 3.7c and 3.7b, 3.7d, respectively. Figs. 3.7a and 3.7b show the activation t-statistics computed by using the likelihood ratio tests from the MO Model (Bandettini et al., 1993). Illustrated in Figs. 3.7c and 3.7d are the activation Z-statistics computed by using the CV

Model (Rowe and Logan, 2004; Rowe, 2005a,b). The activation maps shown in Fig. 3.7 were thresholded at a 5% per comparison error rate (Logan and Rowe, 2004) and presented with a color bar that ranges between -6.5 and 6.5. It can be observed that the activation statistics that are computed from the standard-reconstructed and the modified-reconstructed image space measurements are identical for both the CV and MO Models. It can be concluded that T_1 incorporation into the Fourier image reconstruction process preserves the functional activations. This result is expected since the estimated T_1 map that is incorporated during the image reconstruction is constant over the time series and therefore the activation information is preserved with the proposed framework.

| a) Ω-reconstr. (MO) | b) Ω_a-recons. (MO) | c) Ω-recons. (CV) | d) Ω_a-recons. (CV) |
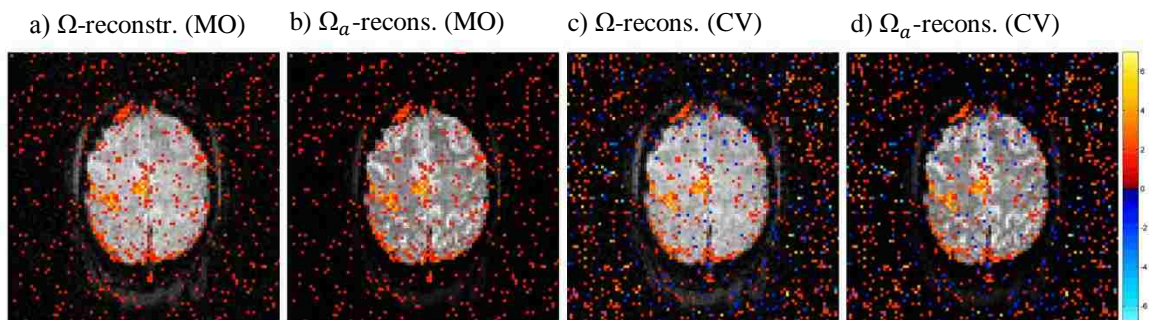
Figure 3.7: Activation statistics that are computed from a) standard-reconstructed images with the use of the MO Model, b) modified-reconstructed with the use of the MO Model, c) standard-reconstructed images with the use of the CV Model, d) modified-reconstructed with the use of the CV Model. The activation maps are thresholded at a 5% per comparison error rate.

3.4   Discussion

The model developed in this chapter expands upon the AMMUST-k framework that examines the statistical implications of frequency space and image space processing operations (Nencka et al., 2009). We further expand this framework to account for the effects of relaxation parameters, T_2^* and T_1, and magnetic field inhomogeneities, ΔB, that alters the observed MR signal in the process of Fourier encoding. We develop a modified

FR operator that accounts for such effects in image space by first generating the modified FE operator that considers the terms of these anomalies as they appear in the signal equation, and then inverting. Although the correction of T_2^* and ΔB effects prior to the final analysis of fMRI data have been the focus of research in previous studies, the T_1 recovery term has been ignored with the assumption of long repetition time, which is not always met, especially when performing fast repetitive image excitations. Furthermore, the T_1 estimates have the potential to detect tissue characteristics of the acquired MRI data. In this chapter, we present theoretical results for accounting for the effects of T_2^*, ΔB, and T_1 during the Fourier reconstruction process, and focus on T_1 incorporation in acquired human subject echo planar data. The experimental results presented in this chapter have shown that the images reconstructed through the use of the reconstruction operator adjusted for estimated static T_1 appear to be brighter and have increased tissue contrast. This increased gray/white matter contrast can improve the precision of image reconstruction, motion correction, image registration, and tissue segmentation over a time series. Furthermore, our experimental results show that such correction does not alter the activation results. Even though we incorporate only T_1 into the reconstruction process in our experimental analysis, the model can be utilized to account for T_2^* and ΔB effects once their estimated maps are obtained.

The proposed framework makes it possible to precisely quantify any potential induced correlations by the process of accounting for FE anomalies. It has been shown that the FR operator that is modified by the incorporation of ΔB or T_1 does not induce any image space correlations whereas the one that accounts for T_2^* blurring effect induces negligible correlation in the phase encoding direction. The Fourier anomaly correction

method introduced in this chapter can be used on a regular basis in every fMRI and

fcMRI experiment.

Chapter 4:   Quantification of the Statistical Effects of Spatial and Temporal Processing of fcMRI and fMRI Data

In this chapter, the linear model introduced in Chapter 3 is further expanded to a more general framework that represents the spatiotemporal processing and reconstruction operations as linear operators. The linear representation provides precise quantification of the correlations induced or modified by such processing rather than performing lengthy Monte Carlo simulations. A framework of this kind allows one to appropriately model the statistical properties of the processed data, optimize the data processing pipeline, characterize excessive processing, and ultimately draw more accurate functional connectivity conclusions.

4.1   Introduction

Spatiotemporal processing is a common practice in fMRI and fcMRI studies as a way to "improve" the resulting images. Such processing makes the image data more "appealing" by alleviating it of "noise". However, fMRI/fcMRI data processing could unknowingly lead to misguided conclusions as the signal (mean) and noise (variance and correlation) properties of the data are altered with the application of these processes. In recent studies, it has been shown that spatial processing operations, such as spatial filtering in both the spatial frequency space and image space domains (Nencka et al., 2009; Karaman et al., 2013b; Karaman et al., 2014b), induce artificial correlations. Moreover, parallel MRI models, such as SENSitivity Encoding (SENSE) (Pruessmann et al., 1999) and Generalized Autocalibrating Partially Parallel Acquisition (GRAPPA) (Griswold et al., 2005), have been shown to induce artificial correlations between

previously aliased voxels in the reconstructed images (Bruce et al., 2011; Bruce et al., 2012; Bruce and Rowe 2013; Bruce and Rowe, 2014). Functional MRI and fcMRI studies typically employ both spatial and temporal filtering, together with additional signal regression operations (Glover et al., 2000; Hahn and Rowe, 2012). While these spatial and temporal processing operations could induce artificial correlations in the acquired data, the traditional fMRI and fcMRI models assume independence between voxels, and therefore do not account for the spatial correlation between voxels or temporal correlation within each voxel's time series. As these correlations are of no biological origin, they can result in increased Type I/Type II errors in both fMRI and fcMRI. Even though the structure of the induced correlations can be estimated through time consuming simulations, there is an apparent need for the development of tools that can precisely quantify the implications of spatial and temporal processing operations and means of accounting for these implications in the final analysis. If the effects that such operations have on the statistical properties of the acquired data are unaccounted for, neuroscientists could draw inferences from the processed data that are inconsistent with those of the original data.

Many studies have aimed to rid the data of "noise" through both spatial and temporal processing. However, little attention is ever paid to the degree to which processing operations change the true statistical properties of the acquired data. Previous studies have considered means of evaluating preprocessing by either using time consuming Monte Carlo simulations (Della-Maggiore et al., 2002) or empirically optimizing the processing procedures (LaConte et al., 2003; Shaw et al., 2003). Such work aims to determine the best results through the evaluation of the effect of

preprocessing on the computed time series statistics, while the true statistical properties of the data are not typically included into the given fMRI and fcMRI models. Bowman (2005) presented a spatiotemporal model that partitions voxels into functionally related networks and captures correlations between voxels through a simultaneous spatial autoregression. Other promising work has shown that accounting for background spatial correlation inherent in neuroimaging data, that is caused by non-neurophysiologic associations and image processing, can improve functional connectivity measurements. (Patel et al., 2006). A study by Deshpande et al. (2009) introduced the measure of integrated local correlation for assessing local coherence and corrected the inherent correlation in the fMRI data due to the image acquisition and reconstruction processes. Derado et al. (2010) proposed a two-stage model that accounts for both spatial and temporal correlations in the fMRI data. However, these approaches either do not account for temporal correlations or do not provide a theoretical estimation of spatiotemporal correlations of the voxel measurements to be accounted for in the fMRI and fcMRI models.

Previous studies have incrementally developed the necessary tools to evaluate and incorporate the statistical impact of spatial and temporal processing operators into the final analysis of the fcMRI and fMRI data. A real-valued isomorphism of the complex-valued inverse Fourier transformation matrix operator was described by Rowe et al. (2007) in order to relate the signal and noise characteristics of k-space measurements and reconstructed voxel measurements. As explained in Chapter 3, representing Fourier reconstruction as a single matrix operator formed the basis for another study by Nencka et al. (2009) in which the AMMUST-k framework was developed to represent various

spatial processing operations performed on the acquired spatial frequencies in terms of real-valued linear isomorphisms. The AMMUST-k framework was further expanded to incorporate parallel MR reconstruction models, SENSE and GRAPPA, by representing each model as a series of real-valued matrix operators (Bruce et al., 2011; Bruce et al., 2012; Bruce and Rowe, 2013; Bruce and Rowe, 2014). Representing the reconstruction and spatial processing in this way makes it possible to precisely compute the covariance (and ultimately correlation) induced by such operations into the image-space data.

In this chapter, "A Mathematical Model for Understanding the STatistical effects of time series preprocessing" (AMMUST-t) is developed by advancing the AMMUST-k framework to include temporal processing of the data together with spatial processing and parallel MRI reconstruction operations. With a framework of this kind, one can precisely quantify the degree to which the mean and covariance between both voxels and time points are modified by each processing operation individually or by all processes collectively, without the need for lengthy simulations that can only approximate these changes. Such a framework can be used by neuroscientists to assess their processing pipelines by characterizing excessive processing, and ultimately aid in producing more accurate functional connectivity statistics. In this chapter, we first develop time series operators for common processing operations such as image registration (Jenkinson et al., 2002), dynamic magnetic field correction (Hahn et al., 2009), slice timing correction (Huettel et al., 2004), and temporal filtering (Huettel et al., 2004), and illustrate the effects of these operators with a low dimensional example. We then demonstrate the effects of commonly used operations such as spatial smoothing, temporal filtering, and a

SENSE image reconstruction with higher dimension theoretical data as well as on experimental phantom and resting state human subject data.

4.2   Theory

4.2.1   AMMUST-*t* Framework

A real-valued isomorphism for the complex-valued Fourier reconstruction, that was presented in section 3.1.2, allowed the image reconstruction to be performed by

$$y = \Omega s,$$ [4.1]

where $s=(s_R', s_I')'$ is a $2p \times 1$ column vector of the frequency space measurements for an $u \times v$ image of $p = uv$ voxels. In this representation, $s_R=(s_{R1},\ldots,s_{Rp})'$ and $s_I=(s_{I1},\ldots,s_{Ip})'$ are $p \times 1$ real-valued vectors representing the real and imaginary parts of the observed frequency space measurements, respectively. This formalism produces a vector, y, with all real reconstructed voxel values stacked by row on top of all imaginary reconstructed voxel values. As explained in detail in Chapter 3, this formalism in Eq. [4.1] can be generalized to

$$y = Os,$$ [4.2]

where the operator O signifies an arbitrary series of linear processing operations (Nencka et al., 2009) expressed in matrix form.

In order to improve the temporal resolution, spatial frequencies of fMRI and fcMRI data is often sub-sampled with multiple coils by an acceleration factor of a, where only every a^{th} line of the frequency space is acquired. As skipping k-space lines results in aliasing in images, parallel MRI models are used to synthesize the missing k-space lines

and form full FOV data. SENSE model performs complex-valued least squares to unfold the aliased coil images (Pruessmann et al., 1999). In recent studies, SENSE model was represented by the multiplication of a series of matrices (Bruce et al., 2011; Bruce et al., 2012) to perform the reconstruction of an image at an individual time point by using a linear operator that allows one to precisely quantify the artificial correlations induced between the previously aliased voxels. The operator, O, in Eq. [4.2] was adopted to include a linear operator that reconstructs all aliased coil images at once with the assumption that the frequency space vector, s, includes the spatial frequencies from each N_C coils.

In the AMMUST-t framework, the model in Eq. [4.2] is extended to combine temporal processing operations with the previously developed spatial processing and reconstruction operations. In such a framework, the vector of the observed k-space observation can be represented as a concatenation of n k-space signal vectors, with each of these vectors representing one $2p \times 1$ time point image vector. The time series frequency measurements can therefore be represented by a $2pn \times 1$ column vector, $s_T = (s_{1R}', s_{1I}', \ldots, s_{nR}', s_{nI}')'$ where s_{tR} and s_{tI} are the real and imaginary frequency space column vectors at time point t. The reconstructed and processed time series, y_T, can then be obtained from the acquired signal vector, s_T, by

$$y_T = O_T s_T .$$
[4.3]

The operator matrix, O_T, is formed through the multiplication of a k-space processing operator, K, a reconstruction operator, R, an image-space processing operator, I, and finally a temporal processing operator, T, as

$$O_T = TIRK .$$
[4.4]

4.2.2 Time Series Operators

As most of the existing spatial and temporal processes are linear in nature, or their application to the data can often be represented in a linear way, many commonly used processing operations can be integrated into the O_T operator of the AMMUST-t framework. In this section, we demonstrate the construction of matrix operators for a collection of common processing operations that might be considered in this framework. These operators include the generalization of individual time point k-space, image space, and reconstruction operators, the performance of temporally dynamic B-field corrections, the shifting and rotating of images for registration, temporal filtering, and slice timing correction.

Generalized k-space, Image-space and SENSE Reconstruction Operators

In the AMMUST-k framework, k-space and image space processing operations, O_K and O_I, are temporally unvarying, and equivalently applied to each image in a time series. These operations include the incorporation of intra-acquisition decay and static B-field, the performance of zero filling, apodization, smoothing and partial Fourier reconstruction. In AMMUST-t, applying such operators to the newly parametrized time series data requires an operator of higher dimensionality. Consider that the same image processing steps are performed on all time points of an acquired k-space time series. The time series k-space and image space processing operators, K and I, can then be formed with a Kronecker product between the previously described individual time point operators and an identity matrix with dimension matching the number of time series points, I_n, as $K = I_n \otimes O_K$, and $I = I_n \otimes O_I$, respectively. The resulting operators are

therefore block diagonal where each block corresponds to an instance of the processing

operators. As previously described, a generalization of the SENSE reconstruction

operator can be performed in a similar fashion to the k-space and image space processing

operations by $R = I_n \otimes O_R$, where O_R can be considered as the SENSE parallel image

reconstruction operator for an individual time point.

Dynamic *B*-field Correction

In echo planar imaging, magnetic field inhomogeneities can result in severe

artifacts such as image warping and signal loss. Since the characteristics of the B-field

inhomogeneity are affected by respiration and motion, in a time-dependent manner,

dynamic B-field correction may need to be performed before the analysis of the fMRI and

fcMRI data. Such correction can be included into the AMMUST-t framework by altering

the FR operator in Eq. [4.1]. The magnetic field inhomogeneity to be corrected can be

estimated through relative field measurements (Hahn et al., 2009) or intra-acquisition

measurements (Roopchansingh et al., 2003). With an estimated offset, ΔB, for each k-

space vector, the FR operator can then be multiplied by $\exp(-i\gamma\Delta B(x,\ y)t(k_x,k_y))$, where

$t(k_x,k_y)$ represents the time at which the k-space point corresponding to the row of the

Fourier encoding matrix was acquired. As such, the individual blocks along the diagonal

of the time series reconstruction operator, R, can be adjusted to correct the B-field

inhomogeneity effects at the corresponding time point.

Image Registration

Head motion can be a severe problem for the statistical analysis of the fMRI data

since the time course of one single voxel would represent a signal derived from different

parts of the brain when the subject moves. Image registration is used for motion correction in fMRI and performed by shifting each image according to independently determined motion parameters. In-plane motion correction can be performed by integrating the registration into the time-series reconstruction operator, R, as in the case of dynamic B-field correction. As both image-space translation and in-plane rotation can be considered as shifts on x and y axes, multiplying the k-space data with an appropriate phase before the Fourier reconstruction yields a correctional shift in image-space after reconstruction as a result of the Fourier shift theorem. For a voxel that is originally located at (x,y) in image space, the horizontal and vertical displacements resulting from motion can be calculated by $\Delta x = \delta_x + x(\cos\psi - 1) - y\sin\psi$, and $\Delta y = \delta_y + y(\cos\psi - 1) - x\sin\psi$, respectively, where δ_x and δ_y represent horizontal and vertical image space translation and ψ represents in-plane rotation. For a single image with the aforementioned motion parameters, the row of the inverse Fourier transformation operator that represents the image-space point (x,y) must have each element multiplied by the exponential term, $\exp(-i2\pi(\Delta_x k_x / p_x + \Delta_y y_x / p_y))$, where k_x and k_y are integers representing the k-space indices of the column of the inverse Fourier transformation operator, and p_x and p_y are the number of k-space points in the x and y directions, respectively. The complex-valued inverse Fourier transformation operators for each time point can be formed by modifying the real valued isomorphism in Eq. [4.1] and then appropriately positioned along the diagonal of the time series reconstruction operator, R. The motion parameters of image-space translation, (δ_x, δ_y), and in-plane rotation, ψ, can be determined through available software (Jenkinson et al., 2002; Cox, 1996), or through external means, such as a tracking device

that measures head motion (Tremblay et al., 2005). A three-dimensional registration operator can be also constructed by utilizing a three-dimensional Fourier transforms.

Temporal Filtering

The process of temporal filtering can be performed through an application of the Fourier shift theorem. The temporal filtering process is mathematically identical to the line shifting process used to correct Nyquist ghosts in EPI. First, the vector of reconstructed images can be reordered to a vector of reconstructed voxel time series through a permutation matrix, P_T. Then, each time series can be Fourier transformed into the temporal frequency domain by a block diagonal matrix, Ω_T, where each block is a real-valued isomorphism of a one-dimensional time series Fourier transform matrix. Each transformed time series can then be multiplied by a diagonal matrix, Φ_T, with diagonal elements comprised of frequency space weighting for temporal filtering. The temporally filtered image time series vector then can be obtained through the inverse Fourier transformation and inverse permutation, $T = P_T^{-1} \Omega_T^{-1} \Phi_T \, \Omega_T P_T$.

Slice Timing Correction

In fMRI, the MR scanner acquires different slices of the brain sequentially throughout the repetition time period, resulting in a temporal offset between slices. As knowledge of the exact acquisition timing is essential for fMRI, differential slice acquisition times should be accounted for, especially for acquisitions with long TRs. Slice timing correction is performed in image-space after k-space processing, reconstruction and registration in order to align all slices with the same reference time point. The slice timing process can be performed similar to the process of temporal filtering. After transforming the vector of the reconstructed images into a temporal

frequency vector, multiplication with a matrix that consists of sines and cosines to create the additional phase shift for the time series is performed. The vectors of temporal frequencies can then be inverse Fourier transformed to obtain temporally shifted time series, and then the inverse of the original permutation matrix is performed to obtain temporally shifted images. It has been shown that the shifting of k-space lines does not induce correlations in the acquired data if the acquired k-space data is assumed to be uncorrelated (Nencka et al., 2009).

4.2.3 Functional Correlations

In fcMRI, the null hypothesis assumes no correlation between voxels, and thus any statistically significant correlation observed in the data denotes a functional connection between voxels. With the amount of processing performed in fcMRI studies through operations such as spatial filtering, temporal filtering, nuisance signal regression, global signal regression, the statistical properties of the processed voxels are far removed from those of the acquired data. When time series processing operations, O_T, are applied to a data vector in Eq. [4.3], $s_T = s_{T_0} + \eta_{s_T}$, which is comprised of a mean vector of complex-valued spatial frequencies, in a real-valued form, s_{T_0}, added to a noise vector, η_{s_T}, with a mean of zero and a covariance of Γ_T, then the time series image vector, $y_T = O_T s_T$ has a mean and covariance of

$$E[y_T] = O_T s_{T_0} \qquad\qquad [4.5]$$

and

$$\Sigma = \text{cov}(y_T) = O_T \Gamma_T O_T{}'. \tag{4.6}$$

As the vector of images, y_T, is comprised of a stack of n image space vectors, each length $2p \times 1$, the spatiotemporal covariance matrix, Σ, in Eq. [4.6] is of dimension $2pn \times 2pn$. The $2p \times 2p$ blocks along the diagonal of Σ contain the spatial covariance matrices for the individual images, and are partitioned into quadrants that contain the real by real, real by imaginary, and imaginary by imaginary covariances. The spatiotemporal correlation matrix is obtained from the covariance matrix by

$$\Sigma_R = \text{corr}(y_T) = D_T{}^{-1/2} O_T \Gamma_T O_T{}' D_T{}^{-1/2}, \tag{4.7}$$

where D_T is a diagonal matrix of the variances drawn from the diagonal of the covariance matrix, Σ. To deduce the covariance induced solely by the operation O_T, one merely assumes an inherent identity covariance in the data, $\Gamma_T = I$.

It is a common practice in fcMRI to use the $2p \times 2p$ spatial covariance matrix, Σ_ρ, which is estimated from time series observations. It is shown in Appendix C that the average of the diagonal blocks of the large spatiotemporal covariance matrix, Σ, is the expected value of the spatial covariance matrix, Σ_ρ. For functional connectivity analysis, the spatial covariance matrix, Σ_ρ, is converted into a spatial correlation matrix, $\Sigma_{R\rho}$, similar to Eq. [4.7].

Another practice in fcMRI is to analyze the temporal covariance matrix, Σ_v, which represents a single voxel's time series covariance matrix. Although the large covariance matrix Σ contains the components necessary to compute Σ_v, Σ must be permuted by a matrix, P_T, which reorders the reconstructed data from a vector of n vectors of p

observations stacked above each other to the reconstructed time series vector of p vectors of n observations stacked above each other. The reordered covariance matrix is thus

$$\Sigma_T = P_T \Sigma P_T' = \begin{bmatrix} \Sigma_{T_{11}} & \cdots & \Sigma_{T_{1p}} \\ \vdots & & \vdots \\ \Sigma_{T_{p1}} & \cdots & \Sigma_{T_{pp}} \end{bmatrix}, \qquad [4.8]$$

where each $\Sigma_{T_{ij}}$ block is a $2n \times 2n$ temporal covariance matrix between spatial elements i and j. The diagonal blocks of Σ_T are the temporal covariance matrices for the p individual voxels. The vth voxel covariance matrix, Σ_v, is of the form

$$\Sigma_v = \begin{pmatrix} \Sigma_{vRR} & \Sigma_{vRI} \\ \Sigma_{vRI}' & \Sigma_{vII} \end{pmatrix}. \qquad [4.9]$$

4.3   Implementation of the AMMUST-*t* Framework

The matrix representations of spatial and temporal processing operations can be very computationally intensive, requiring large amounts of memory. The final single operator for an acquisition matrix of 96×96, single slice, and 490 repetitions would be of dimension 9,031,680×9,031,680. With the assumption that the operators are in double precision, the memory size of an individual time series operator is approximately 81.5 TB. Moreover, the two matrices to be multiplied and the resulting matrix are required to be held in the memory during matrix multiplication.

As it has been explained in section 4.2.1, the k-space processing operator, K, reconstruction operator, R, and image-space operator, I, are created by generalizing the individual processing operators, O_K, O_R, and O_I, respectively with the use of Kronecker product operator. As such, the final time series operators K, R, and I are block diagonal

sparse matrices of size $2pn \times 2pn$ with n diagonal blocks of size $2p \times 2p$. The block diagonal structure of the operators along with the sparse representation drops the memory size of the time series operator (for a 96×96 acquisition array in 490 repetitions) to 2.1 TB. Moreover, the temporal processing operator, T, consists of multiplication of matrix operators and is represented as $T = P_T^{-1} \Omega_T^{-1} \Phi_T \Omega_T P_T$. As a result of using permutation matrix in this process, the time series operator T is not of block diagonal form, but still can be stored as a sparse matrix.

As the problem of requiring large amounts of memory is faced in all aspects of the framework, we develop an efficient implementation with the use of matrix partitioning, sparse matrix multiplication techniques, and utilization of the block diagonal form of the matrices in matrix multiplication when possible. For the implementation of the proposed spatial and temporal processing framework, we deploy an algorithm that uses the following:

- Sparse representation of the operators.

- Utilizing the block diagonal structure of the matrices in performing matrix multiplications, when possible.

- Two stage matrix partitioning:
    o Performing matrix multiplications in four partitions, i.e. using T_{11}, T_{12}, T_{21}, and T_{22} for the time series operator, T.
    o Using $n/2$ square partitions that are located on the block diagonals of R_{11}, R_{22}, K_{11}, K_{22}, I_{11}, and I_{22} for matrix multiplication, i.e. using $R_{11,dd}$, which is the square matrix on the dth block diagonal of R_{11}. The matrix $R_{11,dd}$ corresponds to the reconstruction operator that will be applied to the k-space vector

acquired at image time point d, whereas $R_{22,dd}$ corresponds to the reconstruction operator that will be applied to the k-space vector acquired at image time point $n/2+d$.

- o Using $n/2$ row wise partitions of each quadrant of the time series operator, T, for matrix multiplication, i.e. using $T_{ij,d,}$ which is the dth row-wise partition of ij^{th} quadrant of T, where $i,j = 1,2$ and $d = 1,2,\ldots,n/2$.

- Storing the resulting partitions of matrix multiplications as square partitions.

- Reducing the number of the arrays kept in the memory when performing a multiplication.

- Reducing the number of the times that the arrays are loaded and saved.

In the case that an identity k-space covariance structure is assumed, $\Gamma_T = I$, the covariance matrix of the time series images, given in Eq. [4.6], is calculated by $\Sigma = O_T O_T{}'$. Rather than first creating the final time series operator, O_T, and multiplying it with its transpose, the covariance matrix, Σ, can be computed directly by utilizing the block diagonal structure of I, R and K operators as follows:

$$\Sigma = T(IRK)(IRK)'T' = T(MM')T' = TLT',$$
[4.10]

where L has the multiplication of individual k-space processing, reconstruction, and image space operators, O_K, O_R, and O_I, on its block diagonals.

In the case that a non-identity k-space covariance structure is assumed, $\Gamma_T \neq I$, the covariance matrix of the time series images, given in Eq. [4.5] is calculated by $\Sigma = O_T \Gamma_T O_T{}'$, with an estimated Γ_T matrix. With the assumption of only spatially

correlated data, the implementation of the framework can be performed similar to the case of identity k-space covariance matrix. In this case, Eq. [4.10] can be written as

$$\Sigma = T(IRK)\Gamma_T(IRK)'T' = T(M\Gamma_T M')T' = TUT' . \qquad [4.11]$$

As Γ_T is a block diagonal matrix, this case requires only one more block diagonal matrix multiplication to create U from the individual reconstruction, k-space, and image space operators, O_R, O_K, O_I, and the block diagonals of Γ_T, that are of size $2p\times 2p$. The computation of the reordered covariance matrix, $\Sigma_T = P_T \Sigma P_T'$, and the correlation matrix, $\Sigma_R = corr(y_T) = D_T^{-1/2}\Sigma D_T^{-1/2}$, can also be performed with this proposed implementation approach.

4.4 Theoretical Illustration

To illustrate the linear representations of the aforementioned time series processing operations, and to quantify the correlations induced by such operations, a time series of 490 images was generated with a single 96×96 slice of true noiseless brain phantom with a maximum magnitude of 10. Within this illustration, the operations that we chose were spatial smoothing, SENSE reconstruction, and temporal filtering. To integrate the SENSE reconstruction into the framework, k-space data was sub-sampled by an acceleration factor of $a=3$ with $N_C=4$ coils (Bruce et al., 2011). After reconstruction, spatial filtering was performed with a Gaussian smoothing kernel with an image-space full width at half maximum (fwhm) of three pixels. A temporal filtering operator was generated to band pass filter the voxel time series to observe frequencies below 0.1 Hz as it is a common practice in fcMRI studies to eliminate BOLD signal changes correlated with physiological effects (Biswal et al., 1995).

To closely illustrate the time series processing operators, a 6×6 ROI was selected within the brain phantom in the first 8 time points of the generated data. As the data was sub-sampled by the acceleration factor of $a=3$ with $N_C=4$ coils, the SENSE reconstruction operator is of dimension 576×768, and the spatial smoothing and temporal operators are of dimension 576×576. Figs. 4.1a-4.1c show the time series operators for SENSE reconstruction, spatial smoothing, and temporal filtering that were used to compute the operator induced spatiotemporal correlation matrices, assuming an underlying k-space identity covariance structure, $\Gamma_T = I$.

a) Reconstruction operator, R b) Smoothing operator, I c) Temporal filtering operator, T
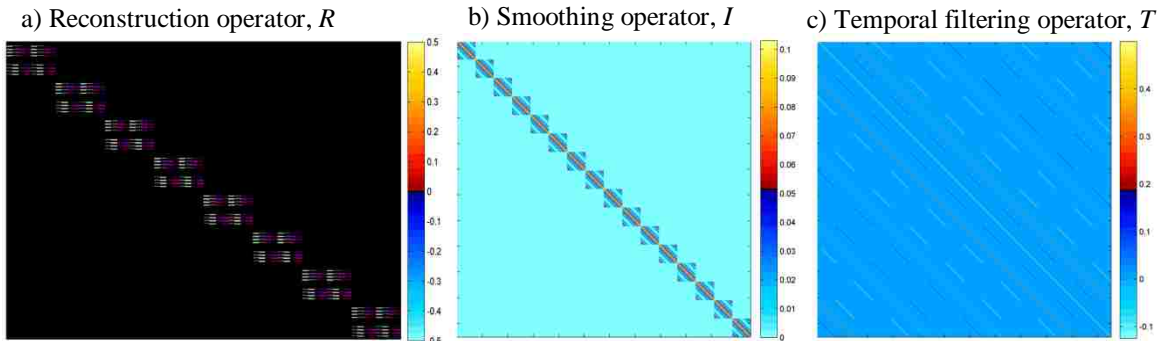
Figure 4.1: Time series operators for an acquisition of $N = 8$ repetitions of a 6×6 ROI. a) SENSE reconstruction operator from $N_C=4$ coils with an acceleration factor of $a=3$, b) smoothing operator, I, c) temporal filtering operator, $T=P_T^{-1}\Omega_T^{-1}\Phi_T\Omega_T P_T$.

Illustrated in Figs. 4.2a-4.2c are the theoretical correlation matrices that are induced by the SENSE reconstruction, spatial smoothing, and temporal filtering, respectively. The first, second, and third columns of Fig. 4.2 illustrate the correlation matrices calculated from the large covariance matrix, Σ, spatial covariance matrix, Σ_ρ, and temporal covariance matrix, Σ_v, about the center voxel, respectively. Figs. 4.2d$_1$-4.2d$_3$ show the overall correlation matrices when SENSE reconstruction, spatial smoothing, and temporal filtering are considered together. Figs. 4.2a$_2$ and 4.2b$_2$ show that the SENSE reconstruction induces spatial correlations between voxels that are previously aliased

with each other, while smoothing induces correlations in the neighborhood of the voxels, as expected. Temporal filtering does not alter spatial correlations, as shown in Fig. $4.2c_2$, as the process is purely temporal. Temporal correlations are only altered by temporal filtering, as seen in Figs. $4.2a_3$, $4.2b_3$ and $4.2c_3$. The correlation maps in the case that the processes are considered together may appear to be dominated by individual processes, as seen in Fig. $4.2d_1$-$4.2d_3$. However, the correlation map is not a simple superimposition of the individual processes, which highlights the advantage of the proposed AMMUST-t framework that provides an exact quantification of the final correlation structure.

In order to observe the effects of the processing operations on the spatiotemporal correlation structure of the data, we computed both theoretical and Monte Carlo simulated spatial and temporal correlations between the real components (real/real), between the imaginary components (imaginary/imaginary), and between the real and imaginary (real/imaginary) components of the reconstructed voxel values. For Monte Carlo simulation, a single 96×96 slice was generated for a time series of 490 images by $y_t=m_t+\varepsilon_t$, where m_t is a $2N_C×p$ matrix whose first N_C rows are the real noiseless images and the second N_C rows are the imaginary noiseless images. The noise matrix $\varepsilon_t=z_t$ was assumed to be a $2N_C×p$ random matrix drawn from the standard normal distribution when the initial identity voxel covariance was assumed. When the initial voxel covariance was assumed to be non-identity, ε_t was generated by $\varepsilon_t=z_tQ_\Gamma$ where Q_Γ is the second unitary matrix in the singular value decomposition of the non-identity voxel covariance structure $\Gamma_T = P_\Gamma\Sigma_\Gamma Q_\Gamma{}'$. The covariance matrix, Σ_Γ, can be constructed according to the intrinsic spatial covariance between voxels. The theoretical operator induced correlations were

computed by Eq. [4.7] whereas Monte Carlo simulated correlations were estimated from 100 simulations.
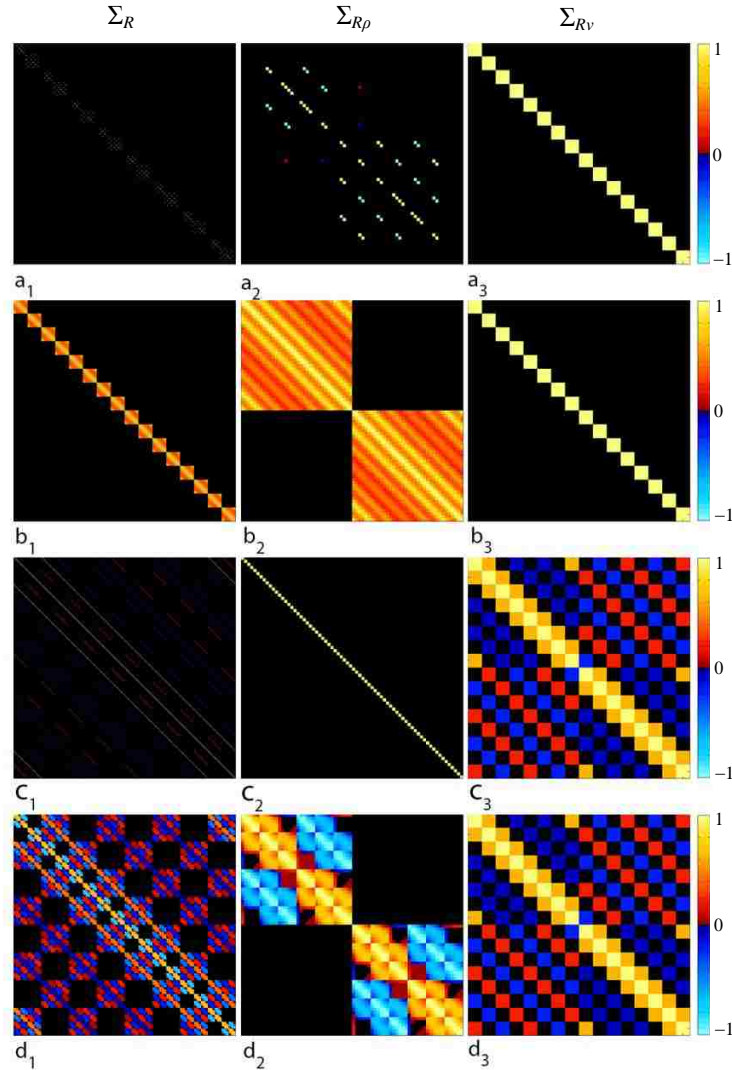
Figure 4.2: Theoretical spatiotemporal correlation matrices that are induced by the consideration of a) SENSE reconstruction from N_C=4 coils with a=3, b) spatial smoothing, c) temporal filtering, d) SENSE reconstruction, spatial smoothing, and temporal filtering. First column: large correlation matrix, Σ_R. Second column: spatial correlation matrix, $\Sigma_{R\rho}$. Third column: center voxel's temporal correlation matrix, Σ_{Rv}.

Correlations in the theoretical and Monte Carlo simulated illustrations are analyzed for the spatially smoothed SENSE reconstructed images with and without the application of band pass filtering under the assumption of identity or non-identity intrinsic k-space covariance structure. In the case of the non-identity spatial covariance,

the intrinsic *k*-space covariance structure is designed in such a way that three ROIs are assumed to be inherently correlated with each other. These regions are selected in the areas that are similar to the motor cortices and supplementary motor area, as presented in Figs. 4.3b$_5$ and 4.3d$_5$. Our Monte Carlo simulation results have shown that the spatial and temporal correlation maps, with and without an inherent correlation assumption, are visually the same as the theoretical operator induced correlations after applying a threshold of ±0.15, and thus only operator induced correlations are shown in Fig. 4.3. For all considered cases, the center voxel has been picked as the seed voxel to present the theoretical operator induced spatial and temporal correlations although a similar correlation structure can be observed around any voxel.

The first three vertical panels of Fig. 4.3 denote the operator induced real/real, imaginary/imaginary, and real/imaginary spatial correlations for the various cases. Figs. 4.3a and 4.3c show the correlation results for the smoothed SENSE reconstructed data with and without band pass filtering under the assumption of an identity inherent spatial correlation, respectively. It is apparent in Figs. 4.3a and 4.3c that the induced spatial correlations appear as a cluster of voxels instead of individual voxels, as a result of the smoothing operation. It is of note that the center voxel shows negative real/real and imaginary/imaginary correlations with a cluster of voxels in the center of the upper and lower folds due to the choice of *a*=3. The increased spatial correlation between the center voxel with its neighbors can also be observed in real/real and imaginary/imaginary correlations. It can be seen in Figs. 4.3a$_3$ and 4.3c$_3$ that there is no correlation induced between the center voxel's real and imaginary measurements. As expected, temporal

filtering does not alter the spatial correlation structure since Figs. $4.3a_1$-$4.3a_3$ are identical to Figs. $4.3c_1$-$4.3c_3$.

Figs. 4.3b and 4.3d show the correlation results for the smoothed SENSE reconstructed data with and without band pass filtering under the assumption of a non-identity inherent spatial correlation, respectively. As in Figs. $4.3a_3$ and $4.3c_3$, there is no correlation induced between the center voxel's real and imaginary measurements either with or without band pass filtering. One can see in Figs. $4.3b_1$, $4.3b_2$, $4.3d_1$ and $4.3d_2$ that the real/real and imaginary/imaginary spatial correlations between the voxels that are in the originally correlated ROIs are spread to the adjacent voxels by the smoothing operator. Additionally, there is a negative real/real and a negative imaginary/imaginary correlation between the three clusters of correlated voxels and the respective regions from the top and bottom folds. This structure underlines that the inherent true correlation can be observed both in its original location and in the regions that were previously aliased with this original region. This artificially amplified and induced correlation structure could be misinterpreted as a network of functional connectivity in the brain if no steps are taken to identify processing induced correlations.

The fourth panel of Fig. 4.3 denotes the operator induced temporal correlations for the various cases. Figs. $4.3a_4$ and $4.3b_4$ show the temporal correlation matrix of the center voxel when only SENSE reconstruction and smoothing are considered under the assumption of identity and nonidentity initial spatial correlation, respectively. As expected, the temporal correlation structure is not altered by SENSE reconstruction or smoothing as it is shown to be identity for the center voxel. It can be observed in Figs. $4.3c_4$ and $4.3d_4$ that the temporal correlation structure within the real and imaginary

components of the data is altered by temporal filtering with and without presence of initial spatial correlation. Such altered correlations arise from the convolution of the temporal filtering kernel with the voxel time series.
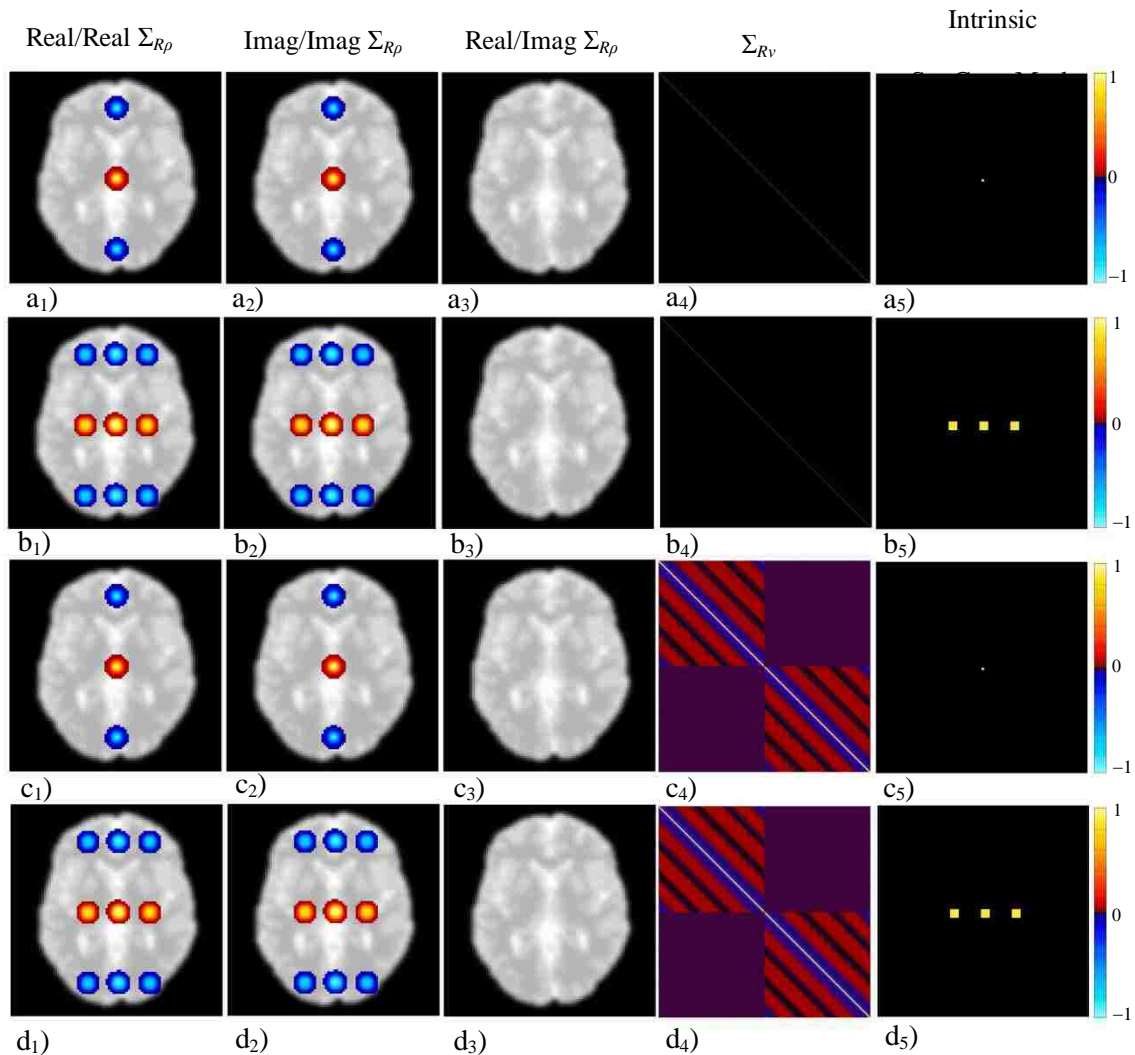
Figure 4.3: Presented on a magnitude brain phantom underlay are theoretical operator induced real/real, imaginary/imaginary, real/imaginary spatial correlations, and temporal correlations of the center voxel under the assumption of SENSE reconstruction and smoothing with a_1)-a_4) identity intrinsic k-space covariance, b_1)-b_4) non-identity intrinsic k-space covariance, c_1)-c_4) band pass filtering and identity intrinsic k-space covariance, d_1)- d_4) band pass filtering and non-identity intrinsic k-space covariance. The intrinsic spatial correlation masks for the considered cases are illustrated in a_5)-d_5).

4.5   Experimental Illustration

In order to analyze the statistical implications of time series processing, two sets of data were acquired for a series of 510 TRs from an array of eight receiver coils in a 3 T General Electric Signa LX MR imager. The first set of data imaged a spherical agar phantom, while the second set was of a non-task human subject. Both data sets were comprised of seven 2.5 mm thick axial slices that are 96×96 in dimension for a 24.0 cm FOV, with the phase encoding direction oriented as posterior to anterior (bottom to top in images). The data set had a TR of 1 s, an echo time of 45.4 ms, an effective echo spacing of 0.816 ms, a flip angle of 45°, and an acquisition bandwidth of 125 kHz. The data was acquired with a time varying TE in the first 20 time points, the remaining 490 images from N_C=4 equally spaced coils were used in the SENSE reconstruction. Data was acquired with an EPI pulse sequence and reconstructed using locally developed software. Subsampling was simulated for a=3 by deleting lines of k-space in each of the acquired data sets. In order to estimate the error in the center frequency and group delay offsets between odd and even k-space lines, three navigator echoes of the center line of k-space were acquired (Nencka et al., 2008).

We present the experimentally computed spatial and temporal correlations about the seed voxel for three different cases. The correlation maps that are presented in Figs. 4.4a and 4.5a are computed from SENSE reconstructed images without spatial smoothing or temporal filtering. The SENSE reconstructed images that were used to compute the correlations presented in Figs. 4.4b and 4.5b have been spatially filtered by a Gaussian smoothing kernel operator whereas the ones that were used to compute the correlations given in Figs. 4.4c and 4.5c have been both spatially filtered and band pass filtered with

cut-off frequencies at 0.009 Hz and 0.08 Hz (Biswal et al., 1995). Presented spatial correlations between the real/real, imaginary/imaginary and real/imaginary as well as the spatial correlations for magnitude-squared data were estimated over the time series. The magnitude-squared correlation structure is observed here because it is asymptotically equivalent to the correlations of magnitude data and linear in nature when magnitude correlations are not. To estimate the temporal correlation maps, both the spherical agar phantom and non-task human subject time series data were divided into 10 sequential 49 time point experiments after removing the first 20 time points. The resulting data was then used to calculate the sample temporal correlation matrix of the center voxel for the various cases.

4.5.1 Phantom Data

The spherical phantom data was considered for an experimental analysis in order to bridge the gap between the theoretical illustration and the application to human subject data, as the phantom is not prone to physiological effects and subject movement. The center voxel was selected as the seed voxel to experimentally analyze the induced correlation structure by spatiotemporal processing in order to be consistent with the presented theoretical induced correlation analysis.

Presented in Figs. $4.4a_1$-$4.4a_4$, $4.4b_1$-$4.4b_4$ and Figs. $4.4c_1$-$4.4c_4$ are the real/real, imaginary/imaginary, real/imaginary, and magnitude-squared spatial correlations between the center voxel and all the other voxels that were computed from SENSE reconstructed data with and without the application of spatial smoothing and low-pass temporal filtering. The correlations presented in Fig. 4.4 were thresholded at ±0.35 (p-value~0.05) (Greicius et al., 2003). As the center voxel was selected as the seed voxel, two fold

regions are expected to exhibit correlations with the center voxel due to the choice of $a=3$. Two pink circles are placed around the corresponding previously aliased voxels, upper and lower folds, in Fig. 4.4 where the seed voxel is indicated by a small green circle. It can be observed in Figs. $4.4a_1$, $4.4a_2$ and $4.4a_4$ that there is a negative real/real, a negative imaginary/imaginary, and a positive magnitude-squared correlation between the voxels in the lower and upper folds and the seed voxel. The correlations in the circles appear to be at individual voxels although additional imaginary and magnitude-squared spatial correlations can be observed around the center voxel as well. This may be due to B-field inhomogeneities that have not been completely corrected.

The correlations between the previously aliased voxels and the seed voxel are spread to clusters of voxels with the application of smoothing, as presented in Figs. $4.4b_1$, $4.4b_2$, $4.4b_4$, $4.4c_1$, $4.4c_2$, and $4.4c_4$. While the correlation structure in the folds and in the center exhibits an oval shape due to the overlap in the reduced FOV image and Nyquist ghosting that has not been completely removed, it can be seen that the neighborhoods of the seed voxel and the upper and lower folds still exhibit the strongest correlation. It is important to note that while there is no real/imaginary correlation between the center voxel and the other voxels as seen in Fig. $4.4a_3$, real/imaginary correlations can be observed in the center, upper and lower folds with the application of smoothing. By comparing Figs. $4.4b_1$-$4.4b_4$ with Figs. $4.4c_1$-$4.4c_4$, it can be seen that temporal filtering slightly alters the spatial correlation structure.

The temporal correlation matrix of the center voxel after SENSE reconstruction without smoothing is given in Fig. $4.4a_5$. Presented in $4.4b_5$ and $4.4c_5$ are the temporal correlation matrices for the center voxel computed from SENSE reconstructed and

spatially smoothed time series data with and without band pass filtering. It is apparent when comparing Figs. $4.4b_5$ and $4.4c_5$ that band pass filtering induces local temporal correlations as the main diagonal is widened and the correlations before filtering are smoothed. When comparing Fig. 4.4a5 to 4.4b5, it can be seen that there is no apparent difference between the temporal correlation structures of the smoothed and smoothed data. As expected, spatial smoothing does not alter the temporal correlations. It is of note that, while such a correlation structure in the processed time series data can be expected, a precise theoretical quantification, as proposed in this chapter, can allow one to account for processing induced correlations in the final analysis of their data.
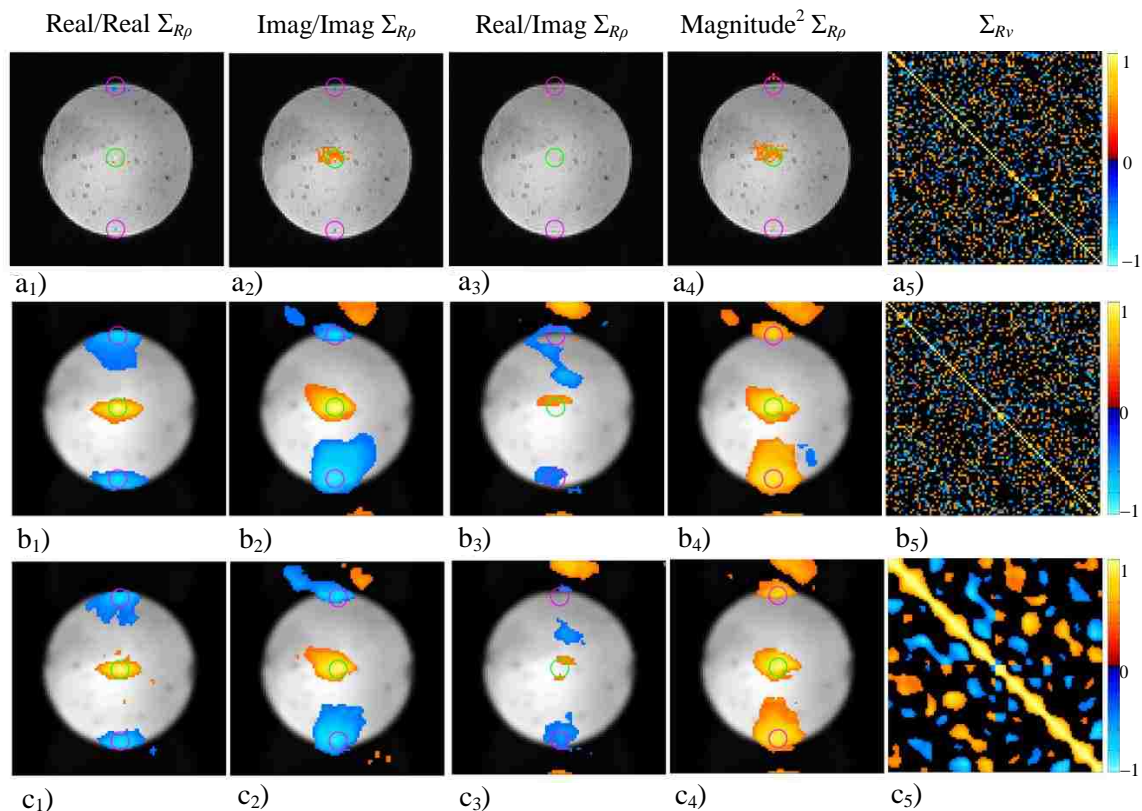
Figure 4.4: Presented on a magnitude spherical agar phantom underlay are estimated real/real, imaginary/imaginary, real/imaginary, magnitude-squared spatial correlations, and temporal correlations of the center voxel throughout the time series of 490 images with a_1)-a_5) SENSE reconstruction; b_1)-b_5) SENSE reconstruction and smoothing; c_1)-c_5) SENSE reconstruction, smoothing, and band pass filtering. Correlations are presented with a threshold of ± 0.35.

4.5.2   Human Subject Data

As with the theoretically generated brain phantom data and experimental spherical phantom data, the center voxel was selected as the seed voxel for the correlation analysis in the human subject data. Figs. $4.5a_1$-$4.5a_4$ show the real/real, imaginary/imaginary, real/imaginary, and magnitude-squared spatial correlations for the seed voxel that were computed from SENSE reconstructed time series. Presented in Figs. $4.5b_1$-$4.5b_4$, and Figs. $4.5c_1$-$4.5c_4$ are the spatial correlations about the seed voxel computed from SENSE reconstructed and spatially smoothed data with and without the application of temporal band pass filtering. Similarly with the spherical phantom data results, two small pink circles are placed around the previously aliased voxels in Fig. 4.5 while the seed voxel is indicated by a small green circle.

The experimental spatial correlations show a negative real/real and imaginary/imaginary correlation and a positive magnitude-squared correlation between the seed voxel and the upper and lower folds, as shown in Figs. $4.5a_1$, $4.5a_2$ and $4.5a_4$. A threshold value of ±0.25 (lower than the threshold value of ±0.35 that is used in theoretical illustration) is applied to the estimated correlations from the human subject data in order to display the general structure of the experimental correlations. While there are no correlated voxels in the real/imaginary theoretical correlation structure in Fig. $4.3a_3$, as well as the experimental spatial correlations computed from spherical phantom in Fig. $4.4a_3$, there appears to be a nonzero real/imaginary correlation structure in Fig. $4.5a_3$. It can be seen in Figs. $4.5b_1$-$4.5b_4$ and $4.5c_1$-$4.5c_4$ that spatial smoothing further spreads the SENSE-induced correlations in the folds and induces positive correlation in the neighborhood of the seed voxel. While it is primarily the amplified SENSE-induced

spatial correlations, real/real spatial correlation maps given in Figs. $4.5b_1$ and $4.5c_1$ exhibit an oval shape of clusters in the fold regions and seed voxel region. This may be due to the noise amplification in the un-aliased images. Similarly with the experimental real/imaginary correlation results of the spherical phantom data, both positive and negative real/imaginary correlations can be observed throughout the images in Figs. $4.5b_3$ and $4.5b_3$. This may be a result of Nyquist ghosting that has not been completely removed and that the brain occupies a small portion of the full FOV which results in aliasing between the center voxel and the voxels in space. By comparing Figs. $4.5b_1$-$4.5b_4$ with Figs. $4.5c_1$-$4.5c_4$, it is interesting to note that the spatial correlation structure is significantly scattered throughout the image after band pass filtering.

Illustrated in Figs. $4.5a_5$, $4.5b_5$ and $4.5c_5$ are the temporal correlation maps about the center voxel computed from the SENSE reconstructed data without spatial smoothing or temporal filtering, with only spatial smoothing, and with both spatial smoothing and temporal filtering, respectively. Similarly with the theoretical induced correlation results and experimental agar phantom results, the temporal filtering process alters the time series correlation structure by widening the main diagonal, which implies local temporal correlations. It is of note here that the theoretical operator induced correlations in Fig. 4.3 were calculated under the assumption of independence between time points. As such, it is evident that the temporal correlation structure in Fig. $4.5c_5$ is the smoothed version of the existing temporal correlations in the data in Fig. $4.5b_5$ rather than exhibiting only a widened main diagonal as in Fig. $4.3d_4$.
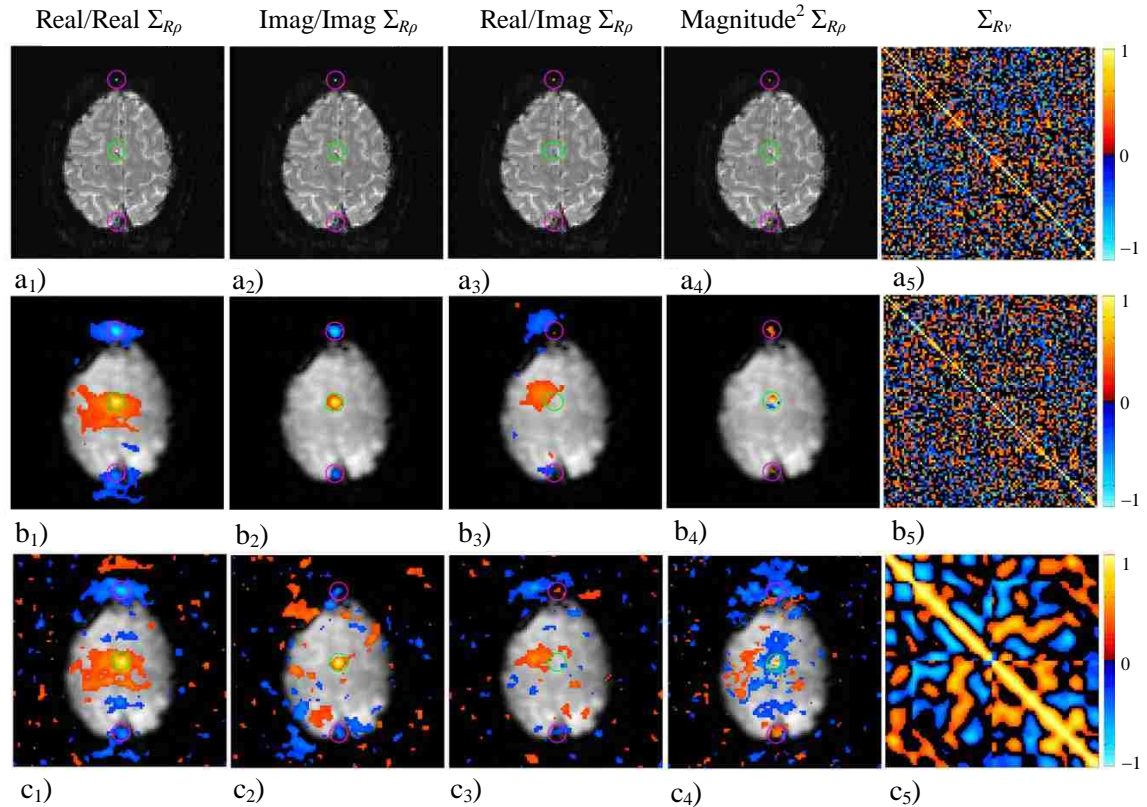
Figure 4.5: Estimated real/real, imaginary/imaginary, real/imaginary, magnitude-squared spatial correlations, and temporal correlations of the center voxel throughout the time series of 490 non-task human subject images with a_1)-a_5) SENSE reconstruction; b_1)-b_5) SENSE reconstruction and smoothing; c_1)-c_5) SENSE reconstruction, smoothing, and band pass filtering. Correlations are presented with a threshold of ± 0.25.

The experimental spatial and temporal correlation results of both the agar phantom and human subject align with the theoretical illustration in Fig. 4.3, and illustrate that SENSE reconstruction and smoothing induce spatial correlations that could result in false positive and negatives in a functional connectivity analysis and misinterpreted if they are not precisely quantified or accounted for. Furthermore, the temporal correlations induced by temporal operators, such as low-pass and high-pass filtering, as well as artificially induced spatial correlations could result in false positive and negatives in fMRI activation statistics as they would make the assumption of independency between voxels invalid. As it becomes increasingly more difficult to derive

the true correlation structure with the use of lengthy Monte Carlo simulations or the parametric covariance functions once the data has been processed, the accuracy of the final analysis of the processed data can be significantly improved with the use of the proposed theoretical linear framework.

4.6   Discussion

In this chapter, we develop a mathematical framework that allows one to analytically observe the effects of commonly used spatial and temporal preprocessing on observed voxel measurements in fcMRI. This framework represents the processing pipeline as a linear isomorphic matrix operator by breaking up each process into a sequence of steps that can be carried out through a collection of matrix operators. With the processes represented in this way, the exact correlation structure induced by each operation both spatially between voxels and temporally within each voxel's time series can be precisely quantified. As the goal of fcMRI studies is to determine, utilize and analyze the true covariance structure of the acquired data, an accurate quantification of the correlation structure is necessary for reliable functional connectivity statistics. This quantification becomes far more challenging once the data has been processed. Even though the spatiotemporal correlation structure of the processed data can be estimated through lengthy Monte Carlo simulations, the proposed AMMUST-t framework provides precise quantification of the implications of such processes and an opportunity to account for them in the final functional connectivity and activation analysis.

We also present the techniques for representing common processing operations such as dynamic B-field correction, image registration, temporal filtering, slice timing correction, and generalizing individual k-space and image space processing as well as

image reconstruction as linear operators. Although the statistical impact of spatial smoothing, SENSE parallel MRI reconstruction, and temporal filtering on the processed data has been presented in detail, additional processing operations can be represented as linear operators and adopted into the AMMUST-*t* framework. While most existing processes are linear in nature, there are select image registration (Poldrack et al., 2011; Klein et al., 2009), spatial normalization (Ashburner and Friston, 1999), spatial smoothing (Smith and Brady, 1997), and high-pass filtering (Marchini and Riley, 2000) operations that can be nonlinear. Although such operations typically use nonlinear calculations to determine various parameters, their application to data is (in most instances) linear. As such, the nonlinear processes that are widely used in biomedical image processing software can also be included into the AMMUST-*t* framework.

The implementation of the AMMUST-*t* framework provides neuroscientists with a means of determining whether or not their selection of reconstruction and processing operations is excessive by observing the artificial correlations that they have induced into their data. With an estimate of the inherent covariance in the acquired data, these changes can be incorporated into an fcMRI model to more accurately analyze processed data. In order to provide a benchmark analysis of the operator induced correlation structure, we use the AMMUST-*t* framework to compute spatial covariance matrix and an individual voxel's temporal covariance matrix, both commonly used fcMRI analysis studies, from an analytically derived spatiotemporal covariance matrix. As the proposed method can easily be applied to data sets in which the implications of processing have been noted, it provides a novel informative tool for preventing possible false positive rates that can result from processing and reconstruction operators. The application of the framework

could enable neuroscientists to reap the benefits of spatial and temporal processing while simultaneously determining the optimal data processing pipeline and identifying the true statistical interpretation of their data.

Chapter 5:   Future Applications

The previous chapter has provided an original approach to quantitatively observe the implications of spatiotemporal processing of fMRI and fcMRI data. As the conventionally used fMRI and fcMRI models compute the brain activity and connectivity of each voxel individually by assuming independence, they do not account for processing induced spatiotemporal covariance structure. In this chapter, we provide ways of accounting for theoretically computed exact noise properties of the fMRI and fcMRI data during the estimation of functional activations and functional correlations. The methods that are proposed in this chapter will incorporate the effects of processing into the analysis, providing a true interpretation of the acquired data and in turn produce more accurate functional activation and connectivity statistics to be used in fMRI and fcMRI application areas such as neurosurgical planning and the diagnosis of degenerative diseases.

5.1   Functional Activity

In fMRI, activations are detected using a hypothesis test in which voxels are assumed inactive under the null hypothesis. As fMRI models make assumptions regarding the statistical properties of noise in the processed data, if the statistical implications of processing are not accounted for, it can result in errors where voxels are either assumed to be active when they are not, or assumed inactive when they actually are. With the linear model presented in section 4.2.1, and the known ideal covariance matrix, Γ_T, the analytically computed entire spatiotemporal covariance matrix, Σ, can be

incorporated into the complex-valued fMRI activation model in order to more accurately calculate the functional activation of all voxels simultaneously.

It has been explained section 2.2.1 that in the CV Model, the observed time series for an individual voxel is represented in a real-valued form by

$$\begin{pmatrix} y_R \\ y_I \end{pmatrix} = \begin{pmatrix} X & 0 \\ 0 & X \end{pmatrix} \begin{pmatrix} \beta\cos\theta \\ \beta\sin\theta \end{pmatrix} + \begin{pmatrix} \eta_R \\ \eta_I \end{pmatrix},$$

$$\eta = \left(\eta_R', \eta_I'\right)' \sim N(0, \Sigma_v), \tag{5.1}$$

with the assumption of a constant phase, θ. Recall that y_R and y_I are real-valued $n\times 1$ vectors, consisting of the real and imaginary components of the processed voxel time series, q is the number of non-baseline regressors, X is an $n\times(q+1)$ design matrix, and β is a $(q+1)\times 1$ vector of magnitude regression coefficients. This model can be extended to a more general case, where the observations contain task related phase changes in addition to task related magnitude changes (Rowe and Logan, 2005b). In this general model, the observed time series vector for an individual voxel is represented by

$$\begin{pmatrix} y_R \\ y_I \end{pmatrix} = \begin{pmatrix} C & 0 \\ 0 & S \end{pmatrix} \begin{pmatrix} X & 0 \\ 0 & X \end{pmatrix} \begin{pmatrix} \beta \\ \beta \end{pmatrix} + \begin{pmatrix} \eta_R \\ \eta_I \end{pmatrix},$$

$$\eta = \left(\eta_R', \eta_I'\right)' \sim N(0, \Sigma_v), \tag{5.2}$$

where, C and S are matrices with the cosine and sine of the voxels modeled phase along the diagonal.

Both the CV Model and the traditional MO Model typically assume independence between voxels and observe brain activity on a voxel-by-voxel basis. As such, the noise

vector in Eq. [5.2] is assumed to be $\eta \sim N(0, \sigma^2 I_2 \otimes I_n)$. However, this assumption does not account for any spatial correlation between voxels, whether inherent of artificially induced. Thus, a generalization of the CV Model that incorporates the analytically derived spatiotemporal covariance matrix is introduced in this section.

The noise vector, η, in Eq. [5.2] assumes a $2n \times 2n$ covariance between the n time points of a single voxel. With temporal processing inducing correlations between time points for each voxel and spatial processing inducing a correlation between the p voxels in each image, the noise of data is better described by the entire $2pn \times 2pn$ reordered spatiotemporal covariance matrix, Σ_T. Each $(j,k)^{\text{th}}$ block of Σ_T is the $2n \times 2n$ temporal covariance matrix between spatial elements j and k. To integrate Σ_T into a CV fMRI model, the linear regression model in Eq. [5.2] can be expanded to derive coefficients for all p voxels at once by

$$
\begin{pmatrix} y_{R1} \\ y_{I1} \\ \vdots \\ y_{Rp} \\ y_{Ip} \end{pmatrix} = \begin{pmatrix} C_1 X_1 \beta_1 \\ S_1 X_1 \beta_1 \\ \vdots \\ C_p X_p \beta_p \\ S_p X_p \beta_p \end{pmatrix} + \begin{pmatrix} \eta_{R1} \\ \eta_{I1} \\ \vdots \\ \eta_{Rp} \\ \eta_{Ip} \end{pmatrix} .
\tag{5.3}
$$

In Eq. [5.3], y_{Rj} and y_{Ij}, and η_{Rj} and η_{Ij} are $n \times 1$ vectors consisting of the real and imaginary components of the image space observations and error measurements of the jth voxel, respectively. The design matrix, X_j, is $n \times (q+1)$, β_j is a $(q+1) \times 1$ vector of magnitude regression coefficients for the jth voxel, and finally C_j and S_j are matrices with the cosine and sine of the jth voxel modeled phase along their diagonals. Eq. [5.3] can alternatively be written by matrix representations as follows

$$
\begin{pmatrix} y_{R1} \\ y_{I1} \\ \vdots \\ y_{Rp} \\ y_{Ip} \end{pmatrix} = \begin{pmatrix} C_1 & 0 & & & \\ 0 & S_1 & & & \\ & & \ddots & & \\ & & & C_p & 0 \\ & & & 0 & S_p \end{pmatrix} \begin{pmatrix} X_1 & 0 & & & \\ 0 & X_1 & & & \\ & & \ddots & & \\ & & & X_p & 0 \\ & & & 0 & X_p \end{pmatrix} \begin{pmatrix} \beta_1 \\ \beta_1 \\ \vdots \\ \beta_p \\ \beta_p \end{pmatrix} + \begin{pmatrix} \eta_{R1} \\ \eta_{I1} \\ \vdots \\ \eta_{Rp} \\ \eta_{Ip} \end{pmatrix}.
\tag{5.4}
$$

As described in Chapter 4, the vector of vectorized images, y_T, is created through

$y_T = O_T s_T$, as a vector of n vectors of p time series observations stacked above themselves.

This vector is in the form of $y_T = (y_{1R}', y_{1I}', \ldots\ldots, y_{nR}', y_{nI}')'$, where y_{tR} and y_{tI} are $p{\times}1$ real

and imaginary column vectors of p voxels at image time point t, respectively. As such,

the reconstructed image space vector y_T should be permuted by $y_P = P_T y_T$ before

computing activation statistics. The equation given in Eq. [5.4] can then be represented in

matrix form,

$$
y_P = JX\beta + \eta,
\tag{5.5}
$$

where y_P and η are $2np{\times}1$ vectors, J is a $2np{\times}2np$ matrix, X is a $2np{\times}2p(q+1)$ matrix, and

β is a $2p(q+1){\times}1$ vector. Note, q is the number of non-baseline regressors. In Eq. [5.5],

the noise vector, η, has a zero mean and a $2np{\times}2np$ spatiotemporal covariance, Σ_T; J is a

diagonal matrix that has the cosine and sine of the jth voxel's temporal phase, C_j and S_j, as

the diagonal elements. The block diagonal design matrix, X, is formed by placing the

design matrix of the jth voxel, X_j, along the diagonal. A simple version of the design

matrix, X_j that corresponds to the jth voxel, has a first column of ones, a second column of

counting numbers from 1 to n, and then a column of zeros and ones representing the task

wave form.

With the assumption of temporarily constant phase for each voxel, the generalized

CV Model parameters, β, θ, and Σ_T can be derived from Eq. [5.5] through a weighted

least squares estimation, and functional activations can be computed by a likelihood ratio test statistic. In the model given by Eq. [5.4], the $(q+1)^{\text{th}}$ element of each β_j denotes the jth voxel's regression coefficient that is related to task activity. Using the contrast vector, V, to observe the $(q+1)^{\text{th}}$ coefficient of each β_j, this statistic considers an estimated variances under the null hypothesis, $H_0: V\beta = \upsilon$, in which no task related to cortical activity is assumed, and under the alternative hypothesis, $H_1: V\beta \neq \upsilon$, that assumes cortical signal that is modeled as task related. In this hypothesis testing setting, the contrast vector, V, can be created as a $p \times 2p(q+1)$ matrix whose j^{th} row is a $1 \times 2p(q+1)$ vector that consists of all zeros with 1's in the $(2j\text{-}1)(q+1)^{\text{th}}$ and $(2j)(q+1)^{\text{th}}$ entries, while υ is a $p \times 1$ column vector consisting of zeros.

5.2   Functional Connectivity

In fcMRI, the null hypothesis assumes no correlation between voxels, and thus any statistically significant correlation observed in the data implies voxels are connected. With the amount of processing performed in fcMRI studies through reconstruction, spatial and temporal filtering, nuisance signal and global signal regression, the statistical properties of processed data are removed from those of the acquired data as presented in Chapter 4. The spatiotemporal covariance matrix, Σ, along with the voxel time series covariance matrix, Σ_ρ, and one voxel's time series covariance matrix, Σ_v, that are commonly utilized in fcMRI studies have been analytically computed in Chapter 4.

In a processing-induced spatiotemporal correlation matrix that is computed with the linear framework presented in Chapter 4, the nonzero off diagonal entries will denote any correlations that are artificially induced by the process. To quantitatively determine

the degree to which voxels in processed images are correlated, a generalized likelihood ratio test statistic for dependence between voxels, that can be derived from the determinant of the correlation matrix, can be used as a metric (Rowe, 2003). Upon converting to a log-likelihood test statistic, any off-diagonal elements in the induced correlation structure are weighted exponentially, which is appropriate given that correlation strength increases quadratically. As the test statistic for dependence between voxels approaches zero when an identity correlation is induced, it can provide a simple means for neuroscientists to characterize their choice of processing as excessive.

While the precise quantification of the correlations induced by spatiotemporal processing provides a useful tool to assess the implications of such processing, the artificially induced correlations can be incorporated into a generalized fcMRI model similarly with the generalized fMRI model given in section 5.1. The regression coefficient β, given in Eq. [5.5], can be utilized with an adjustment to the design matrix, X, in order to detect the functional brain connectivity. In the generalized fcMRI model, the data vector, y_P, represents the vectorized form of the processed resting state time series data. The design matrix, X, therefore can be designed as a block diagonal matrix in which the jth block has a column of ones in the first column and the time series of the jth voxel in the second column. Using a likelihood ratio test, the regression coefficients can be used to determine the correlation between voxels in a hypothesis test in which the null hypothesis assumes no correlation between voxels. The incorporation of the processing induced covariance matrix, Σ_T, into a statistical fcMRI model of this kind provides a novel approach to deduce connectivity in complex-valued data while simultaneously

incorporating the effects of signal processing into the final analysis, thereby improving the accuracy and reliability of fcMRI studies.

Chapter 6:   Conclusion

6.1   Summary of Presented Work

The new statistical fMRI activation model, DeTeCT-ING, that is presented in the second chapter of this dissertation was developed with an aim to utilize the conventionally neglected physical and biological information in brain activation detection. This model provides an original idea to the current state of fMRI activation research by utilizing the first few scans to estimate the relaxation parameters, more appropriately representing the magnetization in each voxel, and incorporating the tissue contrast information into the calculation of brain activation statistics. The statistical analysis of the proposed DeTeCT-ING Model was performed through Monte Carlo simulations that were carried out with the activation data generated under the assumption of various cases as well as experimentally acquired human subject data. With the use of powerful statistical tools such as ROC analysis, comparison of CRLBs and MSEs, it was shown that the DeTeCT-ING Model provides slightly better accuracy in computing brain activation statistics than more conventional fMRI activation models. It was also shown through an experimental analysis that the possible false positives in computed activation statistics can be theoretically eliminated with the use of the DeTeCT-ING Model. The proposed model in Chapter 2 can be applied to improve the sensitivity to detect brain activation in fMRI by theoretically restricting the search volume of the statistical analysis to the gray matter only. This fMRI analysis method can be used to diagnose gray matter diseases, including degenerative diseases, by automatically segmenting gray matter. This application can also be useful in the analysis of the fMRI data prone to producing false

positive rates, as a result of thermal noise, physiological noise, or correlated noise in the data.

In the third chapter, a novel method that incorporates Fourier encoding anomalies, T_1, T_2^*, and ΔB, into the Fourier image reconstruction process is presented. This method was developed through the expansion of the real-valued linear isomorphism of the complex-valued image registration that was also used in the AMMUST-k framework that represents common temporally unvarying image space and k-space processing operations as linear operators. Specifically, we developed a Fourier reconstruction operator that accounts for the physical processes resulting from the MR relaxivities and magnetic field inhomogeneities that occur in the Fourier encoding process. As such, the utilization of the modified Fourier reconstruction operator that accounts for these effects allows one to perform image reconstruction and the correction of such effects in one step via a matrix-vector multiplication. Furthermore, the use of a linear formalization makes it possible to quantify the statistical effects of such correction. The developed modified Fourier reconstruction operator was first illustrated on a theoretical noiseless data set that was generated with the consideration of physical processes resulting from the MR relaxivities, and magnetic field inhomogeneity both separately and simultaneously. The results showed that the developed Fourier reconstruction operator effectively corrects the image blurring, blurring, and loss in image intensity effects of such physical processes. Such correction was also shown to induce negligible correlation in reconstructed images. As the longitudinal relaxation time, T_1, has commonly been neglected with the assumption of a long TR, the focus was placed on an incorporation of T_1 for the experimental illustration of the developed image reconstruction operator. It was shown that such

incorporation provides better image contrast in the reconstructed images by recovering the information of the tissue characteristics that exist prior to T_1 equilibrium. The results also show that such incorporation preserves functional activations and does not induce artificial correlations. The utilization of the developed operator provides better accuracy in reconstructed images and can ultimately lead to more precise image registration with the recovery of the contrast information.

In Chapter 4, the linear AMMUST-k framework is extended to include spatiotemporal processing operations that are commonly applied to fMRI and fcMRI time series data before computing functional activity and connectivity statistics. First, the linear isomorphic representations of time series processing operations, such as slice timing correction, image registration, temporal filtering, and generalization of temporally constant image space and k-space processing operations, as well as parallel SENSE reconstruction operator were presented. In order to theoretically illustrate the developed framework, AMMUST-t, we created cases that consider different combinations of certain operations, parallel SENSE reconstruction, spatial smoothing, and temporal filtering to maintain frequencies between 0.009 and 0.08 Hz. We computed the theoretical induced large spatiotemporal covariance matrix of the processed data by utilizing the AMMUST-t framework with the assumption of both identity and non-identity intrinsic frequency space covariance structure. We then presented the real/real, imaginary/imaginary, and real/imaginary spatial correlations as well as the temporal correlations of the center voxel computed from precisely quantified spatiotemporal covariance matrix. Our theoretical results showed that SENSE reconstruction, spatial smoothing and temporal band pass filtering induce artificial spatial and/or temporal correlations that are of no biological

origin. The theoretical correlation structures induced by the considered operations were validated through experimentally acquired spherical agar phantom and resting state human subject data. In fcMRI, the correlations computed from the processed data through the use of parametric covariance functions are used to create connectivity maps that exhibit true biological correlations. Therefore, the non-biological artificially induced correlation by spatial and temporal processing operations could alter these connectivity maps, resulting in false positives or false negatives in an fcMRI study.

Functional MRI and fcMRI studies employ both spatial and temporal filtering, together with additional signal regression operations. As such, when inferences are drawn from processed data, failure to account for changes in the covariance structure of the data induced by processing can result in Type I or Type II errors. In Chapter 5, we propose to expand models for detecting functional activation and functional connectivity to incorporate an analytically derived spatiotemporal covariance structure of a reconstructed and processed time series. In the fMRI model, the design matrix used in the complex-valued linear regression was designed to detect voxels whose time series correlate with the task performed, while the fcMRI model used a design matrix with blocks down the diagonal that are specific to each voxel in order to determine which voxels correlate with one another. The future application methods proposed in the fifth chapter would incorporate the effects of processing into the analysis, providing a true interpretation of the acquired data and in turn produce more accurate and reliable functional activation and connectivity statistics to be used in fMRI and fcMRI application areas such as neurosurgical planning and the diagnosis of degenerative diseases.

6.2   Future Work

The DeTeCT-ING fMRI activation model, presented in Chapter 2, aims to exploit the structure of the underlying nonlinear dynamic system of the MR magnetization process in modeling fMRI data. In this model, task related neural activity was modeled by means of a differential T_2^* contrast. While the DeTeCT-ING model takes a significant step to provide a more biologically and physically driven model to compute activation statistics, it does not take the hemodynamic response function, which has been used as a measure of response to task based challenge, into account. There are previous models in literature that focus on modeling the BOLD response and the underlying hemodynamic response function, such as the Balloon Model (Buxton et al., 1998; Friston et al., 2000) that describes the dynamics of blood volume and deoxygenation and their effects on the resulting BOLD signal. As such, the DeTeCT-ING Model could be also further expanded to include a more detailed modeling of the physiological processes for the representation of fMRI activation data. In the expanded model, the hemodynamic responses at brain voxels could be re-coded at fMRI image voxels by incorporating the convolution of a stimulus function and the hemodynamic response. Furthermore, as previously stated, the delivery of the blood to the active region is the source of the response to a local increase in metabolic rate. While it is a fact that the oxygenation state of the blood strongly influence the MR signal on T_2 or T_2^* weighted images, change in hemodynamics can produce small alterations in T_1 and effective proton spin density as well. As such, this phenomenon of possible task-related changes in T_1 and spin density could be incorporated into the DeTeCT-ING Model.

The AMMUST-*t* framework developed in Chapter 4 provides a precise quantification of the spatiotemporal correlations induced by processing and parallel reconstruction operations without the need for lengthy simulations. While this framework provides a tool for neuroscientists to visualize the degree to which processing will artificially correlate ones data, it needs an efficient implementation to be integrated into a research study. In order to make this framework more beneficial for the neuroscientists, a software package could be developed to enable them to easily investigate the correlations they have induced in their data through the image reconstruction and spatiotemporal processing operations they have chosen. The program could enable one to enter different scanner and sampling parameters as well as desired processing operations and present the user with an assessment of the configuration specified in terms of the expected correlations induced by the operations to be performed. With the inclusion of a program like this, the current margin of error in the conclusions drawn in functional connectivity studies could be reduced. Furthermore, while a collection of spatial and temporal processing operations have already been represented as linear operations in Chapter 4, several other operations could also be applied to the acquired fMRI and fcMRI data. Additional processing operations, such as respiration and motion correction, global intensity normalization, and global signal regression, can therefore be represented as matrix operators to fit into the AMMUST-*t* framework. The process of incorporation of the relaxation times, T_2^* and T_1, into the image reconstruction process, as explained in Chapter 3, can also be included into the AMMUST-*t* framework by appropriately modifying the reconstruction operators along the diagonal of the time series FR operator.

As mentioned in Chapter 4, it has been noticed in recent studies that changes in the spatiotemporal covariance structure of the fMRI data may result from the acquisition/reconstruction process (Deshpande et al., 2009) and repeated sessions with multiple experimental stimuli (Derado et al., 2010;Bowman, 2005) which need to be compensated for a better analysis of measured brain activity. Recent resting state studies have also raised questions about the effects of preprocessing, specifically global signal correction, on correlation maps including improved specificity of positive correlations and the emergence of negative correlations. As such, a comparative study could be carried out to assess the effect of processing on the final brain activity and connectivity statistics. With the use of open-access data sharing and analysis pipelines, such as the ones that the Human Connectome Project's connectomeDB provides (Marcus et al., 2011), the comparative study could be performed by applying the generalized fcMRI and fMRI models, proposed in Chapter 5, to data sets in which the implications of processing have been noted.

Appendix A: Cramer Rao Lower Bounds of the DeTeCT and DeTeCT-ING Models

With the assumption of a 90° flip angle in the DeTeCT and DeTeCT-ING Models, the temporarily varying magnitude of the magnetization,

$$M_t = \left[M_{t-1}e^{-TR/T_1}\cos(\phi) + M_0\left(1-e^{-TR/T_1}\right)\right]\sin(\phi)e^{-\frac{TE_t}{T_2^*+\delta z_t}} + x_t'\beta_1, \qquad [A.1]$$

becomes

$$M_t = M_0\left(1-e^{-TR/T_1}\right)e^{-\frac{TE_t}{T_2^*+\delta z_t}} + x_t'\beta_1. \qquad [A.2]$$

This assumption reduces the complex valued image, y_t, measured over time t, that is described in Eq. [2.18], to

$$y_t = \left[M_0\left(1-e^{-TR/T_1}\right)e^{-TE_t/(T_2^*+\delta z_t)} + x_t'\beta_1 \right]\left(\cos\theta + i\sin\theta\right) + (\eta_{R_t} + i\eta_{I_t}), \qquad [A.3]$$

which can be written as

$$y_t = M_t\left(\cos\theta + i\sin\theta\right) + \left(\eta_{R_t} + i\eta_{I_t}\right). \qquad [A.4]$$

The complex-valued observation y_t can then be represented at time point t as a 2×1 vector instead of a complex number as

$$\begin{pmatrix} y_{R_t} \\ y_{I_t} \end{pmatrix} = \begin{pmatrix} M_t\cos\theta \\ M_t\sin\theta \end{pmatrix} + \begin{pmatrix} \eta_{R_t} \\ \eta_{I_t} \end{pmatrix}, \qquad [A.5]$$

where $t=1,\ldots,n$. Upon converting from rectangular coordinates $\left(y_{R_t}, y_{I_t}\right)$ in Eq. [A.5] to magnitude and phase polar coordinates (r,φ), the observed data at time t can be

alternatively represented as

$$\begin{pmatrix} r_t\cos\varphi \\ r_t\sin\varphi \end{pmatrix} = \begin{pmatrix} M_t\cos\theta \\ M_t\sin\theta \end{pmatrix} + \begin{pmatrix} \eta_{R_t} \\ \eta_{I_t} \end{pmatrix},$$ [A.6]

where r_t and φ are the observed magnitude and phase at time t. It is of note here that the DeTeCT and DeTeCT-ING Models assume a temporally unvarying constant phase.

The joint distribution of the bivariate observation $\left(y_{R_t}, y_{I_t} \right)$ at time t is

$$p\left(y_{R_t}, y_{I_t} \middle| M_t, \theta, \sigma^2 \right) = \frac{1}{2\pi\sigma^2} \exp\left\{ -\frac{1}{2\sigma^2} \left[\left(y_{R_t} - M_t\cos\theta \right)^2 + \left(y_{I_t} - M_t\sin\theta \right)^2 \right] \right\}.$$ [A.7]

By making the transformation $\left(y_{R_t}, y_{I_t} \right) = \left(r_t\cos\varphi, r_t\sin\varphi \right)$ from rectangular coordinates to polar coordinates with Jacobian of the transformation

$J = \left| (\cos\varphi)(-r_t\cos\varphi) - (-r_t\sin\varphi)(\sin\varphi) \right| = r_t$, and using trigonometric identities, the above equation can be written as

$$p\left(r_t, \varphi \middle| M_t, \theta, \sigma^2 \right) = \frac{r_t}{2\pi\sigma^2} \exp\left\{ -\frac{1}{2\sigma^2} \left[r_t^2 + M_t^2 - 2r_t M_t \cos(\varphi - \theta) \right] \right\}.$$ [A.8]

The CRLB for the variance of an unbiased estimate of a model parameter requires the second derivatives of the logarithm of the likelihood function, LL, with respect to the model parameters. With n temporal observations, the logarithm of the likelihood function of the DeTeCT and DeTeCT-ING Models can be written as

$$LL = -n\log(2\pi) + \sum_{t=1}^{n} \log r_t - n\log\sigma^2 - \frac{1}{2\sigma^2} \sum_{t=1}^{n} \left[r_t^2 + M_t^2 - 2M_t r_t \cos(\varphi - \theta) \right],$$ [A.9]

where the temporarily varying magnitude, M_t, is given in Eq. [A.2] for a 90° flip angle.

By substituting Eq. [A.2] into Eq. [A.9], the logarithm of the likelihood is

$$LL = -n\log(2\pi) + \sum_{t=1}^{n}\log r_t - n\log\sigma^2 - \frac{1}{2\sigma^2} \times$$

$$\sum_{t=1}^{n}\left\{ r_t^2 + (x_t'\beta_1)^2 + \left(M_0\left(1-e^{-TR/T_1}\right)e^{-\frac{TE_t}{T_2^*+\delta z_t}} \right)^2 + 2(x_t'\beta_1)\left(M_0\left(1-e^{-TR/T_1}\right)e^{-\frac{TE_t}{T_2^*+\delta z_t}} \right) \right. \quad \text{[A.10]}$$

$$\left. -2(x_t'\beta_1)r_t\cos(\varphi-\theta) - 2\left(M_0\left(1-e^{-TR/T_1}\right)e^{-\frac{TE_t}{T_2^*+\delta z_t}} \right)r_t\cos(\varphi-\theta) \right\}.$$

Eq. [A.10] can be alternatively represented by the vector multiplications as follows

$$LL = -n\log(2\pi) + \sum_{t=1}^{n}\log r_t - n\log\sigma^2 -$$

$$\frac{1}{2\sigma^2}\left\{ (r-X\beta_1)'(r-X\beta_1) + 2(r-r_*)'X\beta_1 + \right.$$

$$+\left(M_0\left(1-e^{-TR/T_1}\right)s_* \right)'\left(M_0\left(1-e^{-TR/T_1}\right)s_* \right) + \quad \text{[A.11]}$$

$$\left. 2\left(M_0\left(1-e^{-TR/T_1}\right)s_* \right)'(X\beta_1-r_*) \right\},$$

where r_* has the tth element of $r_t\left[\cos(\varphi-\theta)\right]$, and s_* has the tth element of

$\exp\left(\dfrac{TE_t}{T_2^*+\delta z_t}\right)$. It is of note here that the design matrix, X, consists of a single column of

counting numbers in the DeTeCT and DeTeCT-ING Models since β_1 is the coefficient for

a time trend t.

Maximizing the likelihood function in Eq. [A.11] with respect to the parameters is

the same as maximizing the logarithm of the likelihood, LL, with respect to the

parameters and yields

$$\frac{\partial LL}{\partial M_0} = -\frac{1}{2\sigma^2}\left[2M_0\left(1-e^{-TR/T_1}\right)^2 s_*'s_* + 2\left(1-e^{-TR/T_1}\right)s_*'(X\beta_1-r_*) \right], \quad \text{[A.12]}$$

$$\frac{\partial LL}{\partial T_1} = -\frac{1}{2\sigma^2}\left\{2M_0{}^2\left(-TR\frac{e^{-TR/T_1}}{T_1^2}\right)\left(1-e^{-TR/T_1}\right)s_*'s_* + \right.$$

$$\left. 2M_0\left(-TR\frac{e^{-TR/T_1}}{T_1^2}\right)s_*'(X\beta_1 - r_*)\right\},$$

[A.13]

$$\frac{\partial LL}{\partial T_2{}^*} = -\frac{1}{2\sigma^2}\left\{\left(2M_0{}^2\left(1-e^{-TR/T_1}\right)^2\left(\frac{\partial s_*}{\partial T_2{}^*}\right)'s_*\right) + \right.$$

$$\left. \left(2M_0\left(1-e^{-TR/T_1}\right)\left(\frac{\partial s_*}{\partial T_2{}^*}\right)'(X\beta_1 - r_*)\right)\right\},$$

[A.14]

$$\frac{\partial LL}{\partial \delta} = -\frac{1}{2\sigma^2}\left\{\left(2M_0{}^2\left(1-e^{-TR/T_1}\right)^2\left(\frac{\partial s_*}{\partial \delta}\right)'s_*\right) + \right.$$

$$\left. \left(2M_0\left(1-e^{-TR/T_1}\right)\left(\frac{\partial s_*}{\partial \delta}\right)'(X\beta_1 - r_*)\right)\right\},$$

[A.15]

$$\frac{\partial LL}{\partial \beta_1} = -\frac{1}{2\sigma^2}\left[-2X'r + 2X'X\beta_1 + 2X'(r - r_*) + 2M_0\left(1-e^{-TR/T_1}\right)s_*'X\right]$$

[A.16]

$$\frac{\partial LL}{\partial \theta} = -\frac{1}{2\sigma^2}\left\{2\beta_1'X'\left(y_R\sin\theta - y_I\cos\theta\right) + \right.$$

$$\left. 2M_0\left(1-e^{-TR/T_1}\right)s_*'\left(y_R\sin\theta - y_I\cos\theta\right)\right\},$$

[A.17]

since

$$\frac{\partial r_*}{\partial \theta} = y_I\cos\theta - y_R\sin\theta.$$

$$\frac{\partial LL}{\partial \sigma^2} = -\frac{n}{\sigma^2} + \frac{1}{2(\sigma^2)^2}\left\{(r - X\beta_1)'(r - X\beta_1) + 2(r - r_*)' X\beta_1 + \right.$$

$$\left(M_0\left(1 - e^{-TR/T_1}\right)s_*\right)'\left(M_0\left(1 - e^{-TR/T_1}\right)s_*\right) +$$ [A.18]

$$\left. 2\left(M_0\left(1 - e^{-TR/T_1}\right)s_*\right)'\left(X\beta_1 - r_*\right)\right\}.$$

The CRLB for the variance of an unbiased estimate of a model parameter requires the symmetric Hessian matrix, generally denoted by *H* and is formed from the second derivatives of the log likelihoods, *LL*, with respect to the model parameters. The second derivatives of *LL* can be computed from the first derivatives of *LL* given in Eqs. [A.12]-[A.18] as follows:

$$\frac{\partial^2 LL}{\partial M_0^{\,2}} = -\frac{1}{2\sigma^2}\left[2\left(1 - e^{-TR/T_1}\right)^2 s_*' s_*\right],$$

$$\frac{\partial^2 LL}{\partial M_0 \partial T_1} = \frac{\partial^2 LL}{\partial T_1 \partial M_0} = -\frac{1}{2\sigma^2}\left\{\left[2M_0\left(\frac{2TR\left(e^{-TR/T_1} - 1\right)}{T_1^2 e^{-TR/T_1}}\right)s_*' s_*\right] + \right.$$

$$\left.\left[2\left(\frac{-TR e^{-TR/T_1}}{T_1^2}\right)s_*'(X\beta_1 - r_*)\right]\right\},$$

$$\frac{\partial^2 LL}{\partial M_0 \partial T_2^{\,*}} = \frac{\partial^2 LL}{\partial T_2^{\,*} \partial M_0} = -\frac{1}{2\sigma^2}\left\{\left[\left(2M_0\left(1 - e^{-TR/T_1}\right)^2\right)\frac{\partial\left(s_*' s_*\right)}{\partial T_2^{\,*}}\right] + \right.$$

$$\left.\left[2\left(1 - e^{-TR/T_1}\right)\frac{\partial s_*'}{\partial T_2^{\,*}}(X\beta_1 - r_*)\right]\right\},$$

$$\frac{\partial^2 LL}{\partial M_0 \partial \delta} = \frac{\partial^2 LL}{\partial \delta \partial M_0} = -\frac{1}{2\sigma^2} \left\{ \left[\left(2M_0 \left(1 - e^{-TR/T_1} \right)^2 \right) \frac{\partial \left(s_*' s_* \right)}{\partial \delta} \right] + \right.$$

$$\left. \left[2 \left(1 - e^{-TR/T_1} \right) \frac{\partial s_*'}{\partial \delta} \left(X\beta_1 - r_* \right) \right] \right\},$$

$$\frac{\partial^2 LL}{\partial M_0 \partial \beta_1} = \frac{\partial^2 LL}{\partial \beta_1 \partial M_0} = -\frac{1}{2\sigma^2} \left[2 \left(1 - e^{-TR/T_1} \right) s_*' X \right],$$

$$\frac{\partial^2 LL}{\partial M_0 \partial \theta} = \frac{\partial^2 LL}{\partial \theta \partial M_0} = -\frac{1}{2\sigma^2} \left[-2 \left(1 - e^{-TR/T_1} \right) s_*' \left(\frac{\partial r_*}{\partial \theta} \right) \right],$$

$$\frac{\partial^2 LL}{\partial M_0 \partial \sigma^2} = \frac{\partial^2 LL}{\partial \sigma^2 \partial M_0} = \frac{1}{2 \left(\sigma^2 \right)^2} \left\{ 2 \left(1 - e^{-TR/T_1} \right)^2 M_0 s_*' s_* + 2 \left(1 - e^{-TR/T_1} \right) s_*' \left(X\beta_1 - r_* \right) \right\},$$

$$\frac{\partial^2 LL}{\partial T_1^2} = -\frac{1}{\sigma^2} \left\{ \left[M_0^2 \left(-TR^2 \left(\frac{e^{-TR/T_1} - 2e^{-2TR/T_1}}{T_1^4} \right) + 2TR \left(\frac{e^{-TR/T_1} - e^{-2TR/T_1}}{T_1^3} \right) \right) \right] s_*' s_* + \right.$$

$$\left. M_0 \left(\frac{2TRT_1 - TR^2}{T_1^4 e^{TR/T_1}} \right) \right\} s_*' \left(X\beta_1 - r_* \right) \right\},$$

$$\frac{\partial^2 LL}{\partial T_1 \partial T_2^*} = \frac{\partial^2 LL}{\partial T_2^* \partial T_1} = -\frac{1}{\sigma^2} \left\{ -M_0^2 \left(\frac{TR e^{-TR/T_1}}{T_1^2} \right) \left(1 - e^{-TR/T_1} \right) \frac{\partial \left(s_*' s_* \right)}{\partial T_2^*} + \right.$$

$$\left. M_0 \left(\frac{-TR e^{-TR/T_1}}{T_1^2} \right) \frac{\partial s_*'}{\partial T_2^*} \left(X\beta_1 - r_* \right) \right\},$$

$$\frac{\partial^2 LL}{\partial T_1 \partial \delta} = \frac{\partial^2 LL}{\partial \delta \partial T_1} = -\frac{1}{\sigma^2}\left\{ -M_0^2\left(\frac{TRe^{-TR/T_1}}{T_1^2}\right)\left(1 - e^{-TR/T_1}\right)\frac{\partial\left(s_*' s_*\right)}{\partial \delta} + \right.$$

$$\left. M_0\left(\frac{-TRe^{-TR/T_1}}{T_1^2}\right)\frac{\partial s_*'}{\partial \delta}\left(X\beta_1 - r_*\right)\right\},$$

$$\frac{\partial^2 LL}{\partial T_1 \partial \beta_1} = \frac{\partial^2 LL}{\partial \beta_1 \partial T_1} = \frac{1}{\sigma^2}\left[M_0\left(\frac{TRe^{-TR/T_1}}{T_1^2}\right)\right]s_*' X\right\},$$

$$\frac{\partial^2 LL}{\partial T_1 \partial \theta} = \frac{\partial^2 LL}{\partial \theta \partial T_1} = -\frac{1}{\sigma^2}\left[M_0\left(\frac{TRe^{-TR/T_1}}{T_1^2}\right)s_*'\left(\frac{\partial r_*}{\partial \theta}\right)\right]$$

$$= -\frac{1}{\sigma^2}\left[M_0\left(\frac{TRe^{-TR/T_1}}{T_1^2}\right)s_*'\left(y_I \cos\theta - y_R \sin\theta\right)\right],$$

$$\frac{\partial^2 LL}{\partial T_1 \partial \sigma^2} = \frac{\partial^2 LL}{\partial \sigma^2 \partial T_1} = \frac{1}{2\left(\sigma^2\right)^2}\left\{ 2M_0^2\left(\left(-\frac{TRe^{-TR/T_1}}{T_1^2}\right)\right)\left(1 - e^{-TR/T_1}\right)s_*' s_* + \right.$$

$$\left. 2M_0\left(-\frac{TRe^{-TR/T_1}}{T_1^2}\right)s_*'(X\beta_1 - r_*)\right\},$$

$$\frac{\partial^2 LL}{\partial\left(T_2^*\right)^2} = -\frac{1}{\sigma^2}\left\{ M_0^2\left(1 - e^{-TR/T_1}\right)^2\left[\left(\frac{\partial^2 s_*}{\partial\left(T_2^*\right)^2}\right)' s_* + \left(\frac{\partial s_*}{\partial T_2^*}\right)'\left(\frac{\partial s_*}{\partial T_2^*}\right)\right] + \right.$$

$$\left. M_0\left(1 - e^{-TR/T_1}\right)\left[\left(\frac{\partial^2 s_*}{\partial\left(T_2^*\right)^2}\right)'(X\beta_1 - r_*)\right]\right\},$$

$$\frac{\partial^2 LL}{\partial T_2^* \partial \delta} = \frac{\partial^2 LL}{\partial \delta \partial T_2^*} = -\frac{1}{\sigma^2}\left\{ M_0^2\left(1 - e^{-TR/T_1}\right)^2\left[\left(\frac{\partial^2 s_*}{\partial T_2^* \partial \delta}\right)' s_* + \left(\frac{\partial s_*}{\partial T_2^*}\right)'\left(\frac{\partial s_*}{\partial \delta}\right)\right] + \right.$$

$$\left. M_0\left(1 - e^{-TR/T_1}\right)\left[\left(\frac{\partial^2 s_*}{\partial T_2^* \partial \delta}\right)'(X\beta_1 - r_*)\right]\right\},$$

$$\frac{\partial^2 LL}{\partial T_2^* \partial \beta_1} = \frac{\partial^2 LL}{\partial \beta_1 \partial T_2^*} = -\frac{1}{\sigma^2}\left[M_0\left(1-e^{-TR/T_1}\right)\left(\frac{\partial s_*}{\partial T_2^*}\right)' X \right],$$

$$\frac{\partial LL}{\partial T_2^* \partial \theta} = \frac{\partial LL}{\partial \theta \partial T_2^*} = \frac{1}{\sigma^2}\left[M_0\left(1-e^{-TR/T_1}\right)\left(\frac{\partial s_*}{\partial T_2^*}\right)'\left(\frac{\partial r_*}{\partial \theta}\right) \right]$$

$$= \frac{1}{\sigma^2}\left[M_0\left(1-e^{-TR/T_1}\right)\left(\frac{\partial s_*}{\partial T_2^*}\right)' \left(y_I \cos\theta - y_R \sin\theta\right) \right],$$

$$\frac{\partial LL}{\partial T_2^* \partial \sigma^2} = \frac{\partial LL}{\partial \sigma^2 \partial T_2^*} = \frac{1}{\left(\sigma^2\right)^2}\left\{ \left(M_0^{\,2}\left(1-e^{-TR/T_1}\right)^2\left(\frac{\partial s_*}{\partial T_2^*}\right)' s_* \right) + \right.$$

$$\left. \left(M_0\left(1-e^{-TR/T_1}\right)\left(\frac{\partial s_*}{\partial T_2^*}\right)'\left(X\beta_1 - r_*\right) \right) \right\},$$

$$\frac{\partial^2 LL}{\partial \delta^2} = -\frac{1}{\sigma^2}\left\{ M_0^{\,2}\left(1-e^{-TR/T_1}\right)^2\left[\left(\frac{\partial^2 s_*}{\partial \delta^2}\right)' s_* + \left(\frac{\partial s_*}{\partial \delta}\right)'\left(\frac{\partial s_*}{\partial \delta}\right) \right] + \right.$$

$$\left. M_0\left(1-e^{-TR/T_1}\right)\left[\left(\frac{\partial^2 s_*}{\partial \delta^2}\right)'\left(X\beta_1 - r_*\right) \right] \right\},$$

$$\frac{\partial^2 LL}{\partial \delta \partial \beta_1} = \frac{\partial^2 LL}{\partial \beta_1 \partial \delta} = -\frac{1}{\sigma^2}\left[M_0\left(1-e^{-TR/T_1}\right)\left(\frac{\partial s_*}{\partial \delta}\right)' X \right],$$

$$\frac{\partial LL}{\partial \delta \partial \theta} = \frac{\partial LL}{\partial \theta \partial \delta} = \frac{1}{\sigma^2}\left[M_0\left(1-e^{-TR/T_1}\right)\left(\frac{\partial s_*}{\partial \delta}\right)'\left(\frac{\partial r_*}{\partial \theta}\right) \right]$$

$$= \frac{1}{\sigma^2}\left[M_0\left(1-e^{-TR/T_1}\right)\left(\frac{\partial s_*}{\partial \delta}\right)' \left(y_I \cos\theta - y_R \sin\theta\right) \right],$$

$$\frac{\partial LL}{\partial \delta \partial \sigma^2} = \frac{\partial LL}{\partial \sigma^2 \partial \delta} = \frac{1}{\left(\sigma^2\right)^2} \left\{ \left(M_0^2 \left(1 - e^{-TR/T_1}\right)^2 \left(\frac{\partial s_*}{\partial \delta}\right)' s_* \right) + \right.$$

$$\left. \left(M_0 \left(1 - e^{-TR/T_1}\right) \left(\frac{\partial s_*}{\partial \delta}\right)' \left(X\beta_1 - r_*\right) \right) \right\},$$

$$\frac{\partial^2 LL}{\partial \beta_1^2} = -\frac{1}{2\sigma^2}\left(2X'X\right),$$

$$\frac{\partial^2 LL}{\partial \beta_1 \partial \theta} = \frac{\partial^2 LL}{\partial \theta \partial \beta_1} = -\frac{1}{\sigma^2}\left(X' y_R \sin\theta - X' y_I \cos\theta\right),$$

$$\frac{\partial^2 LL}{\partial \beta_1 \partial \sigma^2} = \frac{\partial^2 LL}{\partial \sigma^2 \partial \beta_1} = -\frac{1}{\left(\sigma^2\right)^2}\left[\left(X'X\right)\beta_1 - X'r_* + M_0\left(1 - e^{-TR/T_1}\right)s_*'X\right]$$

$$= -\frac{1}{\left(\sigma^2\right)^2}\left[\left(X'X\right)\beta_1 - X'y_R \cos\theta + X'y_I \sin\theta + M_0\left(1 - e^{-TR/T_1}\right)s_*'X\right],$$

$$\frac{\partial^2 LL}{\partial \theta^2} = -\frac{1}{\sigma^2}\left[\beta_1'X'\left(y_R\cos\theta + y_I\sin\theta\right) + M_0\left(1 - e^{-TR/T_1}\right)s_*'\left(y_R\cos\theta + y_I\sin\theta\right)\right],$$

$$\frac{\partial^2 LL}{\partial \theta \partial \sigma^2} = \frac{\partial^2 LL}{\partial \sigma^2 \partial \theta} = -\frac{1}{\left(\sigma^2\right)^2}\left\{\beta_1'X'\left(y_R\sin\theta - y_I\cos\theta\right) + \right.$$

$$\left. M_0\left(1 - e^{-TR/T_1}\right)s_*'\left(y_R\sin\theta - y_I\cos\theta\right)\right\}.$$

The negative definite second order partial derivative of the log likelihood function, *LL*, can be used to create the symmetric Hessian matrix, *H*. The matrix of the CRLBs can be found by taking the inverse of the Fisher information matrix

$I_F = -E\left[H \middle| M_0, T_1, T_2^*, \delta, \beta_1, \sigma^2\right]$, which is the expectation of the Hessian matrix, *H,* with

respect to y_R and y_I for the given $M_0, T_1, T_2^*, \delta, \beta_1, \sigma^2$.

Appendix B: Maximum Likelihood Estimations of the DeTeCT-ING Model under Null Hypothesis

As described in Appendix A, with the assumption of a 90° flip angle, the logarithm of the log likelihood function, *LL*, in the DeTeCT-ING Model is

$$LL = -n\log(2\pi) + \sum_{t=1}^{n}\log r_t - n\log\sigma^2 -$$
$$\frac{1}{2\sigma^2}\left\{(r - X\beta_1)'(r - X\beta_1) + 2(r - r_*)'X\beta_1 + \right.$$
$$+ \left(M_0\left(1 - e^{-TR/T_1}\right)s_*\right)'\left(M_0\left(1 - e^{-TR/T_1}\right)s_*\right) +$$
$$\left. 2\left(M_0\left(1 - e^{-TR/T_1}\right)s_*\right)'(X\beta_1 - r_*)\right\},$$

[B.1]

where r_* has the tth element of $r_t\left[\cos(\varphi - \theta)\right]$, and s_* has the tth element of

$$\exp\left(\frac{TE_t}{T_2^* + \delta z_t}\right).$$

The MLEs of the DeTeCT-ING Model under the restricted null hypothesis, $H_0 : T_1 = T_{1_{GM}}, T_2 = T_{2_{GM}}, \delta = 0$, are computed by maximizing the likelihood with respect to parameters, M_0, β_1, θ and σ^2. By setting the first derivatives of the log likelihood function, *LL*, that are given in Eqs. [A.12], [A.16], [A.17] and [A.18], equal to zero and solving, the MLEs under the null hypothesis can be found as follows

$$\hat{M}_0 = -\frac{\left(\hat{s}_*'(X\beta_1 - \hat{r}_*)\right)}{\left(1 - e^{-TR/T_{1_{GM}}}\right)\left(\hat{s}_*'\hat{s}_*\right)}$$

[B.2]

$$\hat{\beta}_1 = \left(X'X\right)^{-1}\left(X'\hat{r}_* - \hat{M}_0\left(1 - e^{-TR/T_{1_{GM}}}\right)X'\hat{s}_*\right)$$

[B.3]

$$\frac{\partial \hat{r}_*'}{\partial \hat{\theta}} \left[X\hat{\beta}_1 + \hat{M}_0 \left(1 - e^{-TR/T_{1_{GM}}} \right) \hat{s}_* \right] = 0 \qquad \text{[B.4]}$$

$$\begin{aligned} \hat{\sigma}^2 = \frac{1}{2n} \Bigg\{ & \left(r - X\hat{\beta}_1 \right)' \left(r - X\hat{\beta}_1 \right) + 2 \left(r - \hat{r}_* \right)' X\hat{\beta}_1 + \\ & \left(\hat{M}_0 \left(1 - e^{-TR/T_{1_{GM}}} \right) \hat{s}_* \right)' \left(\hat{M}_0 \left(1 - e^{-TR/T_{1_{GM}}} \right) \hat{s}_* \right) + \\ & 2 \left(\hat{M}_0 \left(1 - e^{-TR/T_{1_{GM}}} \right) \hat{s}_* \right)' \left(X\hat{\beta}_1 - \hat{r}_* \right) \Bigg\}, \end{aligned} \qquad \text{[B.5]}$$

where $\hat{r}_*$ has the tth element of $r_t \left[\cos\left(\varphi - \hat{\theta} \right) \right]$, and $\hat{s}_*$ has the tth element of $\exp\left(\dfrac{TE_t}{T_2^*{}_{GM}} \right)$

with the consideration of the constraints defined by the null hypothesis, $T_1 = T_{1_{GM}}$,

$T_2 = T_{2_{GM}}$, and $\delta = 0$.

Appendix C: Derivation of the Spatial Covariance Matrix from the Spatiotemporal Covariance Matrix

Consider that the reconstructed and processed image space vector, y, has all real voxel values stacked on top of all imaginary voxel values, as given in Eq. [4.1]. The processed spatiotemporal covariance matrix, Σ, can be calculated as

$$\Sigma_{s_j t_l, s_k t_m} = E((y_{s_j t_l} - \bar{y}_{s_j t_l})(y_{s_k t_m} - \bar{y}_{s_k t_m})), \tag{C.1}$$

where (s_j, t_l) are the spatial and temporal indices for the jth element of y at time point l, (s_k, t_m) are the spatial and temporal indices for the vector's k^{th} element at time point m, and $\bar{y}_{s_j t_l}$ is the mean measurement of the jth voxel at time point l in repeated acquisitions. By expanding the product, Eq. [C.1] can be written as

$$\Sigma_{s_j t_l, s_k t_m} = E(y_{s_j t_l} y_{s_k t_m} - y_{s_j t_l} \bar{y}_{s_k t_m} - y_{s_k t_m} \bar{y}_{s_j t_l} + \bar{y}_{s_j t_l} \bar{y}_{s_k t_m}). \tag{C.2}$$

Similarly, the spatial covariance matrix, Σ_ρ, which is estimated from time series observations, can be considered on an element by element basis

$$\left(\Sigma_\rho\right)_{s_j, s_k} = E((y_{s_j} - \bar{y}_{s_j})(y_{s_k} - \bar{y}_{s_k})), \tag{C.3}$$

where $\bar{y}_{s_j}$ is the temporal mean measurement of the jth voxel over the course of the time series. The spatial covariance matrix, Σ_ρ, can then be calculated as

$$\begin{aligned}\left(\Sigma_\rho\right)_{s_j, s_k} &= \frac{1}{n-1}\sum_{t=1}^{n}((y_{s_j t_t} - \bar{y}_{s_j})(y_{s_k t_t} - \bar{y}_{s_k})) \\ &= \frac{1}{n-1}\sum_{t=1}^{n}(y_{s_j t_t} y_{s_k t_t} - y_{s_j t_t}\bar{y}_{s_k} - y_{s_k t_t}\bar{y}_{s_j} + \bar{y}_{s_j}\bar{y}_{s_k}),\end{aligned} \tag{C.4}$$

in a time series with n points.

The average of the diagonal blocks of the large, processed covariance matrix, Σ, can be written as

$$
\begin{aligned}
\left(\Sigma_A\right)_{s_j, s_k} &= \frac{1}{n-1}\sum_{t=1}^{n} E(y_{s_j t_t} y_{s_k t_t} - y_{s_j t_t}\bar{y}_{s_k t_t} - y_{s_k t_t}\bar{y}_{s_j t_t} + \bar{y}_{s_j t_t}\bar{y}_{s_k t_t}). \\
&= E\left(\frac{1}{n-1}\sum_{t=1}^{n} y_{s_j t_t} y_{s_k t_t} - y_{s_j t_t}\bar{y}_{s_k t_t} - y_{s_k t_t}\bar{y}_{s_j t_t} + \bar{y}_{s_j t_t}\bar{y}_{s_k t_t}\right).
\end{aligned}
$$

[C.5]

Under the assumption that the voxel mean does not change over time in a resting state study, $\bar{y}_{s_j t_t}$ is equal to $\bar{y}_{s_j}$. As such, it can be concluded that the average of the diagonal blocks of the large processed covariance matrix, Σ, is the expected value of the spatial covariance matrix, Σ_ρ

$$
\begin{aligned}
\left(\Sigma_A\right)_{s_j, s_k} &= E\left(\frac{1}{n-1}\sum_{t=1}^{n} y_{s_j t_t} y_{s_k t_t} - y_{s_j t_t}\bar{y}_{s_k t_t} - y_{s_k t_t}\bar{y}_{s_j t_t} + \bar{y}_{s_j t_t}\bar{y}_{s_k t_t}\right) \\
&= E\left(\frac{1}{n-1}\sum_{t=1}^{n} y_{s_j t_t} y_{s_k t_t} - y_{s_j t_t}\bar{y}_{s_k} - y_{s_k t_t}\bar{y}_{s_j} + \bar{y}_{s_j}\bar{y}_{s_k}\right) \\
&= E\left(\left(\Sigma_\rho\right)_{s_i, s_j}\right).
\end{aligned}
$$

[C.6]

Thus, the spatial covariance matrix can be computed as the average of the diagonal blocks of the spatiotemporal covariance matrix, Σ.

BIBLIOGRAPHY

Adrian DW, Maitra R, Rowe DB: Ricean versus Gaussian modelling in magnitude fMRI analysis – Added complexity with few practical benefits. Stat. 2013;2(1):303–316.

Antonini A., Leenders K.L., Meier D., Oertel W.H., Boesiger P., Anliker M. T_2 relaxation time in patients with Parkinson's disease. Neurologyn. 1993;43:697–700.

Ashburner, J., Friston, K.J. Nonlinear spatial normalization using basis functions. Hum. Brain. Mapp. 1999;7(4):254-266.

Atlas, S.W. Magnetic resonance imaging of the brain and spine. Lippincott, PA: Williams & Wilkins, 2008.

Bandettini, P.A., Jesmanowicz, A., Wong, E.C., Hyde, J.S., Processing strategies for time course data sets in functional MRI of the human brain. Magn. Reson. Med. 1993; 30:161–173.

Baselice, F., Ferraioli, G., Pascazio, V. Relaxation time estimation from complex magnetic resonance imaging. Sensors 2012;10(4):3611-3625.

Bernstein, M.A., King, K.F., Zhou, X.J. Handbook of MRI pulse sequences. Amsterdam, Academic Press, 2004.

Biswal, B., Yetkin, F.Z., Haughton, V.M., Hyde, J.S. Functional connectivity in the motor cortex of resting human brain using echo-planar MRI. Magn. Reson. Med. 1995; 34:537-541.

Bodurka, J., Ye, F., Petridou N., Murphy, K., Bandettini P.A. Mapping the MRI voxel volume in which thermal noise matches physiological noise-Implications for fMRI. Neuroimage 2007;34:542-49.

Bonny, J.M., Zanca, M., Boir Haackee, J.Y., Veyre, A. T_2 maximum likelihood estimation from multiple spin-echo magnitude images. Magn. Reson. Imag. 1996;36(2):287-293.

Bowman, F.D. Spatio-temporal modeling of localized brain activity. Biostatistics 2005;6(4): 558-575.

Bruce, I.P., Karaman, M.M., Rowe, D.B. A statistical examination of SENSE image reconstruction via an isomorphism representation. Magn. Reson. Imag. 2011;29:1267-1287.

Bruce, I.P., Karaman, M.M., Rowe, D.B. The SENSE-Isomorphism Theoretical Image Voxel Estimation (SENSE-ITIVE) model for reconstruction and observing statistical properties of reconstruction operators. Magn. Reson. Imag. 2012;30:1143-1166.

Bruce I.P., Rowe, D.B. Artificial correlations induced by SENSE and GRAPPA corrupt fcMRI conclusions. Int. Proc. Magn. Reson. Med., 2013;2229.

Bruce I.P., Rowe, D.B. Quantifying the statistical impact of GRAPPA in fcMRI data with a real-valued isomorphism. IEEE Trans. Med. Imaging 2014;33(2):495-503.

Buxton, R.B., Wong, E.C., Frank, L.R. Dynamics of blood flow and oxygenation changes during brain activation: The balloon model. Magn. Reson. Med. 1998;39:855-864.

Buxton, R.B., Uludag, K., Dubowitz, D.J., Liu, T.T. Modeling the hemodynamic response to brain activation. Neuroimage 2004; 23:220-233.

Chai, X.J., Castanon, A.N., Ongur, D., Whitfield-Gabrieli, S. Anticorrelations in resting state networks without global signal regression. Neuroimage 2012; 16;59(2):1420-1428.

Cox, R.W, Jesmanowicz, A., Hyde, J.S. Real-time functional magnetic resonance imaging. Magn. Reson. Med. 1995;33(2):230-236.

Cox, R.W. AFNI: Software for analysis and visualization of functional magnetic resonance neuroimages. Comput. Biomed. Res. 1996;29:162-173.

Della-Maggiore, V., Chau, W., Peres-Neto, P., McIntosh, A.R. An empirical comparison of SPM preprocessing parameters to the analysis of fMRI data. Neuroimage 2001;17:19-28.

Derado, G., Bowman, F.D., Kilts, C.D. Modeling the spatial and temporal dependence in fMRI data. Biometrics 201;66:949-957.

Deshpande, G., LaConte, S., Peltier, S., Hu, X. Integrated local correlation: a new measure of local coherence in fMRI data. Hum. Brain. Mapp. 2009;30(1):13-23.

Friston, K.J., Josephs, O., Zarahn, E., Holmes,A.P., Rouquette, S., Poline, J.B. To smooth or not to smooth? Neuroimage 2000;12:196-208.

Friston, K.J., Mechelli ,A., Turner, R., Price, C.J. Nonlinear responses in fmri: The balloon model, volterra kernels, and other hemodynamics. Neuroimage 2000;12:466–477.

Gach, H.M., Tanase, C., Boada, F. 2D & 3D Shepp-Logan phantom standards for MRI. ICSENG '08;521-526.

Glover, G.H., Li, T.Q., Ress, D. Image-based method for retrospective correction of physiological motion effects in fMRI: RETROICOR. Magn. Reson. Med. 2000; 44(1): 162-167.

Greicius, M.D., Krasnow, B., Reiss, A.L., Menon, V. Functional connectivity in the resting brain: A network analysis of the Default Mode hypothesis. PNAS, 2003; 100:253-258.

Griswold, M.A., Blaimer, M., Breuer, F., Heidemann, R.M., Mueller, M., Jakob, P.M. Parallel magnetic resonance imaging using the GRAPPA operator formalism. Magn. Reson. Med. 2005;54:1553-1556.

Gudbjartsson, H., Patz, S. The Rician distribution of noisy data. Magn. Reson. Med. 2005;34 (6):910-914.

Haacke, E.M., Brown, R., Thompson, M., Vankatesan, R. Magnetic resonance imaging: physical principles and sequence design. New York, NY, USA: John Wiley and Sons, 1999.

Hahn, A.D., Nencka, A.S., Rowe, D.B. Improving robustness and reliability of phase-sensitive fMRI analysis using temporal off-resonance alignment of single-echo time series (TOAST). Neuroimage 2009; 44:742-52.

Hahn, A.D., Nencka, A.S., Rowe, D.B. Enhancing the utility of complex-valued functional magnetic resonance imaging detection of neurobiological processes through postacquisition estimation and correction of dynamic B0 errors and motion. Hum. Brain Mapp. 2012; 33:288-306.

Hahn, A.D., Rowe, D.B. Physiologic noise regression, motion regression, and TOAST dynamic field correction in complex-valued fMRI time series. Neuroimage 2012; 59:2231-2240.

Haldar, J.P., Anderson, J., Sun, S.W. Maximum likelihood estimation of T_1 relaxation parameters using VARPRO. Int. Proc. Magn. Reson. Med. 2007; 41.

Haley A.P., Knight-Scott J., Fuchs K.L., Simnad V.I., Manning C. Shortening of hippocampal spin-spin relaxation time in probable Alzheimer's disease: A 1H magnetic resonance spectroscopy study. Neurosci. Lett. 2004;362:167–170.

Hall, D.A., Gonçalves, M.S., Smith, S., Jezzard, P., Haggard, M.P., Kornak, J. A method for determining venous contribution to BOLD contrast sensory activation. Magn. Reson. Imaging 2002;20:695-706.

Huettel, S.A., Song, A.W., McCarthy, G. Functional magnetic resonance imaging. Sinauer Associates, Inc., Sunderland, MA, USA, 2004.

Jenkinson, M., Bannister, P.R., Brady, J.M., Smith, S.M. Improved optimization for the robust and accurate linear registration and motion correction of brain images. Neuroimage 2002;17:825-841.

Jezzard, P., Balaban, R.S., 1995. Correction for geometric distortion in echo planar images from B0 field variations. Magn. Reson. Med. 1995; 34, 65–73.

Kannengiesser, S.A., Wang, Y., Haacke, E.M. Geometric distortion correction in gradient-echo imaging by use of dynamic time warping. Magn. Reson. Med. 1999; 42, 585–590.

Karaman, M.M., Bruce, I.P, Rowe, D.B. Incorporating simultaneously estimated T_1 and T_2^* of gray matter improves brain activation statistics in fMRI. Int. Proc. Magn. Reson. Med. 2013a; 2285.

Karaman, M.M., Nencka, A.S., Rowe, D.B. Temporal processing of fMRI data induces functional correlations and potentially alters functional activations. Int. Proc. Magn. Reson. Med. 2013b; 2232.

Karaman, M.M., Bruce I.P., Rowe D.B. A statistical fMRI model for differential T_2^* contrast incorporating T_1 and T_2^* of gray matter. Magn. Reson. Imag. 2014a;32(1):9-27.

Karaman, M.M., Rowe D.B., Nencka A.S. Decreasing false positives and negatives from spatio-temporal processing of fMRI. Int. Proc. Magn. Reson. Med., 2014b; 4144.

Klein, A., Andersson, J., Ardekani, B.A., Ashburner, J., Avants, B., Chiang, M., Christensen, G.E., Collins, D.L., Gee, J., Hellier, P., Song, J.H., Jenkinson, M., Lepage, C., Rueckert, D., Thompson, P., Vercauteren, T., Woods, R.P., Mann, J.J., Parsey, R.V. Evaluation of 14 nonlinear deformation algorithms applied to human brain MRI registration. Neuroimage 2009;46(3):786–802.

LaConte, S., Anderson, J., Muley, S., Ashe, J., Frutiger, S., Rehm, K., Hansen, L.K., Yacoub, E., Hu, X., Rottenberg, D., Strother, S. The evaluation of preprocessing choices in singlesubject BOLD fMRI using NPAIRS performance metrics. Neuroimage 2003;18:10-27.

Lai, S., Glover, G.H. Detection of BOLD fMRI signals using complex data. Int. Proc. Magn. Reson. Med. 1997; 1671.

Liu, J., Nieminen, A., Koenig, J.L. Calculation of T_1, T_2 and proton spin density in nuclear magnetic resonance imaging. J. Magn. Reson. 1989;85(1):95-110.

Logan, B.R., Rowe, D.B. An evaluation of thresholding techniques in fMRI analysis. Neuroimage 2004;22(1):95-108.

Maclaren, J.R., Bones, P.J., Millane, R.P., Watts, R. MRI with TRELLIS: a novel approach to motion correction. Magn. Reson. Imag. 2008; 26:474–483.

Marchini, J., Ripley, B. A new statistical approach to detecting significant activation in functional MRI. Neuroimage 2000;12:366–380.

Marcus, D.S., Harwell, J., Olsen, T., Hodge, M., Glasser, M.F., Prior, F., Jenkinson, M., Laumann, T., Curtiss, S.W., Van Essen, D.C. Informatics and data mining tools and strategies for the human connectome project. Front. Neuroinform. 2011;5:4.

Mariappan S.V.S., Subramanian S., Chandrakumar N., Rajalakshmi K.R., Sukumaran S.S. Proton relaxation times in cancer diagnosis. Magn. Reson. Med. 1988;8:119–128.

Mazaheri, Y., Biswal, B.B., Ward, B.D., Hyde, J. Measurements of tissue T_1 spin-lattice relaxation time and discrimination of large draining veins using transient EPI data sets in BOLD-weighted fMRI acquisitions. Neuroimage 2006;32(2):603-615.

Murphy, K., Birn, R.M., Handwerker, D.A., Jones, T.B., Bandettini, P.A. The impact of global signal regression on resting state correlations: are anti-correlated networks introduced? Neuroimage 2009; 44:893-905.

Nan, F.Y., Nowak, R.D. Generalized likelihood ratio detection for fMRI using complex data. IEEE Trans. Med. Imag. 1999;18(4):320-329.

Nencka, A.S., Rowe, D.B. Reducing the unwanted draining vein BOLD contribution in fMRI with statistical post-processing methods. Neuroimage 2007;37:177-188.

Nencka, A.S., Hahn, A.D., Rowe, D.B. A mathematical model for understanding statistical effects of k-space (AMMUST-k) preprocessing on observed voxel measurements in fcMRI and fMRI. J. Neurosci. Meth. 2009;181:268-282.

Nencka, A.S., Hahn, A.D., Rowe, D.B. The use of three navigator echo in Cartesian EPI reconstruction reduces Nyquist ghosting. Int. Proc. Magn. Reson. Med., 2009; 3032.

Ogawa S., Lee T.M., Kay, A.R., Ellermann, J.M., Kim, S.G., Merkle, H., Ugurbil, K.   Intrinsic signal changes accompanying sensory stimulation: Functional brain mapping with magnetic resonance imaging. Proc. Natl. Acad. Sci. U.S.A. 1992;89,5951-5955.

Ogawa, S., Menon, R.S., Tank, D.W., Kim, S.G., Merkle, H., Ellermann, J.M., Ugurbil, K. Functional brain mapping by blood oxygen level-dependent contrast magnetic resonance imaging. Biophys. J. 1993; 64:803–812.

Patel, R., Van De Ville, V., Bowman, D. Determining significant connectivity by 4D spatiotemporal wavelet packet resampling of functional neuroimaging data. Neuroimage 2006;31:1142-1155.

Pauling, L., Coryell, C.D. The Magnetic Properties and Structure of Hemoglobin, Oxyhemoglobin and Carbonmonoxyhemoglobin. Proc. Natl. Acad. Sci. U.S.A. 1936; 22:210-216.

Poldrack, R.A., Mumford, J.A., Nichols, T.E. Handbook of functional MRI data analysis. New York, NY, U.S.A.: Cambridge University Press, 2011.

Poncelet, B.P., Wedeen, V.J., Weisskoff, R.M., Cohen, M.S. Brain parenchyma motion: measurement with cine echo-planar MR imaging. Radiology 1992;185:645-51.

Pruessmann, K.P., Weiger, M., Scheidegger, M.B., Boesiger, P. SENSE: Sensitivity encoding for fast MRI. Magn. Reson. Med. 1999;42:952-962.

Rauscher, A., Barth, M., Reichenbach, J.R., Stollberger, R., Moser, E. Automated unwrapping of MR phase images applied to BOLD MR-venography at 3 Tesla. J. Magn. Reson. Imaging 2003;18:175-80.

Reber, P.J., Wong, E.C., Buxton, R.B., Frank, L.R. Correction of off resonance-related distortion in echo-planar imaging using EPI-based field maps. Magn. Reson. Med. 1998; 39:328-330.

Reichenbach, J.R. The future of susceptibility contrast for assessment of anatomy and function. Neuroimage 2012;62(2):1311-1315.

Rice, S.O. Mathematical analysis of random noise. Bell System Technical Journal 1944;23:282.

Robitaille, P., Berliner, L. Ultra high field magnetic resonance imaging. Berlin, Springer; 2007.

Roebuck, J.R., Haker, S.J., Mitsouras, D., Rybicki, F.J., Tempany, C.M., Mulkern, R.V. Carr-Purcell-Meiboom-Gill imaging of prostate cancer: quantitative T_2 values for cancer discrimination. Magn. Reson. Imag. 2009;27(4):497-502.

Roopchansingh, V., Cox, R.W., Jesmanowicz, A., Ward, B.D., Hyde, J.S. Single-shot magnetic field mapping embedded in echo planar time-course imaging. Magn. Reson. Med. 2003;50:839–843.

Rowe, D.B. Significant fMRI neurologic synchrony using Monte Carlo Methods. Monte Carlo Methods and Appl. 2003; 9(4): 367-385.

Rowe, D.B. Parameter estimation in the magnitude-only and complex-valued fMRI data models. Neuroimage 2005a;25(4):1124-1132.

Rowe, D.B. Modeling both the magnitude and phase of complex-valued fMRI data. Neuroimage 2005b;25:1310-1324.

Rowe, D.B. Magnitude and phase signal detection in complex-valued fMRI data. Magn. Reson. Med. 2009;62(5):1356-1357.

Rowe, D.B., Logan, B.R. A complex way to compute fMRI. Neuroimage 2004;23(3):1078-1092.

Rowe, D.B., Logan, B.R. Complex fMRI analysis with unrestricted phase is equivalent to a magnitude-only model. Neuroimage 2005;24(2):603-606.

Rowe. D.B., Nencka, A.S., Hoffman, R.G. Signal and noise of Fourier reconstructed fMRI data. J.Neurosci. Meth. 2007;159:361-369.

Rowe, D.B., Nencka, A.S. Induced correlation in fMRI magnitude data from k-space preprocessing. Int. Proc. Magn. Reson. Med., 2009;1721.

Saad, Z., Gotts, S.J., Murphy, K., Chen, G., Jo, H.J., Martin, A., Cox, R.W. Trouble at rest: how correlation patterns and group differences become distorted after global signal regression. Brain. Connect. 2012;2(1):25-32.

Severini, T.A. Likelihood methods in statistics. Oxford: Oxford University Press, 2001.

Shaw, M.E., Strother, S.C., Gavrilescu, M., Podzebenko, K., Waites, A., Watson, J., Anderson, J., Jackson, G., Egan, G. Evaluating subject specific preprocessing choices in multisubject fMRI data sets using data-driven performance metrics. Neuroimage 2003;19:988-1001.

Sijbers, J., den Dekker, A.J., Raman, E,. Van Dyck, D. Optimal estimation of T_2 maps from magnitude MR images. Proc. of SPIE Med. Imag. 1998;3338:384-390.

Sijbers, J., den Dekker. AJ, Raman, E., Van Dyck, D. Parameter estimation from magnitude MR Images. Int. J. Imaging Syst. Technol. 1999;10(2):109-114.

Smith, S.M., Brady, J.M. SUSAN-A New approach to low level image processing. Int. J. Comput. Vision 1997;23(1):45-78.

Stroman, P.W. Essentials of Functional MRI. Boca Raton, FL, USA: CRC Press; 2011.

Thulborn, K.R., Waterton, J.C., Matthews, P.M. and Radda, G.K. Oxygen dependence of the transverse relaxation time of water protons in whole blood at high field. Biochim. Biophys. Acta. 1982;714,:265-270.

Tremblay, M., Tam, F., Graham, S.J. Retrospective coregistration of functional magnetic resonance imaging data using external monitoring. Magn. Reson. Med. 2005;53:141-149.

Wheaton, A.J., Borthakur, A., Reddy, R. Application of the keyhole technique to $T_{1\rho}$ relaxation mapping. J. Magn. Reson. Imag. 2003;18(6):745-749.

Zhou, X.J., Liang, Z., Cofer, G.P., Beaulieu, C.F., Suddarth, S.A., Johnson, G. Reduction of ringing and blurring artifacts in fast spin-echo imaging. J. Magn. Reson. Imag. 1993;3(5):803-807.